The performance of ships in wave and wind has been studied for a long time, and an empirical model is formulated in [15] by various CFD simulations, which are shown as follows.

$$R_t^T = R^C + \Delta R_t^{wave} + \Delta R_t^{wind} \tag{5.1}$$

$$\Delta R_t^{wave} = \frac{1}{\mathcal{L}} \cdot \rho_{water} \cdot g \cdot h_t^2 \cdot B_{int}^2 \cdot C^{D.wat}(\tau_t, \theta_t) \tag{5.2}$$

$$\Delta R_t^{wind} = \frac{1}{2} \cdot \rho_{air} \cdot S_{int} \cdot C^{D.air} \cdot \begin{bmatrix} \left(v_t^c + v_t^{wind} cos\theta_t\right)^2 \\ -\left(v_t^c\right)^2 \end{bmatrix} \tag{5.3}$$

$$v_t = \sqrt[c_2]{\frac{R^C}{R_t^T}} \cdot v_t^c \tag{5.4}$$

where R_t^T is the total resistance; R^C is the resistance of calm water; ΔR_t^{wave}, ΔR_t^{wind} are the added resistances of wave and wind; $\mathcal{L}$ is the ship length; ρ_{water} is the density of water; g is the acceleration of gravity; h_t is the wave height; B_{int} is the breath of ship intersection; $C^{D.wat}(\tau_t, \theta_t)$ is the added resistance coefficient, which is determined by wave-length τ_t and weather direction θ_t; ρ_{air} is the density of air; S_{int} is the area of ship intersection; $C^{D.air}$ is the air drag coefficient; v_t^{wind} is the wind speed; v_t^c and v_t are the cruising speed in calm water and wave/wind, respectively.

From the above Eqs. (5.1)–(5.4), there are four main decision variables to calculate the speed loss, i.e., wave height denoted as h_t, wavelength denoted as τ_t, wind speed v_t^{wind} and the weather direction θ_t. It should be noted that the weather direction is defined as the angle between the wind and the ship sailing direction. Since the wave has a similar direction with the wind, weather direction is used to indicate the influence of wave and wind.

Reference [15] has comprehensively studied the speed performance in wave and wind, and gives some fitting curves to calculate $C^{D.wat}$ under different weather direction (under B.N. 6), shown as Fig. 5.4. We can see this coefficient differs from each other when the weather direction changes.

With the above model, the speed loss under uncertain waves and wind can be predicted. Then in the energy management model, the speed loss can be considered in the voyage scheduling, and the propulsion system can response to the speed loss and ensures the punctuality of the ship's navigation.

5.2.2 Adverse Weather Conditions

Adverse weather conditions are those scenarios or areas which are not suitable for navigation [16, 17], and the ships should avoid this type of area for safety. Adverse

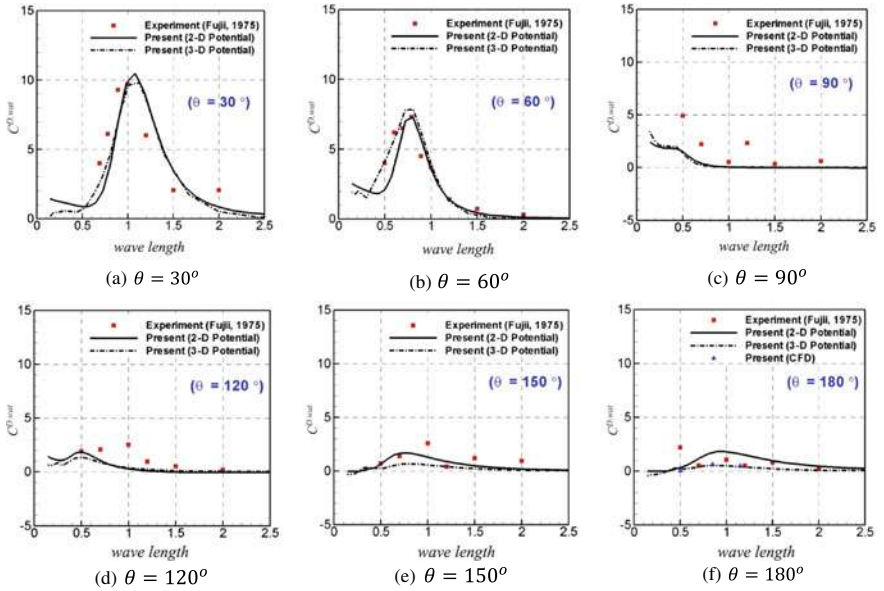

(a) $\theta = 30^o$ (b) $\theta = 60^o$ (c) $\theta = 90^o$

(d) $\theta = 120^o$ (e) $\theta = 150^o$ (f) $\theta = 180^o$

Fig. 5.4 Fitting curves to calculate added resistance of wave. Reprinted from [15], with permission from Elsevier

weather conditions generally include the typhoon or strong ocean current and the following Fig. 5.5 shows the influence of adverse weather conditions on the ship's navigation.

In Fig. 5.5, the primary navigation route is from Singapore to Inchon. The red dash line is the conventional navigation route from Singapore to Inchon due to the shortest distance. However, under pre-voyage weather forecasting, this navigation route is under the influence of a typhoon. Based on this information, the first stage chooses another navigation route (blue dash line) to keep away from the typhoon. In real-time navigation (second stage), the forecasting trajectory of typhoons may change to the black line, and the navigation route obtained in the first stage may still under the influences of typhoons. In this case, the second stage will modify the navigation route and the corresponding cruising speeds as the purple dash line for safe sailing.

From above, the uncertainties of adverse weather conditions come from the weather forecasting error, and the navigation route changes led by the adverse weather conditions will have different energy requirements on the ship power system.

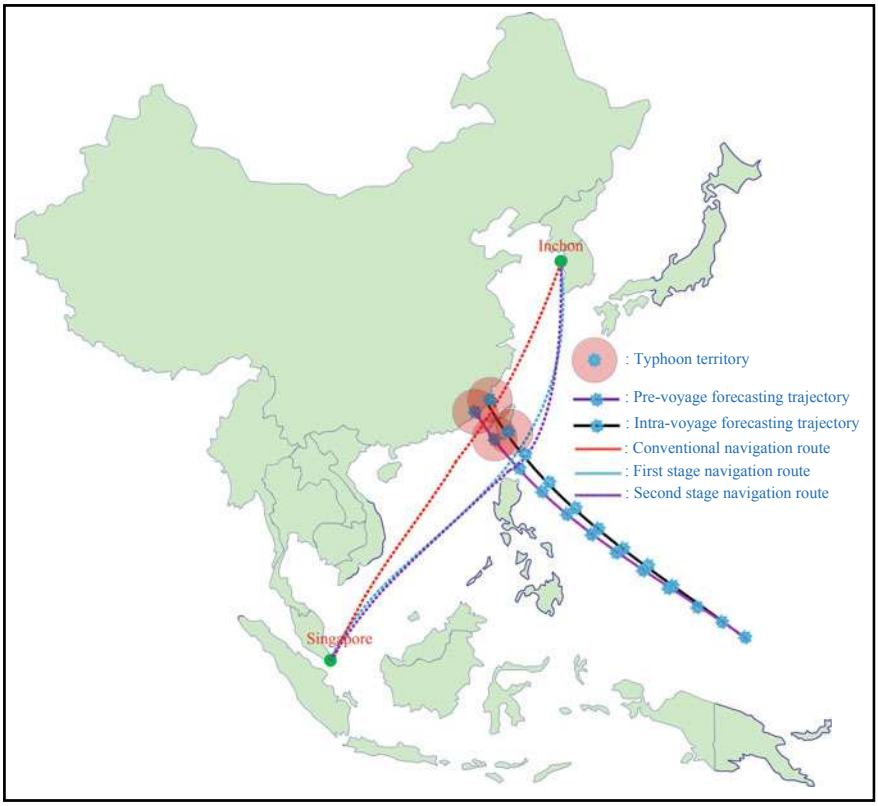

Fig. 5.5 Adverse weather conditions and the two-stage adjustment

5.2.3 Calls-for-Service Uncertainties

The former two types of uncertainties mainly influence the operation of ships and will bring delays to the destination, which brings calls-for service uncertainties to the seaport or other service facilities, such as islands or ocean platforms.

Generally, the services provided to the ships are classified as (1) the logistic services, i.e., cargo handling, and (2) the electric service, i.e., cold-ironing. Since the ships may not arrive on time for different reasons, as stated above, all the services may be delayed. Figure 5.6 shows the influences of calls-for-service uncertainties.

From above, the calls-for-service delays led to different power demand curves, which require different energy schemes. There are two main types of power demand changes, i.e., service delay and service accumulation. The service delay will not change the shape of power demand but only delays them, like the cold ironing power. The other type is the service accumulation, like cargo handling. This type of service has a constant total service workload, and if the service is delayed and the service will accumulate to increase the maximal power demand.

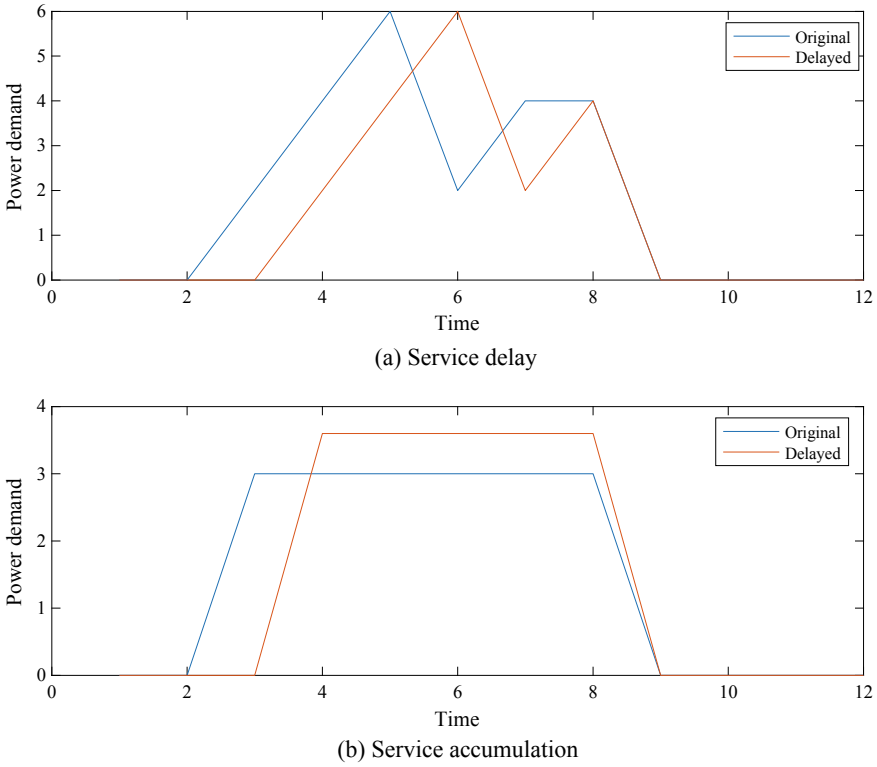

(a) Service delay

(b) Service accumulation

Fig. 5.6 Influences of calls-for-service

5.3 Energy Source Uncertainties

5.3.1 Renewable Energy Uncertainties

Nowadays, environmental issues have been the major concern from the globe, and renewable energy is gradually widely spread in the maritime grids, as we have stated in Chap. 1. However, renewable energy generally has high intermittency and a specified energy management method should accommodate this uncertainty. The following Fig. 5.7 gives a typical wind speed pattern.

The wind speed pattern can be depicted as a spectrum, and a high value indicates a high variation in that timescale [18]. In Fig. 5.7, the first peak is in the timescale of minutes, and the sites with high average wind speed tend to have a lower peak. This variation, referred to as the short-term variation, has been mitigated by many control strategies [19–21]. In the timescale of more than one day (Macro-meteorological range), there are three peaks, (1) Diurnal pattern, or named as the day-night pattern, which is led by the temperature difference between day and night; (2) depressions

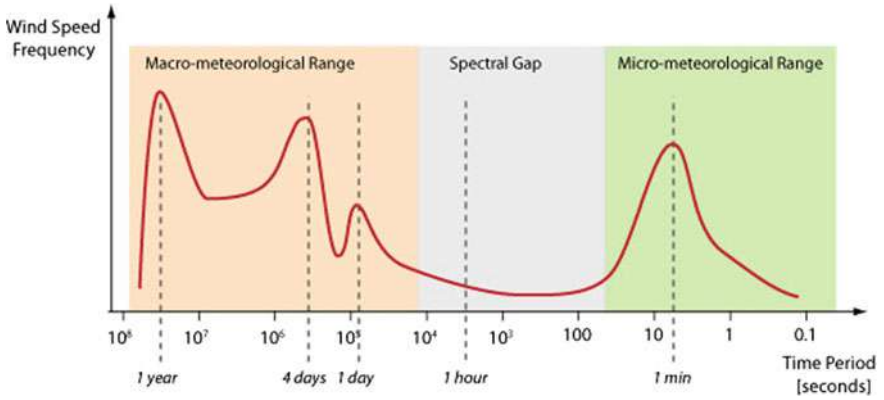

Fig. 5.7 Wind speed patterns. Reprinted from [18], open access

and anti-cyclones, and this phenomenon is more distinct in oceanic than continental regions.; (3) annual pattern, varies with the degree of latitude and vanishes close to the equator. In the following Fig. 5.8a, b, the power outputs of different wind turbines in a day and different seasons are shown.

From the above figure, we can see significant variations by different wind turbines and different seasons. As for the photovoltaic energy, the variations by different modules and different seasons are shown in the following Fig. 5.9a, b.

As above, the power outputs of the wind farm and photovoltaic farm are highly fluctuating, and even after deliberate forecasting, the error is still inevitable. Table 5.2 gives the forecasting error of renewable energy through various methods. The root-mean-square error (RMSE) are around 1–5%, which should be considered in the energy management of maritime grids.

5.3.2 Main Grid Uncertainties

The maritime grids can be mainly operated in (1) grid-connected mode; and (2) isolated mode. Two modes are shiftable for most of the maritime grids. For example, the ships are in isolated mode when sailing, and are in grid-connected mode when receiving the cold-ironing power from the seaport. For a seaport, it can also operate in isolated mode when having enough generators or renewable energy integration.

When in grid-connected mode, the main grid is generally the main energy source of maritime grids. However, there will be many uncertain failures that happened in the main grid and even cause a loss of power. The maritime grids generally don't have a strong network structure, and therefore an energy management method with considering the main grid failure is essential for the safety of maritime grids [26].

Besides, the main grid and the maritime grid maybe not under the same administrator, and the maritime grid should purchase electricity from the main grid, and

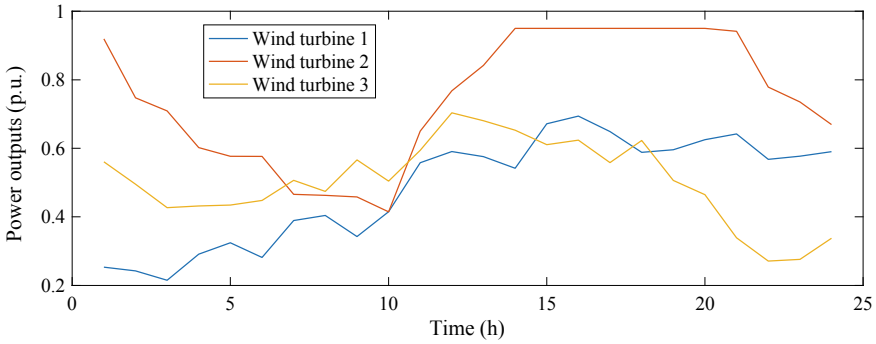

(a) Power outputs by different wind turbines

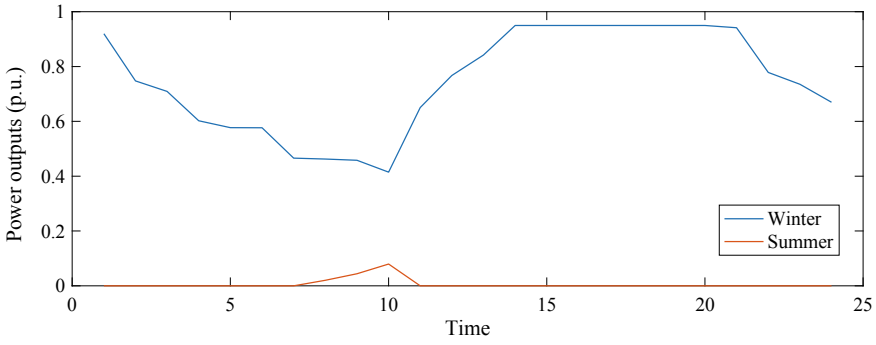

(b) Power outputs in different seasons

Fig. 5.8 Power outputs of different wind turbines and in different seasons

the electricity prices also have uncertainties. The maritime grid should aggregate the total power demand and negotiate the price with the main grid. The price may change in every round of negotiation [27], which also brings the main grid uncertainties.

5.3.3 Equipment Uncertainties

The equipment uncertainties in maritime grids come from two aspects: (1) the equipment failure; and (2) the scheduled maintenance. Their difference is the equipment failure may happen unattended but the latter one is planned.

For the equipment failure, the energy management system of maritime grids has to make enough power reserve for each severe scenario [8]. In [28, 29], to avoid the influence of the onboard generator's failure, the generation system have reserved a certain part of capacity, which are the same in ships and seaports. For a seaport,

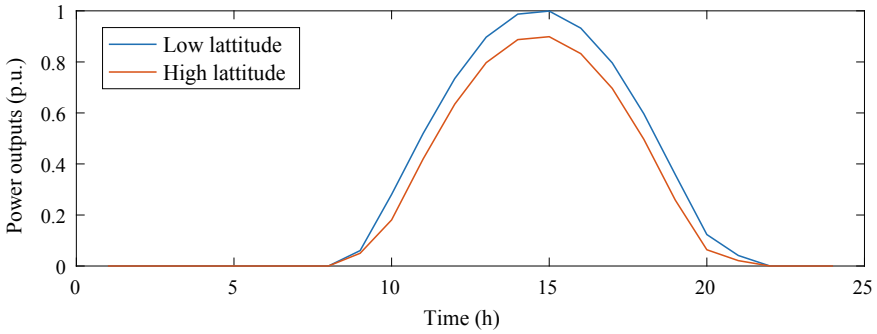

(a) Power outputs in different lattitude

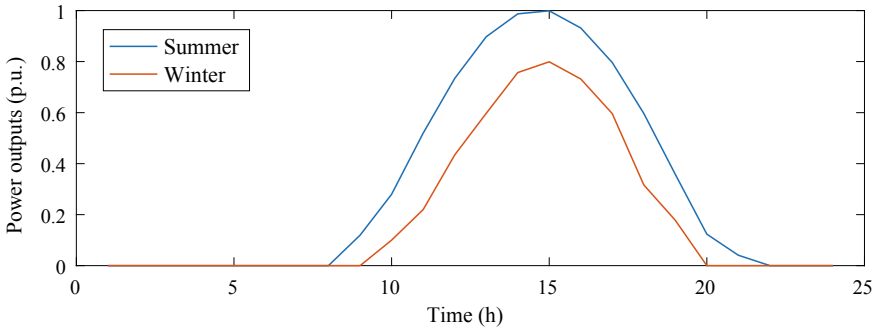

(b) Power outputs in different seasons

Fig. 5.9 Power outputs of different photovoltaic modules and in different seasons

Table 5.2 Forecasting error by different methods

Methods	Renewable energy	Timescale	Error (%)	References
f-ARIMA	Wind	Day-ahead	5.35	[22]
ANN	Wind	Day-ahead	1.32–1.56	[23]
SVM	PV	120 h	1.21	[24]
ARIMA	PV	1~39 h	21	[25]

the power reserve ratio can be lower since the main grid can provide enough power with high reliability, but the within generators still need to be standby for uncertain failure.

For the scheduled maintenance, the equipment out of service is known in advance, and the energy management system can make necessary adjustments. For example, when a generator in a seaport is planned to be in maintenance, the administrator of the seaport will give a new energy plan to the upper main grid to purchase more electricity [27].

5.4 Data-Driven Optimization with Uncertainties

5.4.1 General Model

The main types of uncertainties in the operation of maritime grids are illustrated as above. To ensure the safety and reliability of maritime grids, considering the above uncertainties in energy management is necessary. Nowadays, stochastic optimization [30–32] and robust optimization [32–34] are two main types to address the uncertainties, which are shown as following Eqs. (5.5) and (5.6), respectively.

$$\min_{x \in X} g(x) + E\left(\min_{y \in Y(x,\xi)} f(y)\right) \tag{5.5}$$

$$\min_{x \in X} g(x) + \max_{\xi \in U}\left(\min_{y \in Y(x,\xi)} f(y)\right) \tag{5.6}$$

In stochastic optimization (Eq. (5.5)), x is the first stage decision variables which are not determined by uncertainties; X is the feasible region of x; $g(x)$ is the objective function of the first stage; ξ is the uncertain variables, and $Y(x, \xi)$ is the feasible region of y determined by x and ξ; $f(y)$ is the objective function of the second stage; $E(\cdot)$ is the expectation. In this model, the uncertain variable ξ is depicted by the probability distribution, such as the probability distribution of equipment failure, or the probability distribution of renewable energy output, and so on. Then stochastic optimization seeks the optimal solution within the feasible region defined by the probability distributions.

In robust optimization (Eq. (5.6)), the main difference is the uncertain variable ξ is described by the uncertainty set U, including the upper/lower limits and the uncertainty budget, which mainly has polyhedral models [35] and ellipsoid models [36]. Then robust optimization seeks the optimal solution in the worst case in the defined uncertainty set and brings conservatism. With above, the primary problem of the uncertainty modeling is how to determine the feasible regions, such as the probability distributions in stochastic optimization and the uncertainty set in robust optimization.

As above, how to get the range of uncertain variables, i.e., the probability distribution function or the uncertainty set of ξ, is the basic problem of the optimization model. Nowadays, with the development of measurement and communication technology, more operating data can be transmitted and stored in the control center in real-time. How to use this type of massive data to model the feasible region of uncertainty has become a hot topic, and various methods have been proposed.

5.4.2 Data-Driven Stochastic Modeling

Stochastic modeling is to get the probability distribution functions of uncertain variables, and there are three types in general, (1) the non-parametric probability modeling; and (2) stochastic process modeling and (3) artificial intelligence methods.

The non-parametric probability modeling method directly extracts features from the original dataset and doesn't limit the probabilistic distribution prototype [37], thus may have higher accuracy when having limited knowledge on the dataset characteristics. Based on the diffusion-based density method, [38] proposes a non-parametric probabilistic model for wind speed. Later on, [39] proposes a model for wind speed combined the non-parametric probability modeling and auto-regression modeling. Then based on the non-parametric probability modeling, [40] formulates a probabilistic optimal economy dispatch model for a renewable integrated microgrid, and the case study proves the proposed method can improve the economic behaviors during uncertainties.

The basic idea of stochastic process modeling is to use a series of simple kernel functions to fit the complex function [41]. Based on different basis functions, stochastic process modeling has many representatives. The autoregression and moving average (ARMA) method is one of them and has been utilized in renewable power prediction, and power demand prediction [22, 25]. To reduce the dimension of the dataset, many reduction algorithms are implemented. Based on Karhunen-Loeve expansion, a time-space modeling method for renewable energy is proposed in [42, 43]. Then [44] proposes a solution method for this uncertainty modeling, and shows a lower computational burden with acceptable accuracy.

Compared with the above two types, the methods based on artificial intelligence has stronger data mining ability. The uncertain set can be directly modeled and no necessary to follow the conventional process of "probability distribution formulation-sampling-scenario reduction". Until now, various methods, such as the generative adversarial network (GAN) [45], recurrent neural network (RNN) [46], extreme learning machine (ELM) [47], are implemented to provide uncertain set by massive original dataset.

5.4.3 Data-Driven Robust Modeling

Robust modeling is to get the set of uncertain variables, and there are also three types in general, (1) the polyhedral set; and (2) the ellipsoid set and (3) the uncertain set based on scenarios.

The polyhedral set is the most commonly used uncertainty set for robust modeling, which is based on a series of upper and lower limits, shown as Eq. (5.7).

$$U = \left\{ \xi_t | \underline{\xi} \leq \xi_t \leq \bar{\xi}, \forall t \in T \right\} \tag{5.7}$$

where $\underline{\xi}$ and $\bar{\xi}$ are the lower and upper limits of ξ_t. If the uncertainty series follows the Markov law, the lower and upper limits may become $\underline{\xi} = \underline{\xi}_t(\xi_{t-1})$ and $\bar{\xi} = \bar{\xi}_t(\xi_{t-1})$. To limit the range of uncertain variables, uncertainty budget constraints may be added, shown as Eq. (5.8).

$$\underline{\eta} \leq \sum\nolimits_t \xi_t \Big/ \mu \cdot |T| \leq \bar{\eta} \tag{5.8}$$

where μ is the expectation of ξ; and $\underline{\eta}$, $\bar{\eta}$ are the lower and upper budgets of uncertain variable ξ. The uncertainty budget is used to limit the dramatic changes and reduce the conservatism of the robust model.

The second type is the ellipsoid set, which aims to solve the inconsistent characteristic at the boundary of the uncertain set. A general form is shown in Eqn.

$$U = \left\{ \xi_t \middle| (\xi - \mu)^T \cdot \sum\nolimits^{-1} (\xi - \mu) \leq \Gamma \right\} \tag{5.9}$$

where μ is the expectation of ξ; and $\sum$ is the correlation matrix of ξ. Li et al. [48] use the ellipsoid set to model the uncertainties, and find the ellipsoid set can better represent the uncertainty when approaching the boundary. Kumar and Yildirim [49] proposes the minimum volume enclosing ellipsoid (MVEE) method to limit the uncertainty in the smallest ellipsoid and reduce the conservatism. Based on MVEE, [50] studies the robust optimization based on the ellipsoid set, and proposes an invalid constraint reduction method to simplify the solution method.

Besides the above two modeling methods, there is a modeling method based on extreme conditions. In [51], an ellipsoid set of uncertainty is first formulated and then several extreme points are selected to form a convex set. The formulated robust model is shown as follows.

$$\begin{cases} \max\limits_{\xi_n \in U_n} \left(\min\limits_{x, y_n} f(x, y_n, \xi_n) \right) \\ s.t. A(x, y_n, \xi_n) = 0 n = 1, 2, \ldots, N \\ B(x, y_n, \xi_n) \leq 0 n = 1, 2, \ldots, N \end{cases} \tag{5.10}$$

where ξ_n is the uncertain variable in the n-th extreme scenarios, and y_n is the corresponding second stage decision variables; A and B are the equality and inequality constraints, respectively.

Another robust modeling formulates the uncertain set as a convex envelope to contain all the pre-given extreme points and can be shown as Eq. (5.11). α_n is the ratio for the n-th extreme scenario.

$$U = \left\{ \xi | \xi = \sum_n \alpha_n \cdot \xi_n, \sum_n \alpha_n = 1, \alpha_n \geq 0 \right\} \tag{5.11}$$

5.5 Typical Problems

5.5.1 *Energy Management for Photovoltaic (PV) Uncertainties in AES*

As the main representative of maritime grids, AESs face many uncertainties during navigation. This Chapter focuses on the uncertainties of onboard photovoltaic (PV) integration. This research is illustrated in detail in [52].

(1) Onboard PV power forecasting

In land-based PV power forecasting, the PV power is determined by three factors, i.e., the irradiation density, denoted as I^{Gh}, and the angle between solar rays and the PV modules, denoted as θ, and the generation efficiency, usually determined by the ambient temperature [53], denoted as η^{PV}. However, some differences compared with the load-based applications should be incorporated into the onboard PV forecasting.

The first difference is that the ship will constantly move along the navigation route. As shown in Fig. 5.10, the ship has different locations when t_1 and t_2, meanwhile the direction of solar rays, as well as the ambient temperature along the navigation route, are also changed. Therefore, it is sensible to utilize the measured data along the route, rather than the data in a stationary place to predict the PV generation.

The second difference is that the shipboard deck will constantly swing when cruising and change the angle between solar rays and the PV modules [53], shown in Fig. 5.11. The angles between solar rays and ship decks become $(\theta \pm \phi)$, which further affects the PV generation outputs. In general, the swinging direction of ships

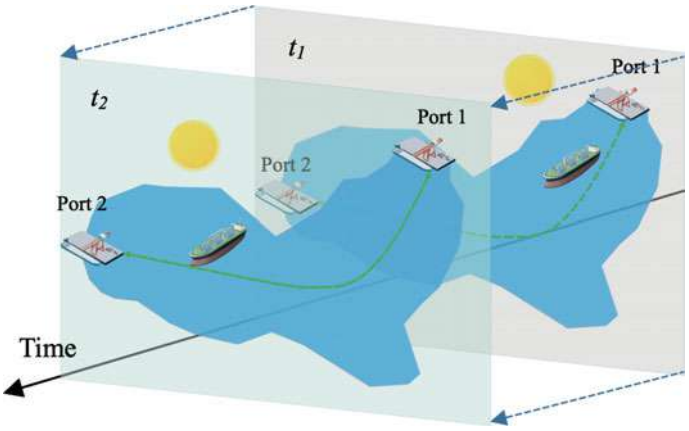

Fig. 5.10 An illustration on the moving of ships

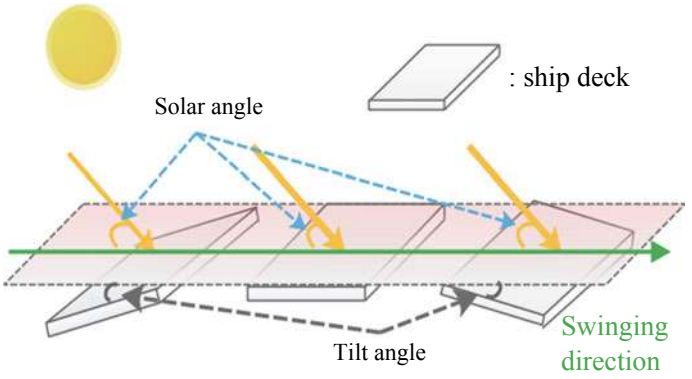

Fig. 5.11 Definition of the angle of solar ray and the tilt angle. Reprinted from [52], with permission from IEEE

is the same with the wind direction and the tilt angle is determined by the wind speed. So, it is necessary to incorporate wind speed along the navigation route to forecast the tilt angle range of ships.

(2) Two-stage robust modeling framework

The above two characteristics are both considered, and this Chapter proposes a data-driven PV generation uncertainty characterization method, shown as the below Fig. 5.12a. The general framework of the two-stage robust modeling is shown as Fig. 5.12b.

In Fig. 5.12a, owing to the high scalability and fast computational speed, the Extreme Learning Machine (ELM) is regarded as a useful learning technique for training a single hidden-stage feed-forward neural network [54]. In Fig. 5.12b, the forecasting values and error of irradiation density, wind speed, and temperature

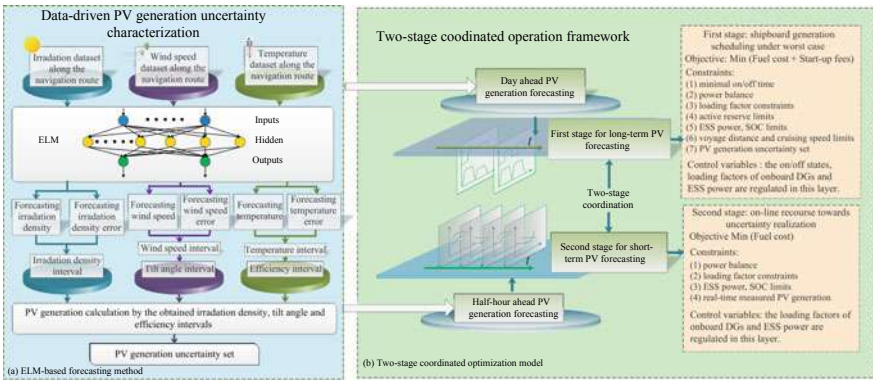

Fig. 5.12 Overall framework of proposed model. Reprinted from [52], with permission from IEEE

are obtained by ELM. Then three intervals, i.e., the irradiation density intervals $\left[I_{min,t}^{Gh}, I_{max,t}^{Gh}\right]$, the tilt angle intervals $\left[\phi_t^{min}, \phi_t^{max}\right]$ and the PV generation efficiency intervals $\left[\eta_{min,t}^{PV}, \eta_{max,t}^{PV}\right]$ are obtained by two different ways, i.e., $\left[I_{min,t}^{Gh}, I_{max,t}^{Gh}\right]$ is calculated by the forecasting values and error, and $\left[\phi_t^{min}, \phi_t^{max}\right]$, $\left[\eta_{min,t}^{PV}, \eta_{max,t}^{PV}\right]$ are calculated by the forecasting wind speed intervals and temperature intervals, since higher wind speed and temperature will lead to larger rolling effect and generation efficiency, respectively.

$$P_t^{PV} = \eta_t^{PV} \cdot A_{PV} \cdot I_t^{Gh} \cdot \begin{bmatrix} \cos\theta_t + C_{\phi_1}\left(\cos\frac{\phi_t}{2}\right)^2 \\ +C_{\phi_2}\left(\sin\frac{\phi_t}{2}\right)^2 \end{bmatrix} \tag{5.12}$$

Based on the obtained uncertain PV generation as (5.12), the proposed two-stage multi-timescale coordinated operation framework aims to coordinate different controllable resources in different timescales according to their different response characteristics considering the uncertain PV outputs, which is shown in Fig. 5.12b. In the day-ahead time-window, i.e., the first stage, the DGs' on/off states and the cruising speed, which cannot instantly respond to the uncertainties, are optimized based on day-ahead interval predictions of the PV generation. This stage aims to dispatch the DGs and ESS on a large time horizon to fulfill propulsion and service loads in the worst case of PV generation.

During the half-hour-ahead online operation time-window, i.e., the second stage, the loading factor of DGs and ESS are re-dispatched based on half-hour-ahead predictions of the PV generation. The half-hour-ahead predictions tend to be more accurate and they can be regarded as the uncertainty realization. Thus, the second-stage operation aims to compensate for the first-stage operation when the uncertainties realize in practice.

(3) Case description

In this study, a typical medium voltage direct current (MVDC) 4-DGs AES case is used to verify the proposed method. The topology and navigation data of this 4-DG AES are shown in Figs. 5.13 and 5.14, respectively. The topology is from [55], which follows the ABS-R2 standard [56]. In Fig. 5.13, 4 DGs are connected in two buses via AC/DC converters, and the circuit breaker is normally open. In general cases, two buses are located in different watertight compartments for avoiding operating risk. As for the PV generation uncertainty set characterization, the training datasets are also applied to [53], which are deduced from real-world navigation from Dalian, China to Aden, Yemen, and 2 MW PV modules are integrated into the AES for future applications. Other detailed parameters can be found in [52].

(4) Case study

To test the validity of the proposed forecasting process, three forecasting methods are compared. The results are shown in Fig. 5.15.

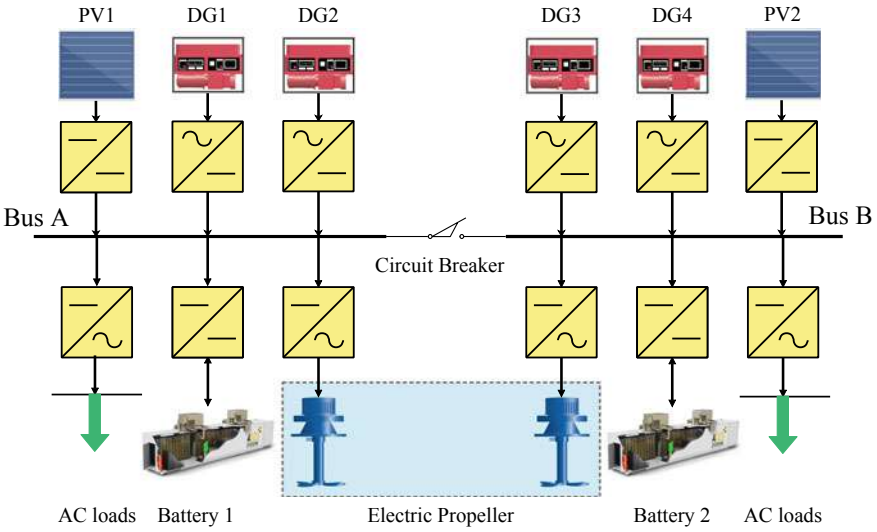

Fig. 5.13 Topology of 4-DG AES. Reprinted from [52], with permission from IEEE

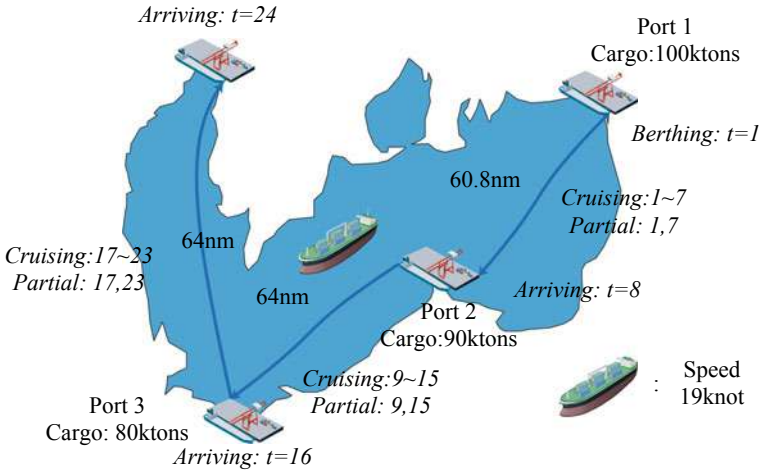

Fig. 5.14 Navigation scheme of AES. Reprinted from [53], with permission from IEEE

Forecasting method A: the proposed method considering both the movement and tilt angle (wind speed);

Forecasting method B: the proposed method without considering the tilt angle (wind speed);

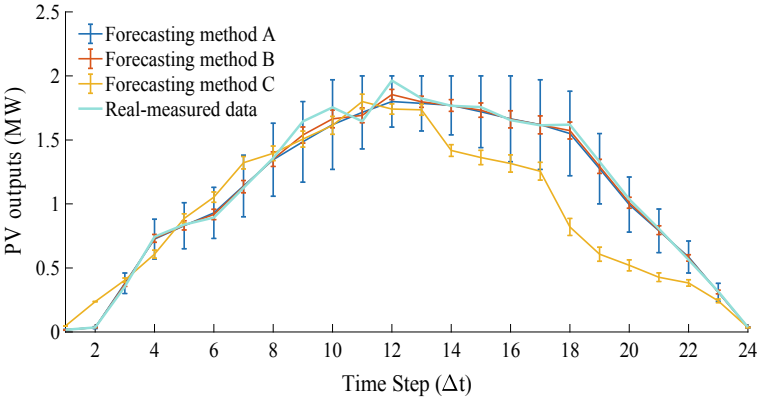

Fig. 5.15 Forecasting results under different methods. Reprinted from [53], with permission from IEEE

Forecasting method C: forecasting method only using the dataset in a stationary place (irradiation density, temperature) without considering the tilt angle.

From Fig. 5.15, the following conclusions can be found, (1) from the comparison between methods A and B, the forecasting intervals become much wider when considering tilt angle. This phenomenon suggests the rolling of the shipboard deck will bring more uncertainties to the PV generation, and if it is ignored, an optimistic scheme may be obtained; (2) from the comparison between method B and C, the forecast error of method C becomes rather large when the ship is away from the initial port ($t = 14 \sim 24$), which suggests the necessity to use the dataset along the navigation route to predict the PV generation.

The energy scheduling schemes in two stages are shown in Figs. 5.16 and 5.17, respectively. From Fig. 5.16, since the PV generations in the second stage are all larger than the worst case, the DGs' outputs are further replaced by the PV integration, which introduces further FC reductions. From Fig. 5.17, the ESS power in most of the partial intervals is increased, which means the PV generation increments are directly charged to the ESS in the partial intervals, therefore in the cruising intervals the ESS has more energy to shed the power demands of DGs than the first stage.

The above results manifest that, since the worst case of PV generation only happens in a small probability, therefore the single-stage robust method will introduce plenty of conservatism to the operating scheme, which leads to wastes on the PV generation. In this section, the online half-hour-ahead operation can effectively go against the uncertainty realization to improve the overall energy utilization efficiency while satisfying the constraints.

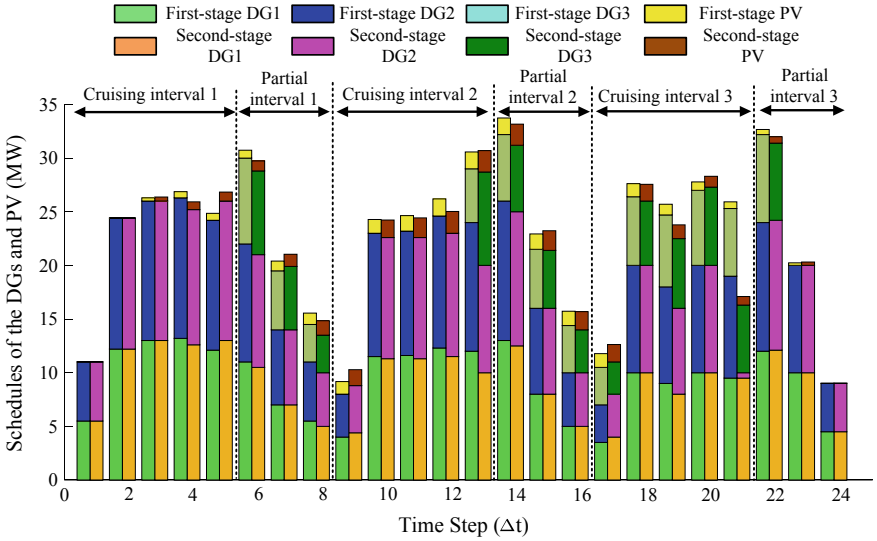

Fig. 5.16 Scheduling schemes of DGs in the first and second stages. Reprinted from [53], with permission from IEEE

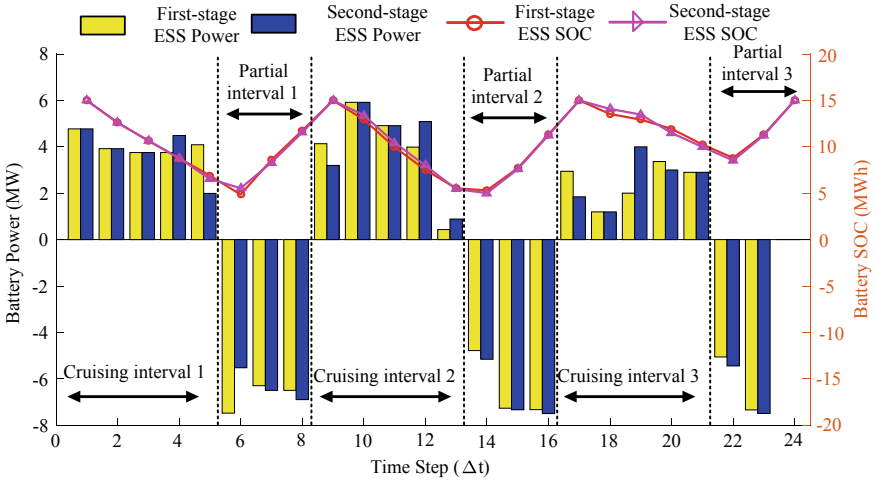

Fig. 5.17 ESS outputs and SOC in the first and second stages. Reprinted from [52], with permission from IEEE

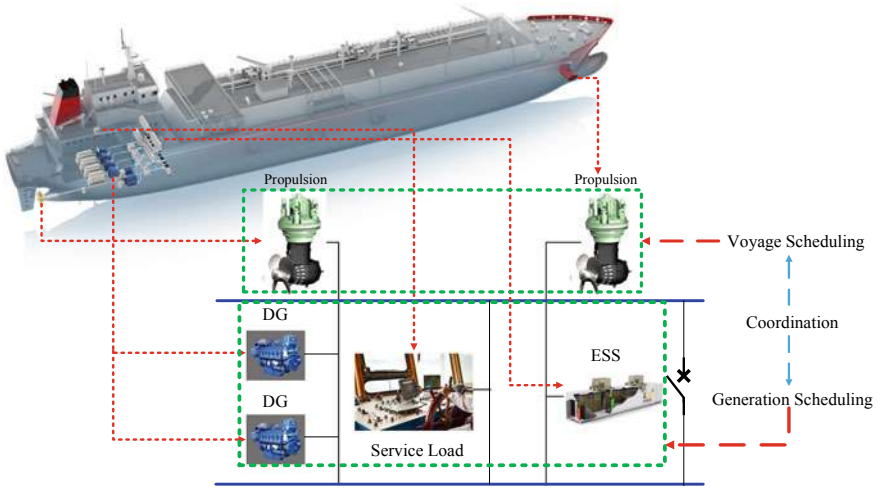

Fig. 5.18 Coordinated generation-voyage scheduling. Reprinted from [57], with permission from Elsevier

5.5.2 *Energy Management for Navigation Uncertainties in AES*

(1) Problem formulation

Besides the above PV power uncertainties, the navigation uncertainties are also commonly faced during the operation of AES. Fang and Xu [57] has studied this problem in detail, which is illustrated below. As shown in Fig. 5.18, the shipboard microgrid of an AES consists of DGs and ESS to meet the propulsion and service loads.

Compared with the conventional land-based microgrids, the AES (mobile microgrid) has the total voyage distance to the ports as a mandatory requirement, and therefore put extra constraints on the cruising speed of AES, as well as on the propulsion load. The generation scheduling aims to an economic energy scheme and the voyage scheduling aims to a punctual energy scheme. Both of them consist of a coordinated generation-voyage scheduling problem.

The speed loss when considering navigation uncertainties can be calculated by (5.1)–(5.4). The uncertainty set of the proposed model is formulated as following (4.13).

In this section, the wave height h, wavelength τ, weather direction angle θ and wind speed v^{wind} are four uncertain variables. In (4.13), $\overline{h_t}$, $\overline{\tau_t}$ and $\overline{v_t^{wind}}$ are the expectations of corresponding uncertain variables; $\underline{\mu}$ and $\bar{\mu}$ are the lower and upper budgets of the uncertainty set, when the lower budget falls and the upper budget rises, it means that the uncertainty set can cover higher uncertainty, leading to a higher robustness degree. Then the robust model shown in (5.6) is utilized to consider the worst influence by the navigation uncertainties.

$$\mathcal{U} = \left\{ \begin{array}{c} h_t \in \mathbb{R}^{|\mathcal{T}|} : h^{min} \le h_t \le h^{max}, \forall t \in \mathcal{T} \\ \underline{\mu^h} \le \sum_{t\in\mathcal{T}} h_t \Big/ \sum_{t\in\mathcal{T}} \overline{h_t} \le \overline{\mu^h} \\ \tau_t \in \mathbb{R}^{|\mathcal{T}|} : \tau^{min} \le \tau_t \le \tau^{max}, \forall t \in \mathcal{T} \\ \underline{\mu^\tau} \le \sum_{t\in\mathcal{T}} \tau_t \Big/ \sum_{t\in\mathcal{T}} \overline{\tau_t} \le \overline{\mu^\tau} \\ v_t^{wind} \in \mathbb{R}^{|\mathcal{T}|} : v_{min}^{wind} \le v_t^{wind} \le v_{max}^{wind} \\ \underline{\mu^v} \le \sum_{t\in\mathcal{T}} v_t^{wind} \Big/ \sum_{t\in\mathcal{T}} \overline{v_t^{wind}} \le \overline{\mu^v} \\ \vartheta \in \left[0, 180^o\right] : \theta_t = \varsigma \cdot \vartheta, \forall \varsigma \le 180/\vartheta \in \mathbb{N} \end{array} \right\} \tag{5.13}$$

(2) Case study

To test the effects of proposed robust model on the on-time rates, 500 water current scenarios are randomly sampled according to uniform distributions in each time-interval, denoted as $\left(h_{l,t}, \tau_{l,t}, v_{l,t}^{wind}\right)$, $t = 1 \sim 24$, $i = 1 \sim 500$. Robust 1 (The formulated robust model considering navigation uncertainties, abbreviated as R1) and Non-robust (conventional coordinated generation-voyage scheduling without navigation uncertainties, abbreviated as NR1) are set as operating strategies, respectively. The corresponding voyage distances of each sample at the scheduled time under $\theta = 30^o$ are shown in Fig. 5.19. The cruising speed and EEOI are shown in Fig. 5.20. The generation scheduling schemes are shown in Fig. 5.21. The worst speed loss and the corresponding on-time rates under different θ with or without wind are shown in Fig. 5.22.

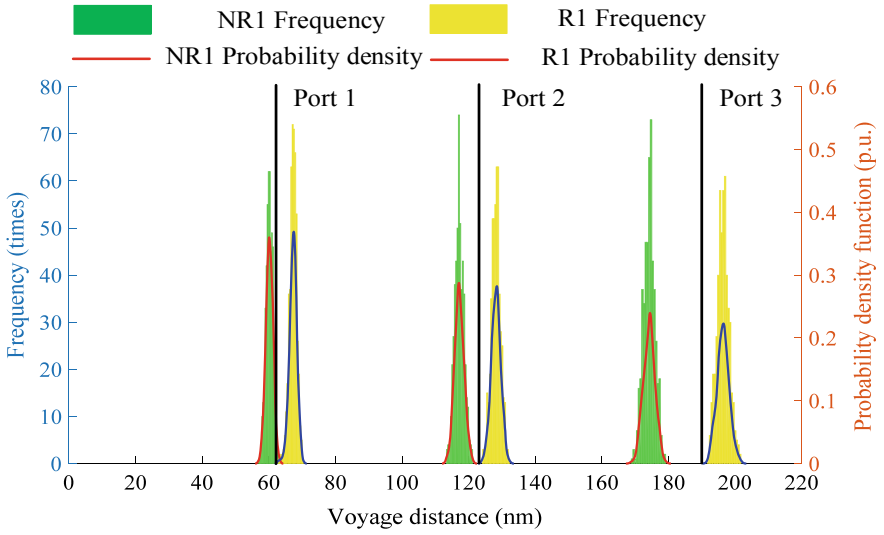

Fig. 5.19 On-time rates of different voyage schedules. Reprinted from [57], with permission from Elsevier

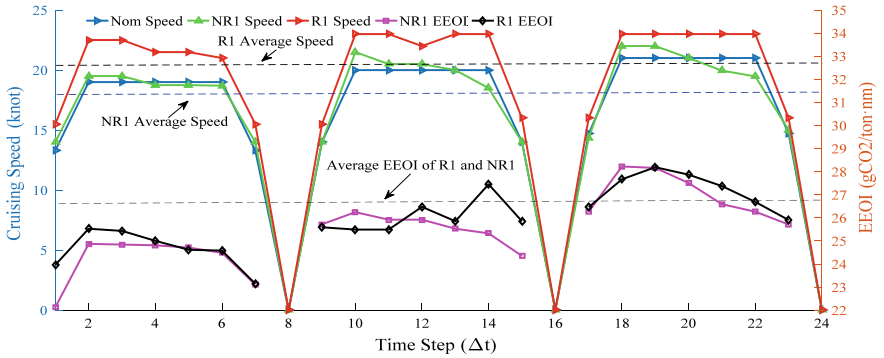

Fig. 5.20 Comparisons between NR1 and R1. Reprinted from [57], with permission from Elsevier

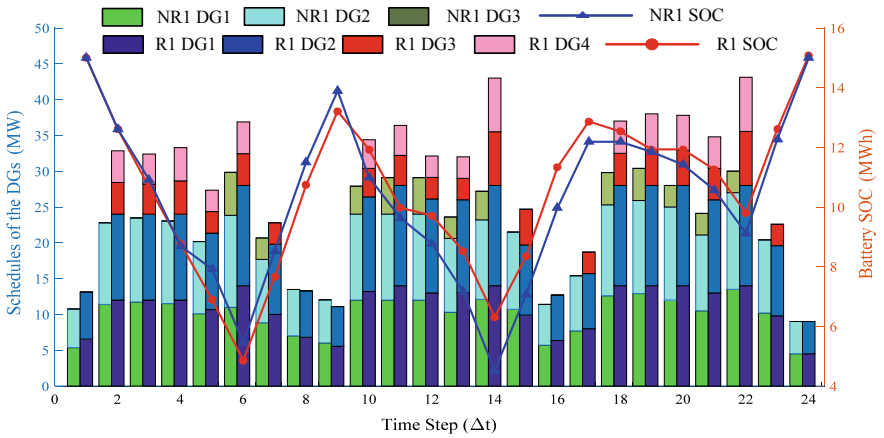

Fig. 5.21 Scheduling schemes of DGs and ESS of NR1 and R1. Reprinted from [57], with permission from Elsevier

Figure 5.19 clearly shows that the influences of uncertain water and wind will constantly accumulate during the voyage, which leads to an average 13 nm delay, leading to a 0% on-time rate of NR1 at the terminal port. However, the proposed robust model can accommodate these uncertainties by adjusting the outputs of the DGs and ESS. Accordingly, the corresponding on-time rates of R1 to each port are all 100%.

The reason to ensure the on-time rates of proposed method can be inferred from Figs. 5.20 and 5.21. The first berthing time-interval, $t = 0$, is not included in the analysis since the cruising speed and corresponding propulsion load are both zeros.

In Fig. 5.20, the cruising speed of robust model is higher than non-robust model, so able to cover the speed loss led by the wave and wind. Higher cruising speed suggests heavier propulsion load, so the corresponding outputs of DGs are all increased to meet the power demand increments, which leads to a higher FC. Specifically, in

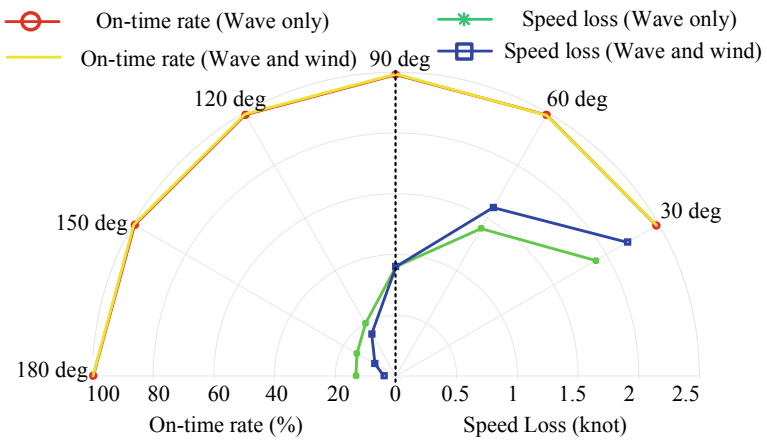

Fig. 5.22 Worst speed loss and corresponding on-time rates. Reprinted from [57], with permission from Elsevier

Fig. 5.21, NR1 uses no more than 3 DGs all the time, even 2 DGs in $t = 1 \sim 5, 8, 9, 15 \sim 17, 23, 24$. Correspondingly, R1 uses 4 DGs in most time during the voyage, only except the partial speed time-intervals, $t = 1, 7 \sim 9, 15 \sim 17, 23, 24$.

Figure 5.22 shows the worst speed loss and corresponding on-time rates. The yellow and red curves show that the proposed method can ensure a 100% on-time rate for all uncertain scenarios. The green curves show that the water wave always has negative impacts on the cruising speed, but the effect will gradually fade with the increment of the weather direction angle, which leads to the speed loss reductions.

Besides, it can be observed from Fig. 5.22 that, unlike water wave, the wind has quite different impacts on the speed loss in different scenarios, e.g. when $\theta \in [30°, 90°]$, the wind will increases speed loss, while when $\theta \in [90°, 180°]$, the wind can reduce speed loss. Especially when $\theta = 150°$ and $180°$, the speed loss under wave and wind are less than 0.5knot, thereby its negative impacts on the voyage scheduling can be greatly reduced. This is also the key reason for the cruising ships to choose their navigation route to the leeward side of wind.

References

1. Kim, M.: Estimation of added resistance and ship speed loss in a seaway. Ocean Eng. **141**, 465–476 (2017)
2. Harvald, S.A.: Resistance and propulsion of ships. Krieger Publishing Company, P.O. Box 9542, Melbourne, FL United States (1992)
3. Shao, W., Zhou, P., Thong, S.K.: Development of a novel forward dynamic programming method for weather routing. J. Mar. Sci. Technol. **17**(2), 239–251 (2012)
4. Padhy, C.P., Sen, D., Bhaskaran, P.K.: Application of wave model for weather routing of ships in the North Indian Ocean. Nat. Hazards **44**(3), 373–385 (2008)

5. Lin, Y.H., Fang, M.C., Yeung, R.W.: The optimization of ship weather-routing algorithm based on the composite influence of multi-dynamic elements. Appl. Ocean Res. **43**, 184–194 (2013)
6. Krata, P., Szlapczynska, J.: Ship weather routing optimization with dynamic constraints based on reliable synchronous roll prediction. Ocean Eng. **150**, 124–137 (2018)
7. Lai, K., Illindala, M.: Graph theory based shipboard power system expansion strategy for enhanced resilience. IEEE Trans. Ind. Appl. **54**(6), 5691–5699 (2018)
8. Xu, Q., Yang, B., Han, Q., et al.: Optimal power management for failure mode of MVDC microgrids in all-electric ships. IEEE Trans. Power Syst. **34**(2), 1054–1067 (2018)
9. Louit, D., Pascual, R., Banjevic, D., et al.: Optimization models for critical spare parts inventories—a reliability approach. J. Oper. Res. Soc. **62**(6), 992–1004 (2011)
10. Evans, P.M., Schultz, R.D.: Rotating electrical machine with electromagnetic and permanent magnet excitation. U.S. Patent 5,663,605. 1997-9-2
11. Sebille, D., Westerholt, E.: Control device for a reversible rotating electrical machine. U.S. Patent 7,102,304. 2006-9-5
12. Iris, Ç., Lam, J.S.: A review of energy efficiency in ports: Operational strategies, technologies and energy management systems. Renew. Sustain. Energy Rev. **112**, 170–182 (2019)
13. Jurong Port starts world's largest port-based solar facility. https://www.businesstimes.com.sg/energy-commodities/jurong-port-starts-worlds-largest-port-based-solar-facility
14. Man Diesel & Turbo, Basic principal of ship propulsion, 2012, Technical Report
15. Kim, M., Hizir, O., Turan, O., et al.: Estimation of added resistance and ship speed loss in a seaway. Ocean Eng. **141**, 465–476 (2017)
16. Sumalee, A., Uchida, K., Lam, W.: Stochastic multi-modal transport network under demand uncertainties and adverse weather condition. Transp. Res. Part C: Emerg. Technol. **19**(2), 338–350 (2011)
17. Sprenger, F., Maron, A., Delefortrie, G., et al.: Experimental studies on seakeeping and maneuverability of ships in adverse weather conditions. J. Ship Res. **61**(3), 131–152 (2017)
18. Hoven, V.: Power spectrum of horizontal wind speed in the frequency range from 0.0007 to 900 cycles per hour. J. Meteorol. **14**(2), 160–164 (1957)
19. Yao, J., Li, H., Liao, Y., et al.: An improved control strategy of limiting the DC-link voltage fluctuation for a doubly fed induction wind generator. IEEE Trans. Power Electron. **23**(3), 1205–1213 (2008)
20. Jiang, Q., Gong, Y., Wang, H.: A battery energy storage system dual-layer control strategy for mitigating wind farm fluctuations. IEEE Trans. Power Syst. **28**(3), 3263–3273 (2013)
21. Li, X., Hui, D., Lai, X.: Battery energy storage station (BESS)-based smoothing control of photovoltaic (PV) and wind power generation fluctuations. IEEE Trans. Sustain. Energy **4**(2), 464–473 (2013)
22. Kavasseri, R., Seetharaman, K.: Day-ahead wind speed forecasting using f-ARIMA models. Renew. Energy **34**(5), 1388–1393 (2009)
23. Li, G., Shi, J.: On comparing three artificial neural networks for wind speed forecasting. Appl. Energy **87**(7), 2313–2320 (2010)
24. Shi, J., Lee, W., Liu, Y., et al.: Forecasting power output of photovoltaic systems based on weather classification and support vector machines. IEEE Trans. Ind. Appl. **48**(3), 1064–1069 (2012)
25. Fernandez-Jimenez, L., Muñoz-Jimenez, A., Falces, A., et al.: Short-term power forecasting system for photovoltaic plants. Renew. Energy **44**, 311–317 (2012)
26. Li, J., Liu, Y., Wu, L.: Optimal operation for community-based multi-party microgrid in grid-connected and islanded modes. IEEE Trans. Smart Grid **9**(2), 756–765 (2016)
27. Kanellos, F.D., Volanis, E., Hatziargyriou, N.D.: Power management method for large ports with multi-agent systems. IEEE Trans. Smart Grid **10**(2), 1259–1268 (2017)
28. Moya, O.: A spinning reserve, load shedding, and economic dispatch solution by Bender's decomposition. IEEE Trans. Power Syst. **20**(1), 384–388 (2005)
29. Jaefari-Nokandi, M., Monsef, H.: Scheduling of spinning reserve considering customer choice on reliability. IEEE Trans. Power Syst. **24**(4), 1780–1789 (2009)

30. Banzo, M., Ramos, A.: Stochastic optimization model for electric power system planning of offshore wind farms. IEEE Trans. Power Syst. **26**(3), 1338–1348 (2010)
31. Abbey, C., Joós, G.: A stochastic optimization approach to rating of energy storage systems in wind-diesel isolated grids. IEEE Trans. Power Syst. **24**(1), 418–426 (2008)
32. Alqurashi, A., Etemadi, A., Khodaei, A.A.: Treatment of uncertainty for next generation power systems: State-of-the-art in stochastic optimization. Electric Power Syst. Res., **141**, 233–245 (2016)
33. Peng, C., Xie, P., Pan, L., et al.: Flexible robust optimization dispatch for hybrid wind/photovoltaic/hydro/thermal power system. IEEE Trans. Smart Grid **7**(2), 751–762 (2015)
34. Bertsimas, D., Litvinov, E., Sun, X., et al.: Adaptive robust optimization for the security constrained unit commitment problem. IEEE Trans. Power Syst. **28**(1), 52–63 (2012)
35. Minoux, M.: On robust maximum flow with polyhedral uncertainty sets. Optim. Lett. **3**(3), 367–376 (2009)
36. Ben-Tal, A., Nemirovski, A.: Robust solutions of uncertain linear programs. Oper. Res. Lett. **25**(1), 1–13 (1999)
37. Epanechnikov, V.: Non-parametric estimation of a multivariate probability density. Theory Probab. Appl. **14**(1), 153–158 (1969)
38. Xu, X., Yan, Z., Xu, S.: Estimating wind speed probability distribution by diffusion-based kernel density method. Electr. Power Syst. Res. **121**, 28–37 (2015)
39. Yuan, Y., Wang, J., Zhou, K., et al.: Monthly unit commitment model coordinated short-term scheduling and efficient solving method for renewable energy power system. Proc. CSEE **39**(18), 5336–5345 (2019)
40. Akhavan-hejazi, H., Mohsenian-rad, H.: Energy storage planning in active distribution grids: a chanceconstrained optimization with non-parametric probability functions. IEEE Trans. Smart Grid **9**(3), 1972–1985 (2016)
41. Kulkarni, V.: Modeling and Analysis of Stochastic Systems. CRC Press (2016)
42. Safta, C., Chen, R., Najm, H., et al.: Efficient uncertainty quantification in stochastic economic dispatch. IEEE Trans. Power Syst. **32**(4), 2535–2546 (2016)
43. Li, J., Ou, N., Lin, G., et al.: Compressive sensing based stochastic economic dispatch with high penetration renewables. IEEE Trans. Power Syst. **34**(2), 1438–1449 (2018)
44. Hu, Z., Xu, Y., Korkali, M., et al.: Uncertainty quantification in stochastic economic dispatch using Gaussian process emulation. 2020 IEEE Power & Energy Society Innovative Smart Grid Technologies Conference (ISGT), pp. 1–5. IEEE (2020)
45. Chen, Y., Wang, Y., Kirschen, D., et al.: Model-free renewable scenario generation using generative adversarial networks. IEEE Trans. Power Syst. **33**(3), 3265–3275 (2018)
46. Kong, W., Dong, Z., Jia, Y., et al.: Short-term residential load forecasting based on LSTM recurrent neural network. IEEE Trans. Smart Grid **10**(1), 841–851 (2017)
47. Hossain, M., Mekhilef, S., Danesh, M., et al.: Application of extreme learning machine for short term output power forecasting of three grid-connected PV systems. J. Clean. Prod. **167**, 395–405 (2017)
48. Li, P., Guan, X., Wu, J., et al.: Modeling dynamic spatial correlations of geographically distributed wind farms and constructing ellipsoidal uncertainty sets for optimization-based generation scheduling. IEEE Trans. Sustain. Energy **6**(4), 1594–1605 (2015)
49. Kumar, P., Yildirim, E.: Minimum-volume enclosing ellipsoids and core sets. J. Optim. Theory Appl. **126**(1), 1–21 (2005)
50. Ding, T., Lv, J., Bo, R., et al.: Lift-and-project MVEE based convex hull for robust SCED with wind power integration using historical data-driven modeling approach. Renew. Energy **92**, 415–427 (2016)
51. Velloso, A., Street, A., Pozo, D., et al.: Two-stage robust unit commitment for co-optimized electricity markets: An adaptive data-driven approach for scenario-based uncertainty sets. IEEE Trans. Sustain. Energy **11**(2), 958–969 (2019)
52. Fang, S., Xu, Y., Wen, S., et al.: Data-driven robust coordination of generation and demand-side in photovoltaic integrated all-electric ship microgrids. IEEE Trans. Power Syst. **35**(3), 1783–1795 (2019)

53. Wen, S., Lan, H., Hong, Y.Y., et al.: Allocation of ESS by interval optimization method considering impact of ship swinging on hybrid PV/diesel ship power system. Appl. Energy **175**, 158–167 (2016)
54. Wan, C., Lin, J., Song, Y., et al.: Probabilistic forecasting of photovoltaic generation: An efficient statistical approach. IEEE Trans. Power Syst. **32**(3), 2471–2472 (2016)
55. Kanellos, F.D., Tsekouras, G.J., Prousalidis, J.: Onboard DC grid employing smart grid technology: challenges, state of the art and future prospects. IET Electr. Syst. Transp. **5**(1), 1–11 (2014)
56. Patel, M.R.: Shipboard Electrical POWER Systems. CRC Press (2011)
57. Fang, S., Xu, Y.: Multi-objective robust energy management for all-electric shipboard microgrid under uncertain wind and wave. Int. J. Electr. Power Energy Syst. **117**, 105600 (2020)

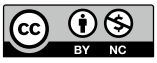

Chapter 6
Energy Storage Management of Maritime Grids

6.1 Introduction to Energy Storage Technologies

Energy is an essential commodity and a key element for global development, and generally comes from various sources and can be mainly classified as two types, (1) the primary forms of energy and (2) the secondary forms of energy. The primary forms of energy are those energy sources that only involve extraction or capture, and the energy directly comes from nature. Typical examples are crude oil, coal, various renewable energy, natural uranium, and falling or flowing water. On the other hand, the secondary forms of energy include all the energy forms after the transformation from the primary forms of energy. The relationship between the primary forms and the secondary forms are shown in Fig. 6.1.

Secondary energy forms are generally more convenient to use and usually viewed as "energy carriers", including various types of petroleum, diesel, and electricity. The transformation technologies include oil refinery, thermal power plants, nuclear power plants, solar power plants, and so on. Among all the secondary forms of energy, electricity is the main "energy carrier" for daily lives, and power system is the corresponding man-made network to generate, transmit, and distribute electricity. Conventionally, the generation-side and demand-side of power system should be equal all the time since the electricity cannot be stored. Nowadays, with large scale of energy storage, power system will have more flexibility since energy storage can change its roles between the generation-side and the demand-side.

As a special type of power system, maritime grids also complete similar roles of "generate-transmit-distribute" as conventional power systems. For example, a seaport microgrid purchases electricity from the upper grid, and the electricity transmits to the seaport via the main substation and then distributes to different equipment within the seaport. Similarly in ships, the main and auxiliary engines generate electricity and

S. Fang and H. Wang, *Optimization-Based Energy Management for Multi-energy Maritime Grids*, Springer Series on Naval Architecture, Marine Engineering, Shipbuilding and Shipping 11, https://doi.org/10.1007/978-981-33-6734-0_6

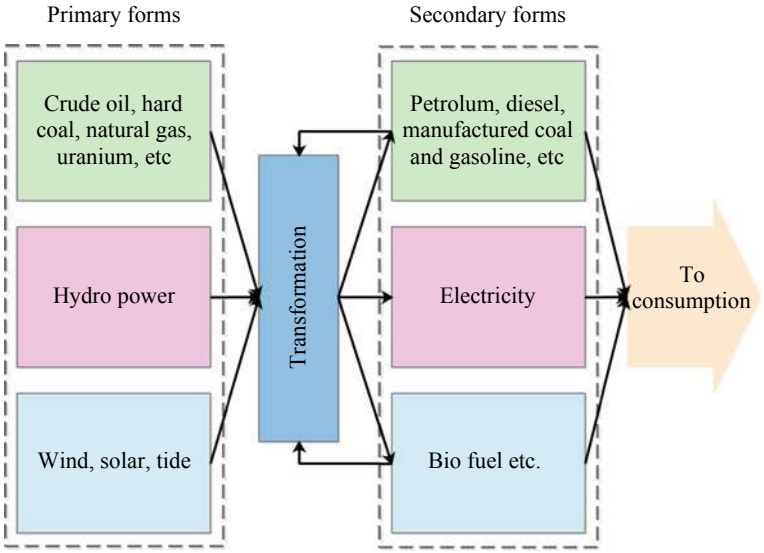

Fig. 6.1 Primary and secondary energy [1]

the electricity is transmitted and distributed by the shipboard microgrid to various load demands. In this sense, energy storage also plays an essential role to facilitate the optimal operation of maritime grids.

For ships, in [2, 3], energy storage is coordinated with the propulsion system of an AES to achieve better economic and environmental targets. Then in [4], energy storage is used to supply the energy consumption of the shipboard gas capture system. In short-term timescale, [5–7] use energy storage to mitigate propulsion fluctuations. For seaports, [8–10] classify the energy storage as an individual agent and has its energy plans to participate in the seaport operation. Molavi et al. [11] uses energy storage to facilitate renewable energy integration. Later on, [12, 13] use energy storage to recover the energy when the lifting-down of port cranes. The above literature has clearly shown that energy storage has already been an important device in maritime grids, and proper management is essential for maritime grids.

This Chapter focuses on this topic and is organized as follows. Section 6.2 gives the characteristics of different energy storage technologies, and Sect. 6.3 gives several application cases of energy storage in maritime grids. At last, Sect. 6.4 analyzes two typical problems to demonstrate the effects of energy storage management.

6.2 Characteristics of Different Energy Storage Technologies

6.2.1 Classifications of Current Energy Storage Technologies

In this section, Fig. 1.13 is re-drawn here to show the classifications of energy storage and denoted as Fig. 6.2. This Chapter focuses on conventional energy storage technologies and fuel cell will be discussed in detail in Chap. 8. The nomenclature of various energy storage technologies is shown in Table 6.1.

In the following Table 6.2, the characteristics of different energy storage are given. Since the different characteristics, we can find that different energy storage has

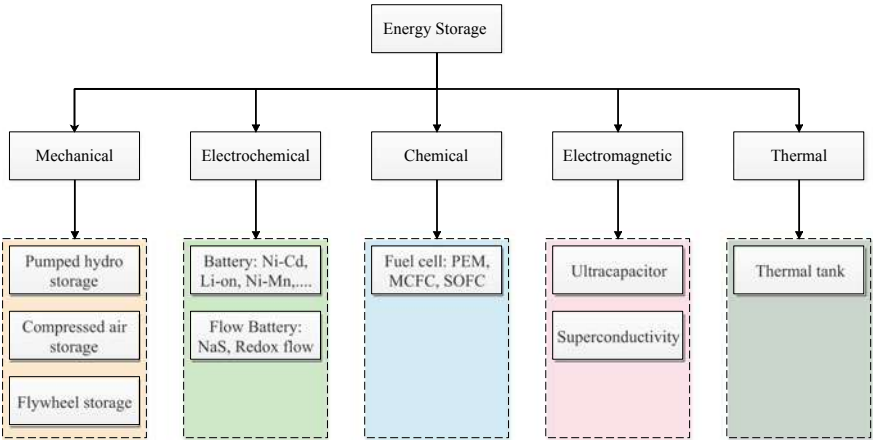

Fig. 6.2 Classification of energy storage

Table 6.1 Nomenclature of different energy storage technologies

BES: Battery Energy Storage	ZBB: Zinc-bromine flow battery
CAES: Compressed Air Energy Storage	NaS: Sodium-sulfur
FBES: Flow Battery Energy Storage	Ni-Cd: Nickel-cadmium
FESS: Flywheel Energy Storage	PSB: Polysulfide bromide battery
Li-ion: Lithium-ion	PHS: Pumped hydro storage
SMES: Superconducting magnetic energy storage	PEM: Proton exchange membrane
SCES: Supercapacitor energy storage	VRB: Vanadium redox battery

Table 6.2 Characteristics of different energy storage [14, 15]

Technologies	Investment (US$/kWh)	Energy rating (MWh)	Power rating (MW)	Specific energy (kWh/kg)	Specific power (kW/kg)
PHS	10–15	500–8000	10–1000	–	–
CAES	2–4	580, 2860	50–300	3.2–5.5	–
VRB	600	1.2–60	0.2–10	25–35	166
ZBB	500	0.1–4	0.1–1	70–90	45
PSB	450	0.005–120	0.1–15	–	–
NaS	170–200	0.4–244.8	0.05–34	100	90–230
Lead-Acid	50–100	0.001–40	0.05–10	30–50	180–200
Ni-Cd	400–2400	6.75	45	30–80	100–150
Li-ion	900–1300	0.001–50	0.01–50	80–200	200–2000
SMES	200–300	0.015	1–100	10–70	400–2000
FESS	400–800	0.025–5	0.1–20	5–100	10000+
SCES	100–300	0.01	0.05–0.2	5–15	10000+

quite different application scenarios. In the following context, some energy storage technologies which are used in maritime grids are described in detail to show their applications.

6.2.2 Battery

Among current energy storage technologies, the battery is one of the most common technologies available on the market. The battery stores energy in the electrochemical form and the battery cells are connected in series or in parallel or both to make up the desired voltage and capacity. A typical battery packs' structure is shown as Fig. 6.3, and each battery cell consists of two electrodes and an electrolyte, which are sealed in a container and then integrated into the external grid or load.

In the last decade, the technologies of battery have become much more mature, such as the lead-acid battery, nickel-cadmium battery, lithium-ion battery. Especially for lead-acid batteries, which have been researched for over 140 years and is the most mature battery technology now. Currently, tremendous efforts have been carried out to turn technologies like nickel-cadmium and lithium-ion batteries into cost-effective options for higher power applications, and their lifetimes are also important research topics.

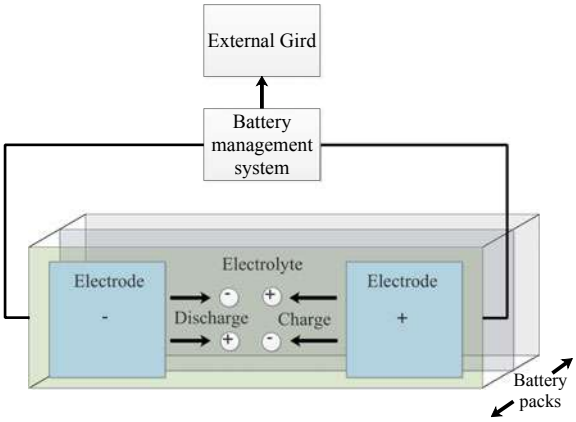

Fig. 6.3 Illustration of battery energy storage packs

6.2.3 Flywheel

FES stores energy as the form of kinetic energy in a rotating mass or rotor. The stored energy is proportional to the rotor mass, location of the mass, and the rotor's rotational speed. When FES charges, it absorbs the energy from outside and accelerates the rotating speed of mass. On the other side, when the flywheel discharges, the rotating mass drives a generator to produce electrical power, and the rotating speed slows down. An illustration of flywheel energy storage is shown in Fig. 6.4.

Compared with other types of energy storage, FES can quickly respond to the power demand, and therefore be widely used in improving the power quality, load demand peak shaving, power factor correction, and load leveling. Other applications of flywheels include UPS [16], frequency response [17], smoothing wind power [18], and heavy haul locomotives [19].

The advantages of FES can be illustrated as it provides intermediate characteristics in terms of power and energy density compared with batteries and super-capacitor,

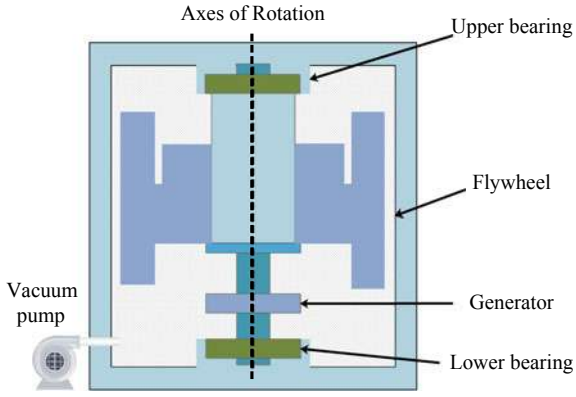

Fig. 6.4 Illustration of flywheel energy storage

i.e., the FES has much higher power density than batteries and much higher energy density than supercapacitors. Besides, FES also caters with many shortcomings of prior energy storage technologies, i.e., less sensitivity to temperature, chemical hazardless, higher life cycle, reduced space, and weight, which is suitable for many applications. But the FES also has its shortcoming, i.e., the complex maintenance process for rotating mass.

6.2.4 Ultracapacitor

Capacitors store energy in the electric field and have a quite low equivalent series-resistance that enable them to supply the power efficiently. Generally, the capacitors are used in higher power demand scenarios, including the compensation of reactive power, mitigation of load fluctuations, and power quality issues. Capacitors usually can be classified as super-capacitors, electrolytic capacitors, and electrostatic capacitors. Figure 6.5 illustrates the typical structure of a super-capacitor. The main advantages of super-capacitors are higher power density, faster charging and discharging, longer life cycles compared with other energy storage technologies. The disadvantages are the low voltage of each cell, and much higher investment cost per Watt-hour, i.e., more than 10 times compared with a lithium battery. Other drawbacks of super-capacitor include relatively low energy density, linear discharge voltage, and high self-discharge.

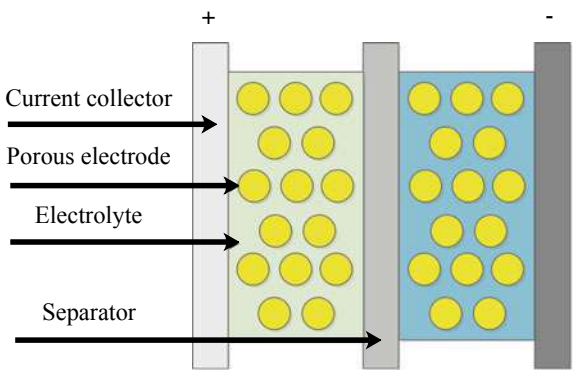

Fig. 6.5 Illustration of super-capacitor energy storage

6.3 Applications of Energy Storage in Maritime Grids

6.3.1 Roles of Energy Storage in Maritime Grids

Generally, energy storage in maritime grids has three main applications, (1) as the main energy source, and (2) for long-term load leveling, shifting or shaving; and (3) for short-term power balancing.

Using energy storage as the main energy source is a recent trend for some short-trip ferries or cargo ships. Such as the first all-electric ferry "ampere" in North Europe [20], and China's first all-electric cargo ship "puffer" in 2019 [21]. Until now, there are more than 50 ships using energy storage as the main energy source in Europe. The biggest capacity is 4.16 MWh (Li-ion), the smallest capacity is 0.02 MWh (Lead-acid). The all-electric ships are about to develop in China and there will be more ships launched in the future. The advantage of using energy storage as the main energy source is nearly zero-emission, but the disadvantage is also obvious, i.e., the capacity of current energy storage technologies is limited to individually sustain a large ship for a long-distance voyage. Similar in seaports and other ocean platforms, the capacity of current energy storage is just enough to serve as auxiliary equipment. In this sense, the main application scenarios of energy storage are still in the long-term load leveling and short-term power balancing.

For the long-term load leveling, the energy storage should have enough energy density to sustain a long-time discharging. Battery is generally the main equipment to undertake this task. Nowadays, many maritime grids have installed energy storage as essential auxiliary equipment for better system characteristics. Two recent examples in China are provided as following Fig. 6.6.

The first example is the emergency supporting ship launched on April, 28th, 2020 in Shenzhen [22]. This ship has a length of 78 m and 12.8 m breadth. The deadweight is 1450 tons. The propulsion system has three diesel generators (3 × 2080 kW) and

(a) "Deep ocean 01" ship (b) Lianyungang port

Fig. 6.6 Two cases for energy storage integration in maritime grids

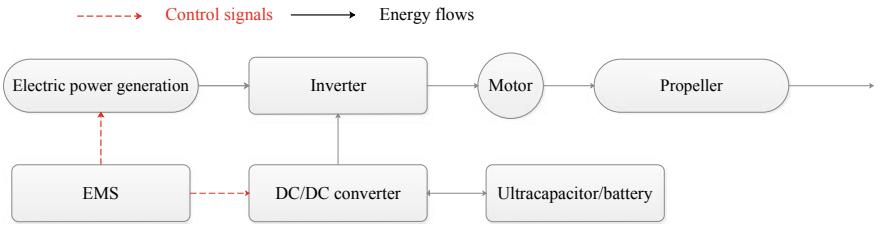

Fig. 6.7 Schematic of an electric propulsion system with ultracapacitor

two Li-ion batteries (2 × 750 kW). The second example is in Lianyungang Port which plans a battery installment (1 MW ultracapacitor + 4 MW Li-ion battery) for cold-ironing services [23]. The above two examples are both using energy storage for long-term load-leveling (hours or even longer).

For short-term power balancing, energy storage should have enough power density. This task is usually undertaken by the ultracapacitor [5] or flywheel [6], since they have enough power density and can quickly respond to the power fluctuations. Jiang et al. [24] gives a schematic of electric propulsion system with ultracapacitor, which is shown as Fig. 6.7.

In Fig. 6.7, the EMS sends control signals to the electric power generation and DC/DC converter to determine their power outputs. Then the electric power generation and ultracapacitor are both used to supply the propeller.

The applications of energy storage in maritime grids are briefly described above. To further clarify the applications, three scenarios are selected and analyzed in detail, i.e., navigation uncertainties and demand response, renewable energy integration, and energy recovery.

6.3.2 Navigation Uncertainties and Demand Response

Chapters 3 and 4 have discussed the influences of navigation uncertainties on the maritime grids. To mitigate these uncertainties, maritime grids should reserve a certain "sea margin" or "spinning margin" which can quickly respond [25]. For a maritime grid, the influences of navigation uncertainties can be described as the changes in load demands. Figure 6.8 gives an example of how energy storage mitigates the navigation uncertainties.

From the following Fig. 6.8a, the total power demand has two peaks. The main energy source need to suffer fast ramping-ups/ramping-downs, or frequent shut-downs/start-ups to follow the power demand. The influences of navigation uncertainties are similar to Fig. 6.8a, i.e., leading to many peak loads. When integrating energy storage, the main energy source and energy storage can share the total power demand, shown as Fig. 6.8b. The charging/discharging of energy storage can smooth the power demand and make the main energy source working in a steady-state, and

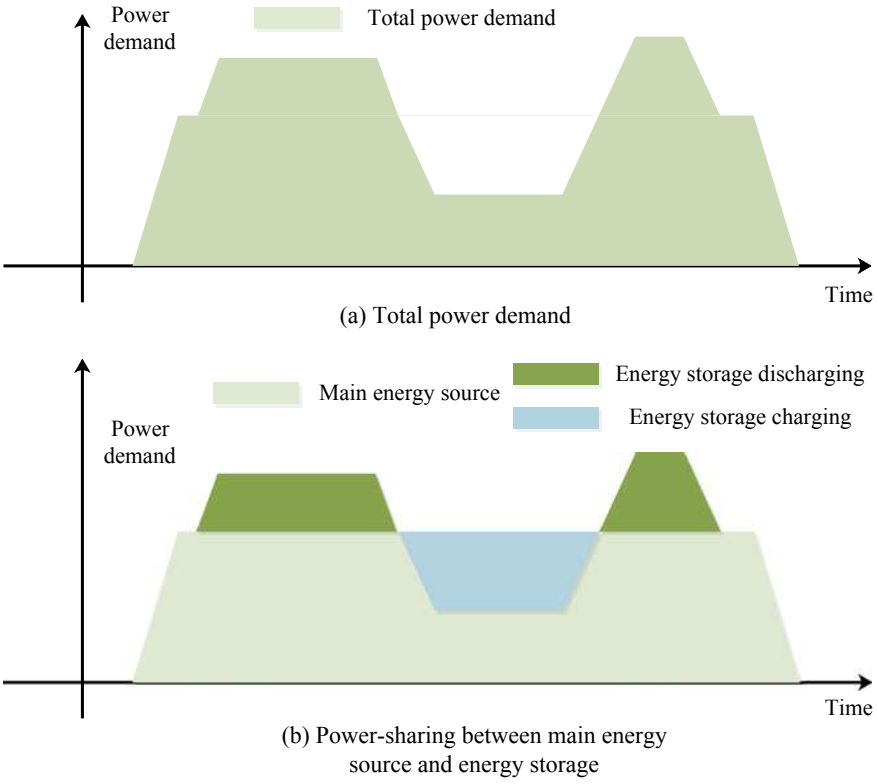

Fig. 6.8 Power sharing by energy storage

the economic and environmental behaviors may be both improved. In this sense, energy storage integration has been viewed as an important approach to facilitate the operation of maritime grids.

It should be noted that energy storage can level/smooth other types of power demand in maritime grids as well, such as service load [3], or weapon system [26], and even in some short-term timescale applications [5–7]. In those applications, the effects are similar to Fig. 6.8a, b, i.e., the main energy source keeps a nearly constant power output and the energy storage shares the fluctuated load demand by continuous discharging/charging. This advantage also gives a new requirement for energy storage management, i.e., the energy storage should coordinate with the main energy source to achieve economic and environmental tasks.

6.3.3 Renewable Energy Integration

To resolve the bottleneck of energy efficiency problems in maritime grids, renewable energy has been gradually integrated into and may soon become an essential part of maritime grids. However, as we have mentioned in Chaps. 1 and 4, the renewable energy is less controllable compared with conventional energy, and the power outputs are generally fluctuating all the time and cannot be accurately forecasted. There are many routes to mitigate the influences of renewable energy and energy storage integration is an important way [24, 27, 28]. Reference [24] gives a schematic diagram of battery energy storage to mitigate the wind power fluctuations, which is shown in Fig. 6.9.

From Fig. 6.9, the battery units are installed with the wind turbine in parallel. Two layers of control strategy are used to determine the battery power for compensating the wind power fluctuation. In the first layer, the wind power is measured and the fluctuation mitigation control layer determines the compensating power. Then the power allocation control layer split the power into each battery unit, including the charging/discharging states and power values. With this compensation, the power output fluctuation of a wind turbine can be greatly reduced.

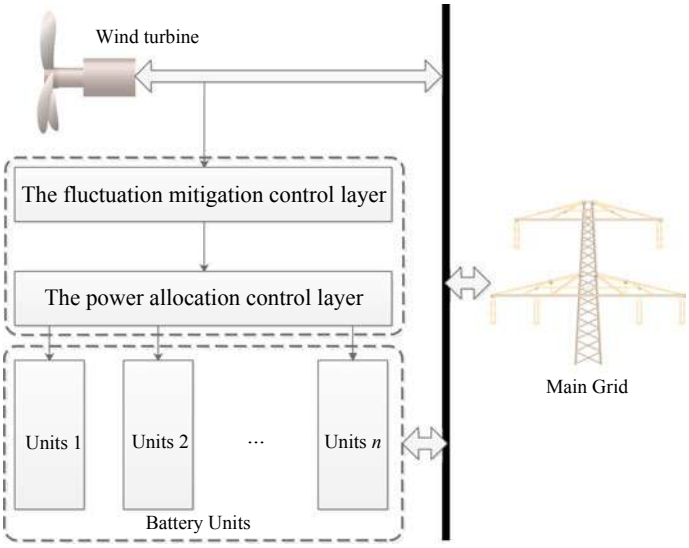

Fig. 6.9 Power sharing by energy storage [24]

6.3.4 *Energy Recovery for Equipment*

With the electrification of various equipment in maritime grids, energy storage can be used as an energy buffer to recover the wasted energy for later usage. Binti Ahamad et al. [13] has studied the energy recovery by energy storage for an electrified port crane. Figure 6.10 shows 8 working steps for an electrified port crane. The corresponding power demand is shown in Fig. 6.11.

A typical working process of a port crane includes (1) hoist, or beginning to lift up; (2) lifting up speedily; (3) lifting up speedily and the trolley moving forward; (4) lifting up with the full speed and the trolley moving forward; (5) lifting up with slowing speed and the trolley moving with full speed; (6) the trolley moving with slowing speed; (7) lifting down speedily and the trolley moving with slowing speed; (8) settling down. Step (2) and (3) usually have the biggest power demand whereas steps (6), (7) and (8) have smaller power demands. Furthermore, when the cargo is lifting down, the gravitational potential of cargo is wasted, which accounts for about 20% of the total energy consumption [13].

Reference [13] uses a flywheel to store the energy when the cargo is lifting down. The entire process consists of three modes, including mode 1: grid provides power and flywheel discharge; mode 2: grid provides power and flywheel charges; and mode 3: crane charges the flywheel, and three modes are shown in Fig. 6.12. The fourth sub-figure shows the operating cycle of the flywheel.

In Fig. 6.12, mode 1 is used when the power demand is high, and mode 2 is used when the power demand is low, and mode 3 is used when the cargo is lifting down.

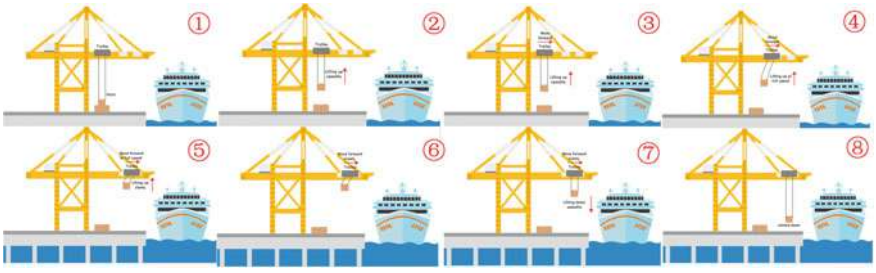

Fig. 6.10 Typical working steps for a port crane

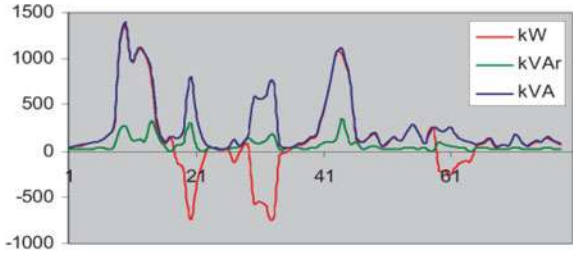

Fig. 6.11 Power demand curves for a port crane. Reprinted from [29], open access

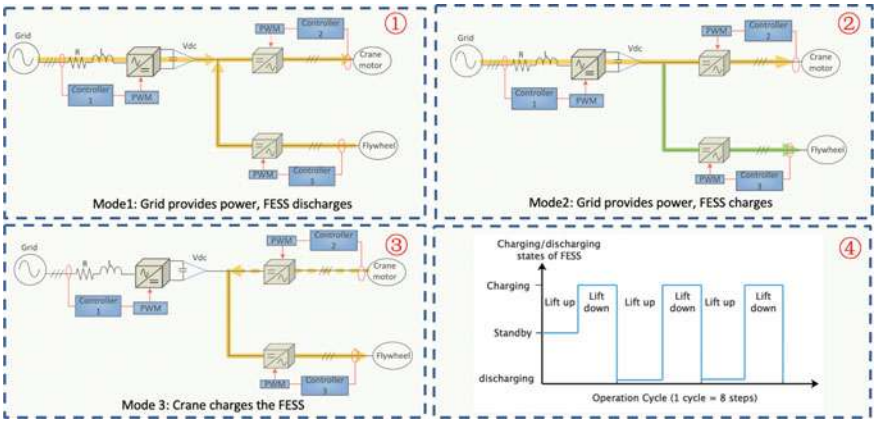

Fig. 6.12 Power demand curves for a port crane [13]

From the overall scope, the flywheel has a periodical operation pattern between "discharging-charging-standby" to recover energy. In a seaport microgrid, there will be increasing electrified equipment and many of them are used for the lifting up/lifting down cargos. Therefore energy storage will be widely used in the future.

6.4 Typical Problems

6.4.1 Energy Storage Management in AES for Navigation Uncertainties

(1) Voyage scheduling and navigation uncertainties

In general, the navigation uncertainty forecasting includes pre-voyage forecasting and intra-voyage forecasting [30]. Responding to the pre-voyage forecasting navigation uncertainties is widely known as the weather routing problems, or pre-voyage planning [30–32]. But the conventional ships are rather difficult to respond to the intra-voyage navigation uncertainties, since in conventional ships, the prime motors are connected with propellers via shafts and gearboxes, and the speed regulation ability of conventional ships are therefore limited. With the development of electric propellers, the prime motors can be "physically separated" from the propellers by the shipboard electric network. With the aid from integrated ESSs, the onboard generation of AESs can quickly and economically respond to the intra-voyage navigation uncertainties. In the future AESs, both the pre-voyage and intra-voyage navigation uncertainties should be addressed by proper energy management.

(2) Two-stage scheduling framework

As shown in Fig. 6.13, the first stage is to respond to the pre-voyage navigation uncertainties and gives the on/off states of onboard DGs, and the second stage is to respond to the intra-voyage navigation uncertainties and gives the loading factors of onboard DGs and other decision variables. The merits are as follow:

a. The two-stage operation model can respond to the pre-voyage navigation uncertainties and intra-voyage navigation uncertainties, coordinately, to gain a compromise between the robustness and flexibility, i.e., the first stage for the worst operating case (robustness) and the second stage to adapt to the current operating case (flexibility).
b. With the proposed two-stage operation, the management of onboard DGs can be more convenient, since the on/off states of onboard DGs are determined before a voyage. The arrangements of the repair or overhaul of the onboard DGs are much easier.

In the pre-voyage time-window, i.e., the first stage, the decision variables are optimized based on the pre-voyage forecasting navigation uncertainty set. The decision variables in the first stage include on/off states of onboard DGs and their loading factors, the shipboard ESS power, the propulsion load and the cruising speed. This stage is to find an optimal robust shipboard operating scheme for addressing the worst speed loss case caused by navigation uncertainties. In this stage, only the on/off states of DGs are "here-and-now" variables and remain as constants in the second stage. Other variables, including the loading factors of DGs, shipboard ESS power, propulsion load, and cruising speed are all "wait-and-see" variables, which will be re-dispatched in the second stage towards uncertainty realization. In the intra-voyage time-window, i.e., the second stage, the navigation uncertainties are treated as realized. All of the "wait-and-see" variables are re-dispatched to address the short-term navigation uncertainties.

The proposed two-stage robust model can be viewed as a "predictive-corrective" process. The first stage is the predictive process to respond to the worst-case and the second stage is the corrective process which takes recourse actions to compensate for the first stage, i.e., reducing the conservatism of the first stage.

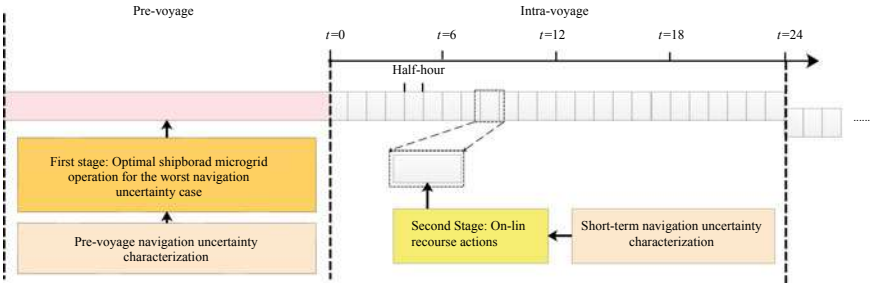

Fig. 6.13 Relation between the first and second stage of proposed model, reprinted from [33], with permission from IEEE

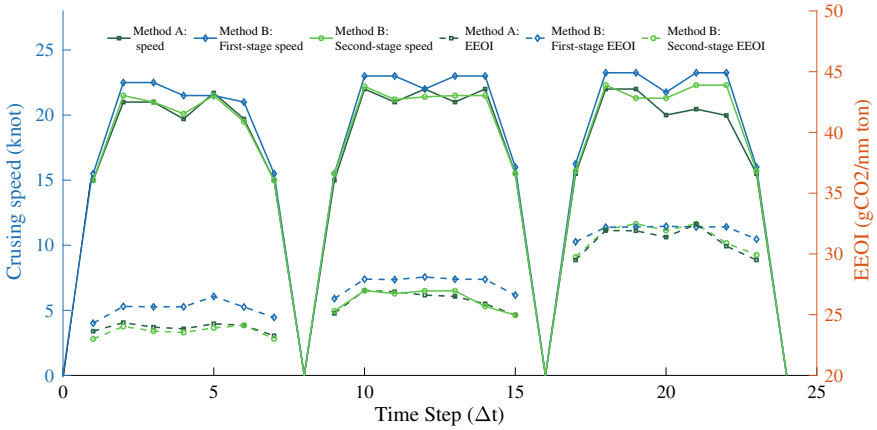

Fig. 6.14 Cruising speed and EEOI comparisons. Reprinted from [33], with permission from IEEE

(3) Case study

To test the proposed two-stage robust optimization problems. Two methods are compared as follows, and the cruising speed and EEOI comparisons are shown in Fig. 6.14.

Method A (Non-robust model): shipboard generation scheduling with the expected wave and wind.

Method B (Robust model): the proposed robust shipboard generation scheduling (first stage and second stage models). In the second stage, an uncertainty sample is selected from the uncertainty set to represent the uncertainty realization.

Firstly, the on-time rates are obtained by generating 500 navigation uncertainty samples in the uncertainty set. The voyage distance of each sample in the terminal port is shown in Fig. 6.15.

In the proposed two-stage robust model, the cruising speed will increase compared with the non-robust model since the robust model is to meet the worst case of the navigation uncertainties, meanwhile, the non-robust model only needs to cope with the expected uncertainties. In this sense, the non-robust model cannot guarantee the on-time rates of AES.

To analyze the effects of energy storage on the navigation uncertainties, the total battery power and SOC in the first and second stages are shown in Fig. 6.16.

From Fig. 6.16, since the worst-case assumed in the first stage may not happen, the total battery power is reduced in the second stage. This phenomenon also shows that the proposed two-stage model can well adapt to the uncertainties with sufficient flexibility.

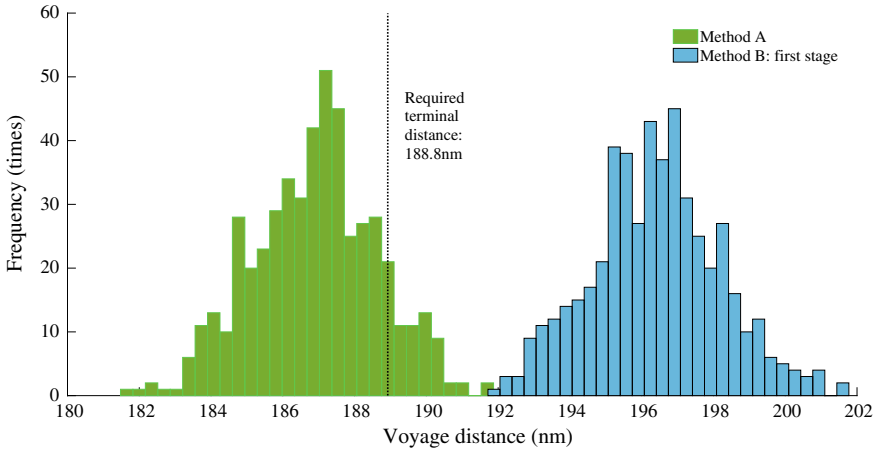

Fig. 6.15 On-time rates of robust and non-robust models. Reprinted from [33], with permission from IEEE

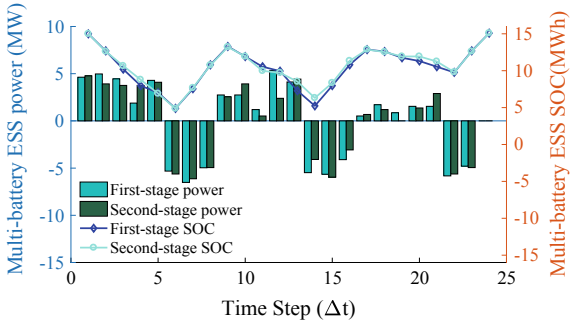

Fig. 6.16 Multi-battery ESS scheme in first and second stages. Reprinted from [33], with permission from IEEE

6.4.2 Energy Storage Management in AES for Extending Lifetime

(1) Definitions of DoD and MSOC

In general, improper cycling conditions are the main reasons for battery degradation, i.e., charging/discharging cycles and the DoD in each cycle [34–37]. In recent years, the impacts of MSOC on the battery lifetime have been gradually realized, but still not been incorporated into the operation problem, yet. In fact, DoD and MSOC are two main factors we considered in the battery degradation. The DoDs and initial/terminal SOCs of battery in discharging/charging events are defined in Fig. 6.17a, b.

In Fig. 6.17, when a charging/discharging event begins, the SOC of battery is denoted as the initial SOC, and when this event terminates, the SOC is denoted as

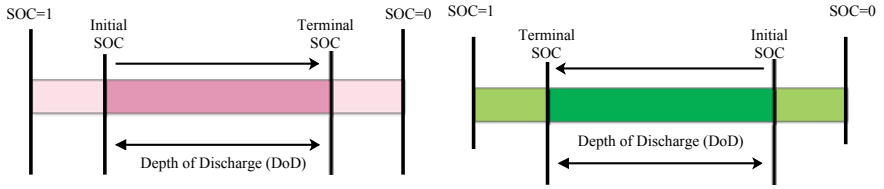

(a) Definition of DoD in discharging event

(b) Definition of DoD in charging event

Fig. 6.17 Definitions of the DoD and initial/terminal SOCs. Reprinted from [38], with permission from IEEE

the terminal SOC. The SOC variations between the initial and terminal SOCs are defined as the DoD, denoted as d. The middle point of the initial and terminal SOCs is defined as the MSOC, denoted as SOC^{mean}.

Since the ship generally has multiple batteries, for the b-th battery in the i-th charging/discharging event, the DoD is denoted as d_i^b, and the corresponding MSOC is denoted as $SOC_{b,i}^{mean}$, and the equivalent life cycle (ELC) is denoted as $ELC_{b,i} = \sum_i d_i^b$.

In the following, we use a vector to denote the MSOC-DoD combination hereafter, i.e., $(SOC_{b,i}^{mean}, d_i^b)$. For example, (0.3, 0.6) means the experiment is conducted in $SOC_{b,i}^{mean} = 0.3$ and $d_i^b = 0.6$.

(2) Impacts of DoD and MSOC on the battery lifetime

In the former section, two main factors for battery degradation have been defined, i.e., d_i^b and $SOC_{b,i}^{mean}$. In the following, a battery degradation model is formulated based on the above two factors. The original dataset is based on experimental research of battery health [39]. It has 14 aging experiments for the batteries in the same brand. The discharging/charging current in each experiment is the same and there are five MSOC-DoD combinations, i.e., (0.3, 0.6), (0.5, 0.2), (0.5, 0.6), (0.5,1), (0.7, 0.6). Several experimental data are shown in Fig. 6.18a, b. If the MSOC-DoD combination is the same, it refers to the experiment that has been conducted twice, otherwise, the experiment is only conducted for once.

In Fig. 6.18, the horizontal axis represents the ELC. The vertical axis represents the normalized battery capacity, and it will decay with the charging/discharging cycles. From above, the impacts of DoD and MSOC on the battery lifetime are clear, i.e., smaller DoD and lower MSOC lead to smaller battery degradation. The reasons are shown as follows, (1) in Fig. 6.18a, experiment 1–6 share the same MSOCs but the DoDs are different, i.e., from 0.2 to 1. As shown in the dataset, the battery with higher DoD will have faster degradation, and (2) in Fig. 6.18b, experiment 7–10 share the same DoD but the MSOC are different, from 0.3 to 0.7. As shown in the dataset, the battery with higher MSOC suffers from higher battery degradation.

To show an example for battery degradation calculation, we take the curve of experiment 6 as an example. The battery in experiment 6 has 879 cycles before life ending. Then the average degradation in each cycle in p.u. is $De_i^b = \frac{1-0.8}{879} =$

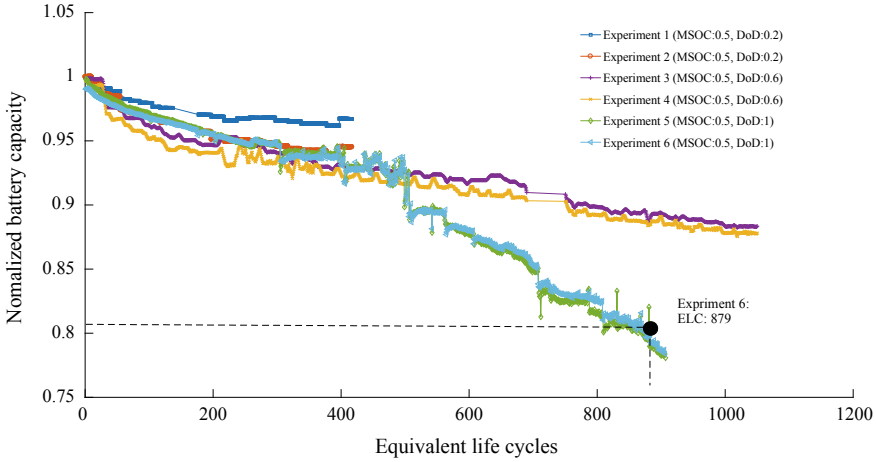

(a) Battery lifetime experiments in different DoDs

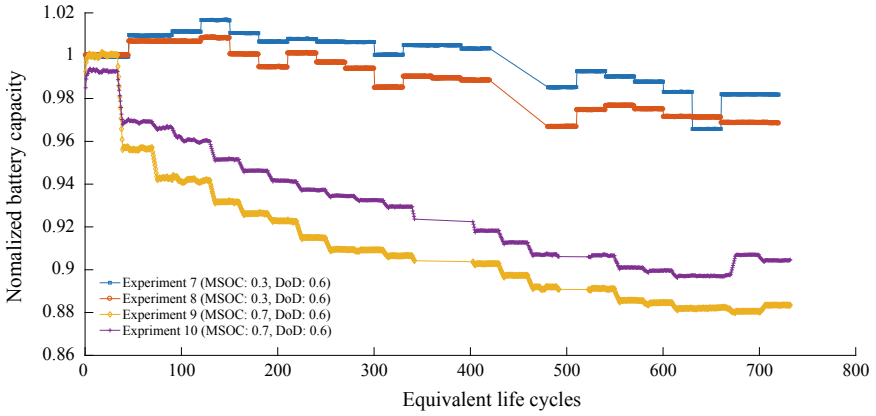

(b) Battery lifetime experiments in different MSOCs

Fig. 6.18 Experimental data illustration. Reprinted from [38], with permission from IEEE

2.2×10^{-4}. Similarly, the average degradations in each cycle for 14 experiments are calculated. For clarification, we denote the obtained battery degradation dataset as $\left(SOC_{b,i}^{mean}, d_i^b, De_i^b\right), b \in \mathcal{B}$, where De_i^b is the average battery degradation.

(3) A revised data-driven battery degradation model

According to Ref. [34], the model of battery lifetime versus DoD is shown as (6.1), where k_1, k_2 and k_3 are all fitting coefficients. To reflect the impacts of MSOC, the degradation model shown in Eq. (6.1) should be revised, and Table 6.3 shows different fitting models and their R-square parameters under the dataset [39]. The fitting tools used is the "sftool" in Matlab 2016b.

Table 6.3 Different Fitting Models and parameters

Model	Model formulation	Fitting parameters	R-square
1	$k_1 \cdot SOC_{b,i}^{mean} \cdot \left(d_i^b\right)^{k_2} \cdot e^{k_3 \cdot d_i^b}$	$k_1, k_2, k_3 = 1.475, -1.106, 3.512$	0.91
2	$k_1 \cdot \left(SOC_{b,i}^{mean}\right)^{k_2} \cdot \left(d_i^b\right)^{k_3} \cdot e^{k_4 \cdot d_i^b}$	$k_1, k_2, k_3, k_4 = 1.41, 1.1, -1.16, 3.62$	0.91
3	$k_1 \cdot e^{k_2 \cdot SOC_{b,i}^{mean}} \cdot \left(d_i^b\right)^{k_3} \cdot e^{k_4 \cdot d_i^b}$	$k_1, k_2, k_3, k_4 = 0.18, 2.0, -1.29, 3.89$	0.87

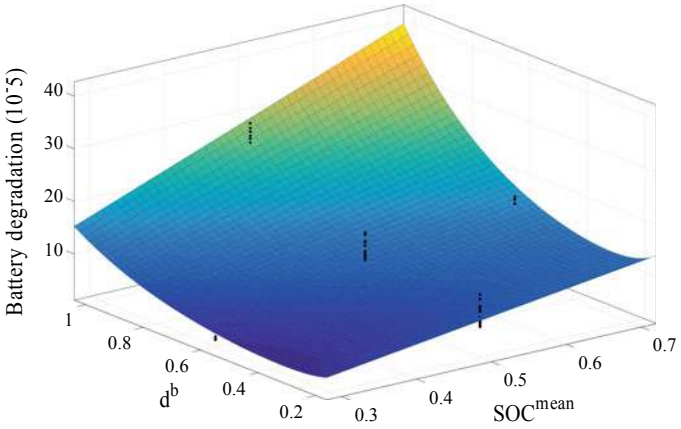

Fig. 6.19 Fitting surface of Battery degradation vs. DoD and MSOC. Reprinted from [38], with permission from IEEE

$$De_i^b = k_1 \cdot \left(d_i^b\right)^{k_2} \cdot e^{k_3 \cdot d_i^b} \tag{6.1}$$

From the results of Table 6.3, model 1and 2 share the best R-square 0.91 with its maximum equal 1, and model 1 is selected as the final battery degradation model since fewer fitting variables and shown as the following Fig. 6.19.

In Fig. 6.19, the black points are the original dataset points, and the fitting surface has shown clear dependence of DoD and MSOC on battery degradation, i.e., higher MSOC and larger DoD will cause higher battery degradation. With the above battery degradation model, the lifetime of battery can be shown as (6.2).

$$L_i^T = \frac{1 - 0.8}{De_i^b} = \frac{0.2}{De_i^b} \tag{6.2}$$

where $1 - 0.8$ means the battery lifetime terminates when the normalized battery capacity becomes 0.8 of its full capacity; L_i^T is the battery lifetime under charging/discharging event i. Obviously, if we want to extend the battery lifetime L_T, De_i^b should be minimized.

(4) Multi-battery scheduling

For indicating when and how many batteries should be utilized, a task matrix B^A is defined and Eq. (6.3) gives an example with the entire operating period having 4 time-intervals, i.e., $t_1 \sim t_4$, and the shipboard ESS include 4 batteries, i.e., no. 1–4.

$$B^A = \begin{bmatrix} 1 & 1 & 0 & 0 \\ 1 & 1 & 0 & 0 \\ 0 & 1 & 1 & 1 \\ 0 & 1 & 1 & 1 \end{bmatrix} \tag{6.3}$$

In (6.3), the row represents batteries and the column represents time-intervals. $B^A(i, j) = B^A_{i,j} = 1$ represents battery i will be switched-on to share power demand (charging or discharging) in the j-th time-interval, or $B^A(i, j) = B^A_{i,j} = 0$ represents the battery i will stand by. With the above definition, the process of multi-battery management can be shown in Fig. 6.20.

With the above multi-battery ESS management, different batteries or battery groups can share different charging/discharging events, which has the potential to reduce the cycles of each battery. The overall lifetime of multi-battery ESS maybe therefore extended.

(5) Case study

To show the benefits of the proposed model, three methods are compared with each other.

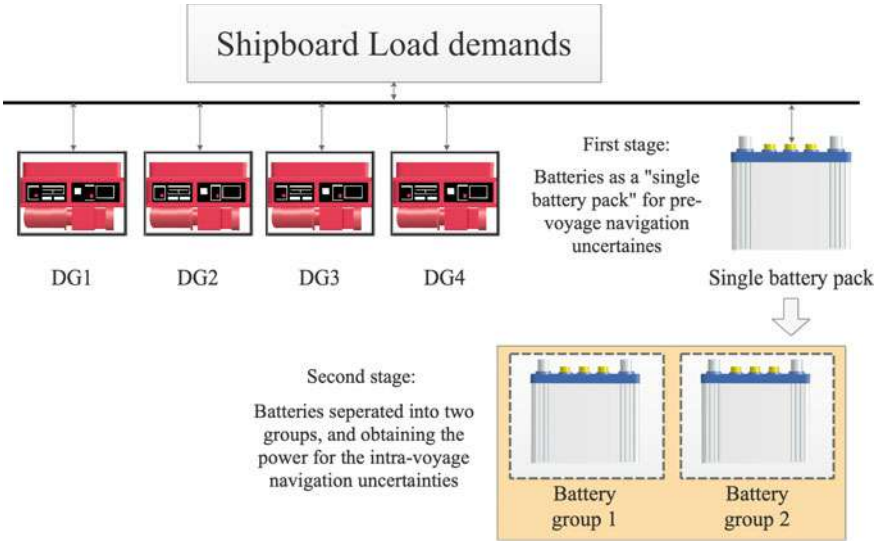

Fig. 6.20 Multi-battery management into two-stage operation. Reprinted from [38], with permission from IEEE

Method A: Conventional energy management without considering battery lifetime degradation [2].

Method B: Conventional energy management only considering DoD as the battery lifetime determinant [34].

Method C: Proposed energy management without multi-battery management.

It should be noted that methods A–C are used to calculate the battery power, and the battery degradations of three methods are calculated by the same model proposed (Model 1 in Table 6.3). The power and SOC curves of three methods are shown in Fig. 6.21, and the corresponding battery degradation in each voyage and overall lifetime are shown in Table 6.4.

In this case study, the voyage is divided into two parts, i.e., $t = 0 \sim 35$ and $t = 41 \sim 64$ are in cruising states, and $t = 36 \sim 40$ is in berthed-in state. From the results in Fig. 6.21, batteries in method A–C all tend to discharge when cruising states to share the power demand and to charge when berthed-in state. It is mainly because when berthed-in, the propulsion load is zero and to avoid frequent start-ups/shut-downs of onboard generators, the energy will be stored in the battery for later usage.

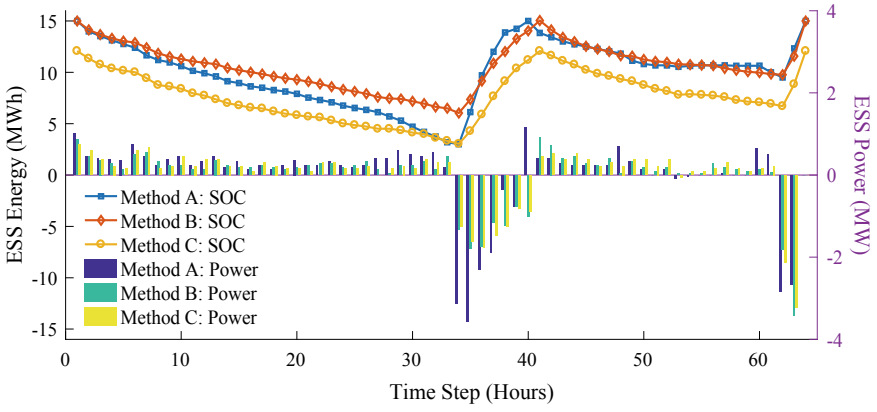

Fig. 6.21 Battery power schedules and SOCs of three cases. Reprinted from [38], with permission from IEEE

Table 6.4 Battery degradation and lifetime in three methods, reprinted from [38], with permission from IEEE

Method	Battery degradation ($\times 10^{-5}$)	Battery lifetime (Times)	Lifetime extension ratios (%)
A	34.94	572.4	–
B	25.76	776.4	35.6%
C	23.0	869.5	51.9%

However, with different battery degradation model, method A–C have different DoDs and MSOCs. In method A, the battery degradation is not considered, the battery operating scheme tends to fully use the battery to reduce $FC^{DG} + FC^{ST}$, and the DoDs of $t = 0$–35, $t = 36$–40 and $t = 41$–64 are 0.8, 0.79, and 0.27, respectively. Meanwhile, in method B, the DoD is considered as the only decision variable of battery degradation. Then the battery operating scheme tends to limit the DoDs, in which the DoDs of $t = 0$–35, $t = 36$–40, $t = 41$–64 decrease to 0.6, 0.6, and 0.27. As a result, the battery lifetime of method B increases by 35.6% compared with method A from Table 6.4. This phenomenon clearly shows that DoD is an important factor for battery lifetime.

In the proposed model (method C), the DoD and MSOC are considered as two factors for battery lifetime. Then compared with method B, method C reduces the MSOC of $t = 0 \sim 35$,$t = 36 \sim 40$, and $t = 41 \sim 64$ from 0.8, 0.8, and 0.87 (method B) to 0.49, 0.5, and 0.66 (method C). Correspondingly, the battery lifetime of method C increases by 51.9% compared with method A, and 12% longer than method B.

The above phenomenon clearly shows that both the DoD and MSOC have vital impacts on the battery lifetime. The proposed test case has 4 batteries, and each battery has 4 MWh capacity and 2.5 MW power, which is denoted as 1–4. 4 batteries are in two groups. Battery 1, 2 are group 1, and battery 3, 4 are group 2. Method D is designed to show the advantages of multi-battery management. The battery power of methods C and D are shown in Fig. 6.22.

Method D: Proposed energy management with multi-battery management.

From Fig. 6.22, with the multi-battery management, the power demand in different time periods is shared by battery $1 + 2$ and $3 + 4$, respectively. For example, when $t = 0 \sim 13$, the power demand is undertaken by battery $1 + 2$, and when $t = 14 \sim 36$, battery $3 + 4$ undertake the power demand. With this strategy, the battery degradations are shown in Table 6.5.

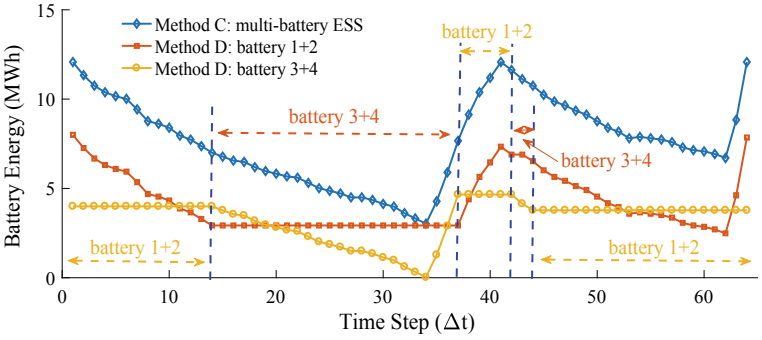

Fig. 6.22 Battery power schedules and SOCs of method C and D. Reprinted from [38], with permission from IEEE

Table 6.5 Battery degradation and lifetime in method C and D, reprinted from [38], with permission from IEEE

Method		Battery degradation ($\times 10^{-5}$/MWh)	Actual battery degradation (MWh)	Battery lifetime (times)
C	1 + 2	11.5	1.84×10^{-3}	869.5
	3 + 4	11.5	1.84×10^{-3}	
	total	23.0	3.68×10^{-3}	
D	1 + 2	27.4	2.19×10^{-3}	980.3
	3 + 4	13.4	1.07×10^{-3}	
	total	20.4	3.26×10^{-3}	

From the above results, the implementation of multi-battery management can further reduce the MSOC of battery 3 + 4, which leads the battery 3 + 4 only have 1.07×10^{-3} MWh degradation compared with 1.84×10^{-3} in method C. As a result, battery 1 + 2 must undertake more power demand than battery 3 + 4, so their degradations increase to 2.19×10^{-3}. In total, the battery degradation in method D is still lower than method C.

In the next voyage, battery 1 + 2 and battery 3 + 4 will change their roles. Battery 1 + 2 will lower their MSOC and battery 3 + 4 will undertake more power to protect the health of battery 1 + 2. With this strategy, the multi-battery management can further extend the total battery lifetime by 12.7%, and the lifetime increases from 869.5 cycles to 980.3 cycles.

As above, the proposed shipboard multi-battery management method can be viewed as a coordinated operation of all the onboard batteries. One battery group undertakes most of the power demand and make the other one working in an MSOC with lower degradation. Then in the next voyage, the battery groups change their roles for the iterative usages.

References

1. Zhao, H., Wu, Q., Hu, S., et al.: Review of energy storage system for wind power integration support. Appl. Energy **137**, 545–553 (2015)
2. Kanellos, F.D.: Optimal power management with GHG emissions limitation in all-electric ship power systems comprising energy storage systems. IEEE Trans. Power Syst. **29**(1), 330–339 (2013)
3. Kanellos, F.D., Tsekouras, G.J., Hatziargyriou, N.D.: Optimal demand-side management and power generation scheduling in an all-electric ship. IEEE Trans. Sustain. Energy **5**(4), 1166–1175 (2014)
4. Fang, S., Xu, Y., Li, Z., et al.: Optimal sizing of shipboard carbon capture system for maritime greenhouse emission control. IEEE Trans. Ind. Appl. **55**(6), 5543–5553 (2019)
5. Hou, J., Sun, J., Hofmann, H.: Mitigating power fluctuations in electric ship propulsion with hybrid energy storage system: design and analysis. IEEE J. Oceanic Eng. **43**(1), 93–107 (2017)

6. Hou, J., Sun, J., Hofmann, H.: Control development and performance evaluation for battery/flywheel hybrid energy storage solutions to mitigate load fluctuations in all-electric ship propulsion systems. Appl. Energy **212**, 919–930 (2018)
7. Hou, J., Song, Z., Park, H., et al.: Implementation and evaluation of real-time model predictive control for load fluctuations mitigation in all-electric ship propulsion systems. Appl. Energy **230**, 62–77 (2018)
8. Kanellos, F.D.: Real-time control based on multi-agent systems for the operation of large ports as prosumer microgrids. IEEE Access **5**, 9439–9452 (2017)
9. Kanellos, F.D., Volanis, E.S., Hatziargyriou, N.D.: Power management method for large ports with multi-agent systems. IEEE Trans. Smart Grid **10**(2), 1259–1268 (2017)
10. Gennitsaris, S.G., Kanellos, F.D.: Emission-aware and cost-effective distributed demand response system for extensively electrified large ports. IEEE Trans. Power Syst. **34**(6), 4341–4351 (2019)
11. Molavi, A., Shi, J., Wu, Y., et al.: Enabling smart ports through the integration of microgrids: a two-stage stochastic programming approach. Appl. Energy **258**, 114022 (2020)
12. Zhao, N., Schofield, N., Niu, W.: Energy storage system for a port crane hybrid power-train. IEEE Trans. Transp. Electrif. **2**(4), 480–492 (2016)
13. Binti Ahamad, N., Su, C., Zhaoxia, X. et al.: Energy harvesting from harbor cranes with flywheel energy storage systems. IEEE Trans. Industry Appl. **55**(4), 3354–3364
14. Díaz-González, F., Sumper, A., Gomis-Bellmunt, O., et al.: A review of energy storage technologies for wind power applications. Renew. Sustain. Energy Rev. **16**(4), 2154–2171 (2012)
15. Mutarraf, M., Terriche, Y., Niazi, K., et al.: Energy storage systems for shipboard microgrids-a review. Energies **11**(12), 3492 (2018)
16. Park, J., Kalev, C., Hofmann, H.: Control of high-speed solid-rotor synchronous reluctance motor/generator for flywheel-based uninterruptible power supplies. IEEE Trans. Industr. Electron. **55**, 3038–3046 (2008)
17. Cheng, M., Sami, S., Wu, J.: Benefits of using virtual energy storage system for power system frequency response. Appl. Energy **194**, 376–385 (2017)
18. Díaz-González, F., Sumper, A., Gomis-Bellmunt, O., et al.: Energy management of flywheel-based energy storage device for wind power smoothing. Appl. Energy **110**, 207–219 (2013)
19. Spiryagin, M., Wolfs, P., Szanto, F., et al.: Application of flywheel energy storage for heavy haul locomotives. Appl. Energy **157**, 607–618 (2015)
20. Norway electric ferry cuts emissions by 95%, costs by 80%. https://reneweconomy.com.au/norway-electric-ferry-cuts-emissions-95-costs-80-65811/
21. A new all-electric cargo ship with a massive 2.4 MWh battery pack launches in China. https://electrek.co/2017/12/04/all-electric-cargo-ship-battery-china/
22. Deep Ocean-01 official ship launched in Shenzhen. http://www.sz.gov.cn/cn/xxgk/zfxxgj/tpxw/content/post_8012934.html
23. 5 MW energy storage for cold-ironing in Lianyugang port. https://www.energytrend.cn/news/20200116-81127.html
24. Jiang, Q., Gong, Y., Wang, H.: A battery energy storage system dual-layer control strategy for mitigating wind farm fluctuations. IEEE Trans. Power Syst. **28**(3), 3263–3273 (2013)
25. Fang, S., Xu, Y., Li, Z., et al.: Two-step multi-objective management of hybrid energy storage system in all-electric ship microgrids. IEEE Trans. Veh. Technol. **68**(4), 3361–3373 (2019)
26. Alafnan, H., Zhang, M., Yuan, W., et al.: Stability improvement of DC power systems in an all-electric ship using hybrid SMES/battery. IEEE Trans. Appl. Supercond. **28**(3), 1–6 (2018)
27. Yao, J., Li, H., Liao, Y., et al.: An improved control strategy of limiting the DC-link voltage fluctuation for a doubly fed induction wind generator. IEEE Trans. Power Electron. **23**(3), 1205–1213 (2008)
28. Li, X., Hui, D., Lai, X.: Battery energy storage station (BESS)-based smoothing control of photovoltaic (PV) and wind power generation fluctuations. IEEE Transactions on Sustainable Energy **4**(2), 464–473 (2013)

29. Tran, T.K.: Study of electrical usage and demand at the container terminal. Deakin University (2012)
30. Perera, L., Soares, C.: Weather routing and safe ship handling in the future of shipping. Ocean Eng. **130**, 684–695 (2017)
31. Krata, P., Szlapczynska, J.: Ship weather routing optimization with dynamic constraints based on reliable synchronous roll prediction. Ocean Eng. **150**, 124–137 (2018)
32. Grifoll, M., Martorell, L., de Osés, F.: Ship weather routing using pathfinding algorithms: the case of Barcelona-Palma de Mallorca. Trans. Res. Procedia **33**, 299–306 (2018)
33. Fang, S., Xu, Y., Wang, H. et al.: Robust operation of shipboard Microgrids with multiple-battery energy storage system under navigation uncertainties. IEEE Trans. Vehic. Technol., In Press (2020)
34. Ju, C., Wang, P., Goel, L., et al.: A two-layer energy management system for microgrids with hybrid energy storage considering degradation costs. IEEE Trans. Smart Grid **9**(6), 6047–6057 (2017)
35. Zhou, C., Qian, K., Allan, M., et al.: Modeling of the cost of EV battery wear due to V2G application in power systems. IEEE Trans. Energy Convers. **26**(4), 1041–1050 (2011)
36. Farzin, H., Fotuhi-Firuzabad, M., Moeini-Aghtaie, M.: A practical scheme to involve degradation cost of lithium-ion batteries in vehicle-to-grid applications. IEEE Trans. Sustain. Energy **7**(4), 1730–1738 (2016)
37. Liu, K., Li, Y., Hu, X., et al.: Gaussian process regression with automatic relevance determination kernel for calendar aging prediction of lithium-ion batteries. IEEE Trans. Industr. Inf. **16**(6), 3767–3777 (2019)
38. Fang, S., Gou, B., Wang, Y., et al.: Optimal hierarchical management of shipboard multi-battery energy storage system using a data-driven degradation model. IEEE Transactions on Transportation Electrification **5**(4), 1306–1318 (2019)
39. Advanced Life Cycle Engineering (CALCE) at the University of Maryland. https://web.calce.umd.edu/batteries/data.htm

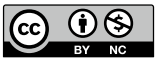

Chapter 7
Multi-energy Management of Maritime Grids

7.1 Concept of Multi-energy Management

7.1.1 Motivation and Background

Generally, all the energy systems are "multi-energy systems" in the sense that multiple energy sectors interact at different levels. For example in conventional power systems, the coal or gas used for generating electricity should be transported to each power plant, and this process implies the couplings between fossil energy and electrical energy. Another case is, the heating service by the combined heat-power plant also last for decades, and this process includes the coupling between heating energy and electrical energy. However, those energy couplings between different systems are conventionally weak compared with the relationship within a single energy system, and that is the main reason for the past studies of power system mostly only consider the electrical energy [1–3]. However, the interactions between different energy systems become tighter and more frequent recently, and this trend is about to continue in the future [4–7], such as the electric-gas energy system, and the coordinated heat-power system, or even the transportation-power system motivated by the transportation electrification. In this sense, conventional energy management for a single energy system may not be valid in the future, which drives the research of multi-energy management.

In literature, [8–11] focus on the coordination between the gas system and power systems [12–15]. Study the energy management methods for heat-power systems [16, 17]. Study the water-power systems and [18–22] investigate the coupling between the transportation system and power system by electric vehicles' charging and discharging. The above research has brought a new perspective in energy system analysis, particularly in the light of reducing the economic and environmental burden of energy services. In summary, three benefits can be achieved by multi-energy management:

S. Fang and H. Wang, *Optimization-Based Energy Management for Multi-energy Maritime Grids*, Springer Series on Naval Architecture, Marine Engineering, Shipbuilding and Shipping 11, https://doi.org/10.1007/978-981-33-6734-0_7

a. Increasing or improving the energy efficiency of the entire system and the utilization of primary energy sources. The reason is the multi-energy system can use the energy at different levels. For example, the waste heat after generating electricity can be used for heating services and the energy efficiency of the entire system improves.
b. Better deploying various energy resources at multiple system levels. For example, small-scale gas turbines can respond to volatile electricity market prices in a wind-rich energy system.
c. Increasing the energy system flexibility by the coordinations between different energy systems. For example, scheduled charging/discharging of the electric vehicles acts as demand response tool for power system. Or the thermal storage tank can bring flexibility for combined power-heat plants.

Since the above three main advantages, the research on multi-energy management is essential for future energy systems. However, different energy systems have different administrators and quite distinct characteristics, and their coordinations are much more complex compared with the coordinations within a single energy system. Proper modeling methods and control strategies should be proposed to facilitate their operation.

7.1.2 Classification of Multi-energy Systems

The multi-energy systems can be classified by different perspectives, and there are mainly four perspectives to characterize the MES. The first is the spatial perspective. This perspective points out how MES can intend at different levels of aggregation in terms of components or even just conceptually. These levels go from buildings to district and finally to regions and even countries. This classification is shown in Fig. 7.1a.

The second perspective focuses on the provision of multiple services by optimally scheduling different energy systems, particularly at the supply levels. Such as the services provided by the MES, including electricity supply, water supply, heating service, EV charging services, gas filling services, and so on. This classification is shown in Fig. 7.1b.

The third perspective highlights how different types of fuels can be integrated together for providing optimal energy services, typically for economic or environmental targets. The fuel types range from classical fossil fuel, such as oil, coal and natural gas, to biomass fuels, and renewable energy. This classification is shown in Fig. 7.1c.

The fourth perspective discusses the coordinations between different energy systems, especially the coordination between different networks, such as the electrical network, gas network, district heating/cooling network, in terms of facilitating the development of multi-energy management methods and their interactions. This classification is shown in Fig. 7.1d.

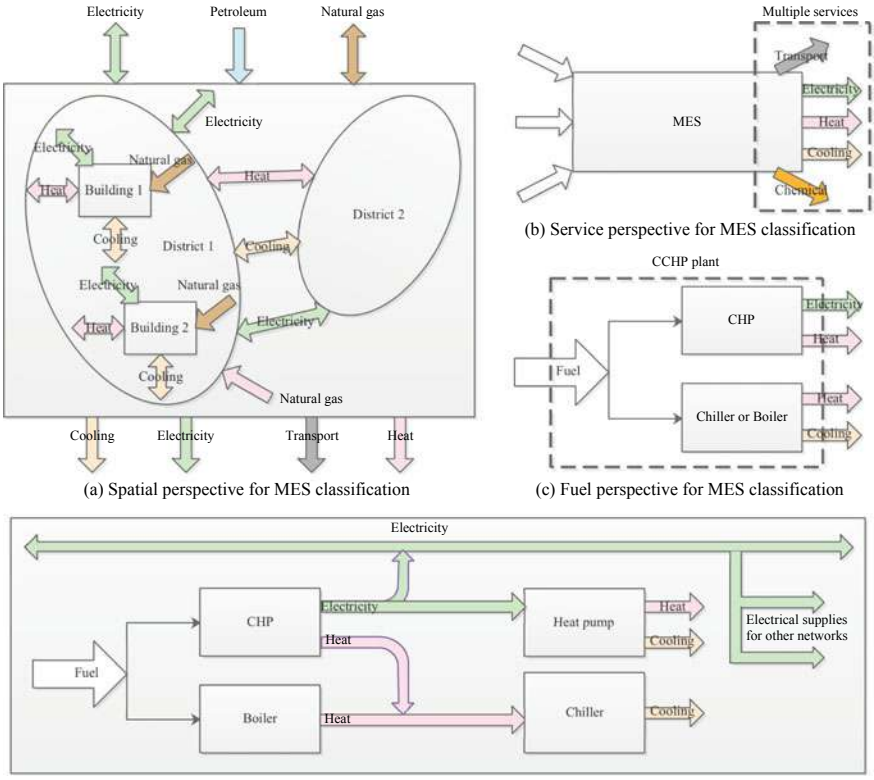

(a) Spatial perspective for MES classification

(b) Service perspective for MES classification

(c) Fuel perspective for MES classification

(d) Network perspective for MES classification

Fig. 7.1 Classifications for MES [4]

Figure 7.1a classifies the MESs from the spatial perspective. An individual building exchanges energy by the transmission of electricity, heat, cooling, and natural gas. Then multiple buildings aggregate as a district, then multiple districts aggregate as a region and expand to a wider area. In this perspective, MESs can be classified as the building MES, district MES, region MES, and so on.

Figure 7.1b classifies the MESs from the service perspective. Generally, MES can provide multiple services to the customers, such as the electricity supply, heat and cooling power, and even some transport services, such as the charging/discharging of EV. In this perspective, MESs can be classified as combined electric-heat MES, combined electric-heat-cooling MES, and even electric-heat-water supply MES, since the water pump is coupled with the electric network by the electrical water pumps.

Figure 7.1c classifies the MES from the fuel perspective. For example, there exist many power sources in MES, such as power plants, boilers, gas turbines, and chillers. They may consume different types of fuels. Different power plants may consume coal, oil, or gas. A boiler may consume electricity or other fossil fuel, and

a chiller may consume electricity or heat power. In this sense, the fuel type can also classify the MESs, such as the coal-gas MES, gas-hydrogen MES, or even ammonia MES since ammonia is a new type of carbon-free fuel [23].

Figure 7.1d classifies the MES from the network perspective since every "energy carrier" should be transmitted by a designed network. The electrical network includes power systems on multiple scales. Gas and oil are transported by pipelines or transportation flows. Heat and cooling power also have certain pipelines. Those different networks can have different topologies and operating strategies, which is the main motivation of this classification method. In this sense, the networks of MESs can be classified as combined electric-heat networks, combined electric-heat-cooling networks, and so on.

7.2 Future Multi-energy Maritime Grids

7.2.1 Multi-energy Nature of Maritime Grids

A sketch of MES is given in the former section to show the basic advantages and characteristics. In this section, the multi-energy nature of maritime grids will be analyzed to show their similarities and differences compared with conventional MESs, and Fig. 4.1 is re-drawn below as Fig. 7.2 as an illustration of future maritime grids. Two cases of maritime grids will be given after this illustration.

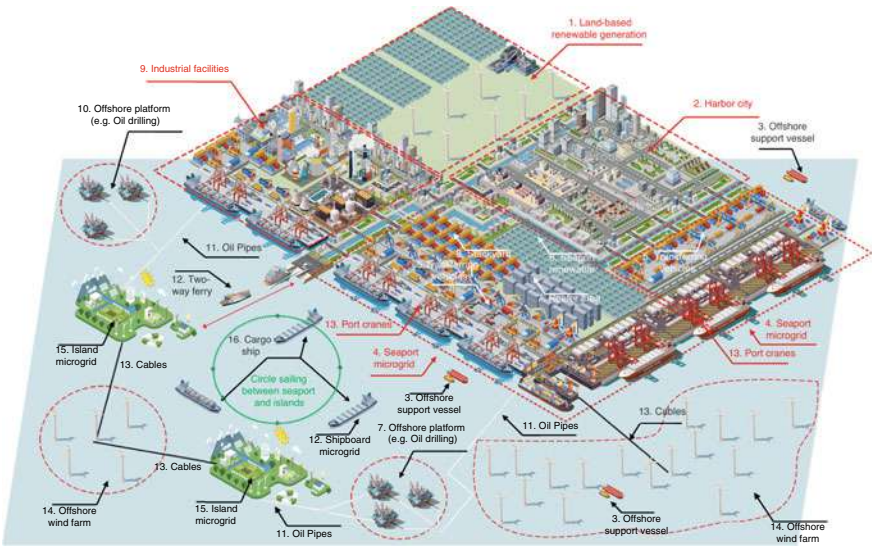

Fig. 7.2 Illustrations of future maritime grids

(1) Spatial perspective

From Fig. 7.2, maritime grids cover different spatial areas. For example, island microgrids cover an individual island, and the energy sources include offshore wind power, photovoltaic power, and underground cables. Seaport microgrids cover the harbor territory, and the energy sources include the offshore wind farm, land-based photovoltaic farm, oil pipelines, and the electricity supply from the harbor city. Other maritime grids include the drilling platforms and different types of ships. In summary, maritime grids have a very wide range on system scales, from the smallest to a ferry or a building and the biggest to a harbor city, which involves all the energy sources within a conventional MES. Different maritime grids are coupled tightly by energy connections, and current multi-microgrid coordination methods can be used in maritime grids to achieve better system characteristics.

(2) Service perspective

Figure 7.2 shows maritime grids can provide different services to customers, including the conventional services of electricity, heat, cooling in land-based MES, also including some types beyond current focuses, such as the logistic services, fuel transportation services. This is the primary difference between current studied MES (land-based MES) from the maritime grids. This is also a challenge for the research of maritime grids, since new energy models of those services should be formulated and integrated into the energy management model.

(3) Fuel perspective

Maritime grids also involve different types of fuels. In Fig. 7.2, the drilling platform can harvest crude oil or natural gas, and transport them to an island or the seaport. The industrial factory can refine crude oil into different types of fuels, such as gasoline, diesel, and so on. Those fuels may in reverse fill into the ships for sailing, into seaport for generation, and into the harbor city for daily lives. Besides, some novel fuels may also use in maritime grids, such as ammonia, methanol, and ethanol.

(4) Network perspective

Maritime grids also have different types of networks. Figure 7.2 shows some typical ones, (1) electrical networks in harbor city, seaport, industrial factory; (2) heat/cooling networks in harbor city, seaport, industrial factory; (3) fossil fuel networks between the ocean platforms and a seaport or an island; (4) electrical networks between offshore wind farms and a seaport or an island; (5) multi-energy network within an island; (6) transportation network by ships and vehicles. Those networks above are connected with multiple energy and information flows and may be more complex than conventional land-based MESs.

7.2.2 *Multi-energy Cruise Ships*

In Fig. 7.3, a typical topology of a multi-energy cruise ship is shown. Detailed illustrations can be depicted as follow. The load demands can be classified into three categories, the electric load, thermal load, and propulsion load. Among the three load demands, the propulsion load is to drive the cruise ship, which consists most of, usually more than 50% of the total load demand [24]. The propulsion load has a simple cubic relationship with the cruising speed, which is under the constraints of navigation distance [25]. The electric load in cruise ships includes the illumination, recreation equipment, movie theater, and so on. This type of load scales up to tens of megawatt [24], which is provided by the electric power bus, shown as the blue lines and arrows in Fig. 7.3. The thermal load in cruise ship includes the cooling and heat load, the swimming pool, and the cooking. This type of load also scales up to tens of megawatt [27], which is provided by the thermal power network, shown as the green line and arrows in Fig. 7.3. It also should be noted that in some cruise ships the cooling and heat loads are provided by the electricity. In this work, we will compare the introduced multi-energy technology with the single electric supply mode.

As for the generation systems, to provide adequate electric and thermal loads for the overall cruise ship. There exist three types of generation systems, i.e., DG, CCHP, and PTC. The DGs make up the main part of the shipboard generation, which provides most of the electric power supply. The CCHP both provides the electric power and the thermal power and the PTC uses electricity to produce thermal power. To balance both the electric and thermal loads, the HES (electric and thermal energy storage) is integrated.

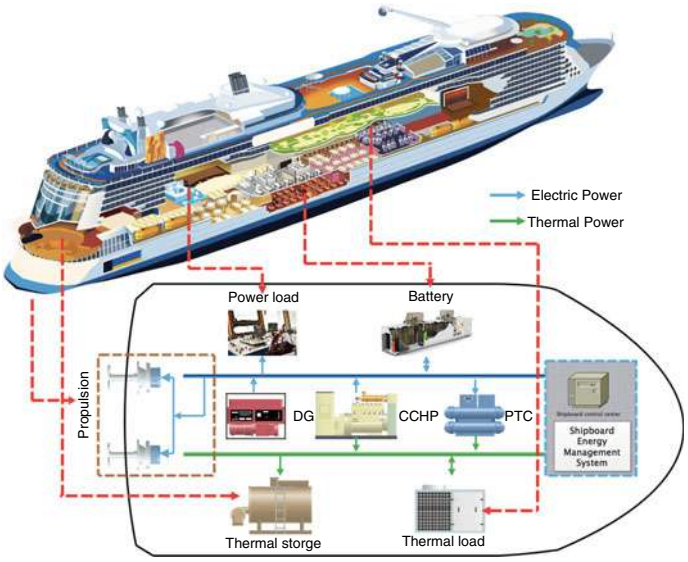

Fig. 7.3 Topology of a multi-energy cruise ship

7.2.3 *Multi-energy Seaport*

We have illustrated the multi-energy seaport in Chap. 1. Here we re-draw Fig. 1.17 as Fig. 7.4to further show its multiple energy flows.

Generally, the seaport is connected with the main grid and various renewable energy are integrated, i.e., seaport wind farms and PV farms in Fig. 7.4. All the port-side equipment, including the quay cranes, gantry cranes, transferring trunks, are electrically-driven. The seaport provides four types of services to the berthed-in ships and has four sub-systems for each type of services: (1) logistic service. The berth allocation and quay crane scheduling for loading/unloading cargo; (2) fuel transportation. Unloading or refilling fuel for the berthed-in ships; (3) cold-ironing. Providing electricity to the berthed-in ships and (4) refrigeration reefer for the cold-chain supply. The coordination between different sub-systems is shown in Fig. 7.5. Four sub-systems are communicating by the seaport control center and a distributed control strategy is employed in the seaport microgrid.

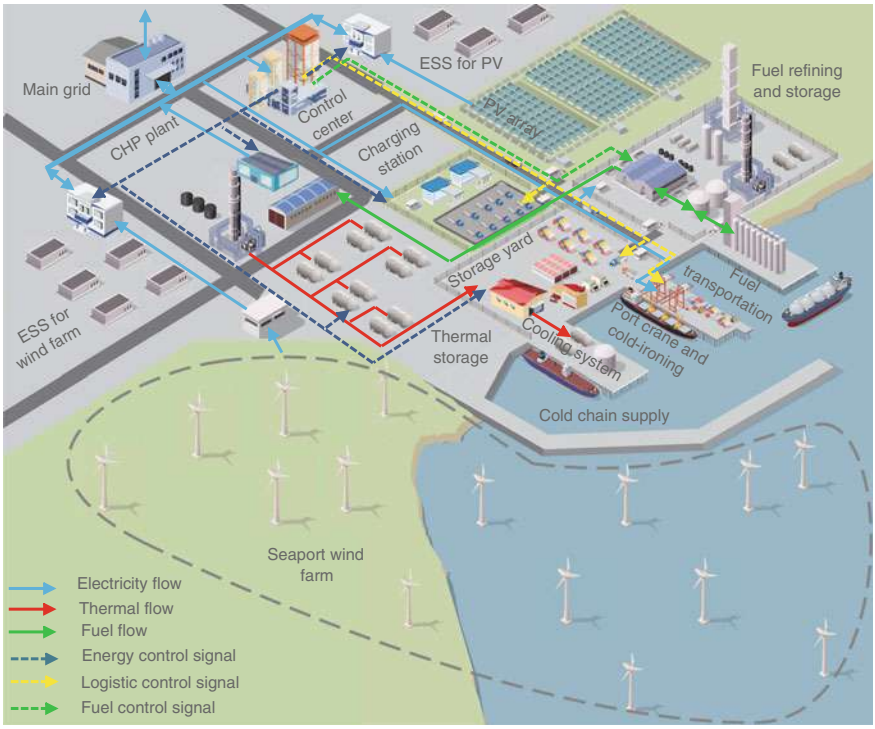

Fig. 7.4 Multi-energy seaport microgrid

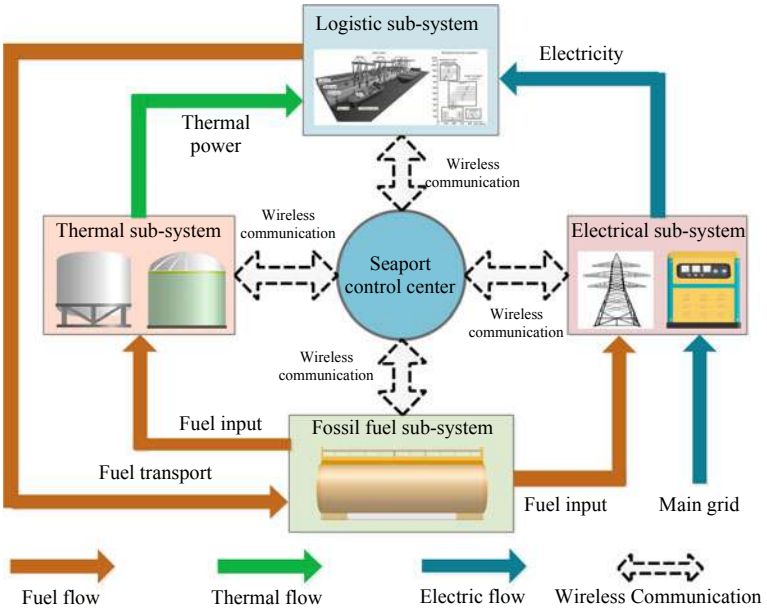

Fig. 7.5 Coordination between different sub-systems in seaport microgrid

7.3 General Model and Solving Method

7.3.1 Compact Form Model

From above, maritime grids involve different networks and provide multiple types of services by different types of fuels. In this sense, maritime grids have a significant characteristic, i.e., using the electric network as the backbone for energy management, and other different networks serve as the "load demand" of electric networks. For example, the heat/cooling networks couple with the electric network by CHP or electric boiler/chiller, and water supply network couple with the electric network by electric water pumps, and logistic network couple with the electric network by charging/discharging.

For this complex network, a general energy scheduling form can be shown as (7.1). Where $f(x)$ is the objective function of the main network, generally the electric network, and x is the decision variable vector; $g_i(y_i)$ is the objective function of the i-th network, and y_i is the decision variable vector of the i-th network; $F(x)$ is the constraint set of the main network; $G_i(y_i)$ is the constraint set of the i-th network; $A_i \cdot x = H_i(y_i)$ is the coupling constraint set of power consumption of coupling equipment, such as water pump, CHP, and various logistic equipment.

$$\begin{aligned} &\min_{x,y_i} f(x) + \sum_{i=1}^{n} g_i(y_i) \\ &s.t. F(x) \geq 0, G_i(y_i) \geq 0 \\ &A_i \cdot x = H_i(y_i), x \in X, y_i \in Y_i \end{aligned} \tag{7.1}$$

7.3.2 A Decomposed Solving Method

This Chapter proposes a decomposed method to solve this type of problem, which is given by the following Theorem 7.1.

Theorem 1 *The above formulation is equivalent to the following form.*

$$\begin{aligned} \min_{x} \Bigg[f(x) + \sum_{i=1}^{n} \underset{y_i,\tau_i,u_i}{inf} \left(g_i(y_i) + \tau_i \cdot G_i(y_i) + u_i \cdot [H_i(y_i) - A_i \cdot x]\right) \Bigg] \\ s.t. F(x) \geq 0, G_i(y_i) \geq 0 \\ x \in X \cap V \\ V \equiv \bigcup_{i=1}^{n} \{x | \lambda_i \cdot [H_i(y_i) - A_i \cdot x] = 0\} \\ , where \lambda_i \geq 0 and \sum_{i=1}^{n} \lambda_i = 1 \end{aligned} \tag{7.2}$$

where u_i is the optimal multiplier vector of the following optimization problem.

$$\begin{aligned} &\min_{y_i} \sum_{i=1}^{n} g_i(y_i) \\ &s.t. G_i(y_i) \geq 0, A_i \cdot x = H_i(y_i), for\ all\ i \end{aligned} \tag{7.3}$$

Proof

(1) Problem (7.1) and (7.2) have the same feasible region.

(1.1) If $\bar{x}$ be feasible for (7.1), then $\bar{x}$ is feasible for (7.2).

Let $\bar{x}$ be an arbitrary point in the feasible region of (7.1), then

$$F(\bar{x}) \geq 0, A_i \cdot \bar{x} = H_i(y_i), for \forall i \tag{7.4}$$

It follows that (7.5) holds for all λ_i.

$$\lambda_i \cdot [H_i(y_i) - A_i \cdot \bar{x}] = 0 \tag{7.5}$$

Then $\bar{x} \in V$, and $F(\bar{x}) \geq 0$. $\bar{x}$ is also feasible for (7.2).

(1.2) If $\bar{x}$ be feasible for (7.2), then $\bar{x}$ is feasible for (7.1).

Let $\bar{x}$ be an arbitrary point for (7.2), then (7.5) holds at least for one i. $F(\bar{x}) \geq 0$ is satisfied all the same, then (7.6) holds.

$$\eta \cdot F(\bar{x}) + \lambda_i \cdot [H_i(y_i) - A_i \cdot \bar{x}] \geq 0 \tag{7.6}$$

It follows that

$$\underset{\eta \geq 0}{\text{Inf}}\{\eta \cdot F(\bar{x}) + \lambda_i \cdot [H_i(y_i) - A_i \cdot \bar{x}] \geq 0\} \tag{7.7}$$

Since $\eta = 0$ is allowed in (7.7). Now, (7.7) is the dual of the following optimization problem.

$$\begin{gathered} \min_{y_i \in Y_i} 0^T \cdot y_i \\ s.t. F(x) \geq 0, H_i(y_i) = A_i \cdot \bar{x} \end{gathered} \tag{7.8}$$

Obviously, (7.8) is feasible and has the optimal value of 0, hence, $\bar{x}$ is feasible for (7.1).

(2) The objective function

Since u_i is the optimal multiplier vector of (7.3), then (7.9) holds.

$$\begin{gathered} \min_{y_i} \sum_{i=1}^{n} g_i(y_i) \\ = inf\left\{\sum_{i=1}^{n} g_i(y_i) + \sum_{i=1}^{n} \tau_i \cdot G_i(y_i) + \sum_{i=1}^{u} u_i \cdot [H_i(y_i) - A_i \cdot x]\right\} \end{gathered} \tag{7.9}$$

In this sense,

$$\begin{gathered} \min_{x, y_i}[f(x) + \sum_{i=1}^{n} g_i(y_i)] \\ \min_{x}\left[f(x) + \sum_{i=1}^{n} \underset{y_i, \tau_i, u_i}{inf} (g_i(y_i) + \tau_i \cdot G_i(y_i) + u_i \cdot [H_i(y_i) - A_i \cdot x])\right] \end{gathered} \tag{7.10}$$

From above, (7.1) and (7.2) are equivalent, then the solution process is given below.

Solution process: From (7.2), the original problem can be solved in a two-step process. It should be noted that, $g_i(y_i) + \tau_i \cdot G_i(y_i)$ is a constant when minimizing x, so it is eliminated for simplification.

Step 1: Given a feasible $\bar{x}$, solve (7.11) for y_i^* and u_i.

$$\begin{gathered} \min_{y_i} \sum_{i=1}^{n} g_i(y_i) \\ s.t. G_i(y_i) \geq 0, A_i \cdot \bar{x} = H_i(y_i), \ for\ all\ i \end{gathered} \tag{7.11}$$

It should be noted that, there are no coupling between different networks. So (7.11) can be solved in parallel.

Step 2: Solve (7.12) for x.

$$\begin{aligned} &\min_{x}\left[f(x) + \sum_{i=1}^{n}\left(u_i \cdot \left[H_i\left(y_i^*\right) - A_i \cdot x\right]\right)\right] \\ &s.t. F(x) \geq 0, A_i \cdot x = H_i\left(y_i^*\right), \ for\ all\ i \end{aligned} \tag{7.12}$$

Then check the convergence characteristic, if yes, terminates and if not, return to Step 1 and update $\bar{x}$. The algorithm convergence is given below.

Algorithm convergence It is proved that the proposed method has finite ε-convergence characteristic.

Theorem 2 *Assume X and V are both compact set, f, g, F, G_i and H_i are continuous. The set $UT(x)$ of the optimal multiplier vector for (7.3) is non-empty for all x in X and uniformly bounded. Then, for any given $\varepsilon > 0$, the proposed procedure terminates in a finite number of steps.*

Proof For simplification, we define (7.13).

$$L(x, \tau, u) = f(x) + \sum_{i=1}^{n}(g_i(y_i) + \tau \cdot G_i(y_i) + u \cdot [H_i(y_i) - A_i \cdot x]) \tag{7.13}$$

For any sequence $L(x^v, \tau^v, u^v), x^v$ of the optimal solution of (7.2). Firstly, the optimal multipliers sequence τ^v, u^v will converges to a point noted as $(\bar{\tau}, \bar{u})$, since the uniformly bounded assumption of $UT(x)$. Additionally, x^v will converge to a point denoted as $\bar{x}$ since the compactness of X.

At last, since $L(x^v, \tau^v, u^v)$ is a non-increasing sequence and bounded below, there exists at least one sub-sequence of $L(x^v, \tau^v, u^v), x^v$ which converges to a point, we noted it as $L(\bar{x}, \bar{\tau}, \bar{u}), \bar{x}$.

Since the weak duality, $(\bar{\tau}, \bar{u})$ is the optimal multiplier for $\bar{x}$ and (7.14) holds.

$$L(\bar{x}, \bar{\tau}, \bar{u}) = \operatorname*{Inf}_{y_i}\left(f(\bar{x}) + \sum_{i=1}^{n} g_i(y_i)\right) \tag{7.14}$$

Then, for any given $\varepsilon > 0$, there should be finite v to make (7.15) hold.

$$L(\bar{x}, \bar{\tau}, \bar{u}) \leq L\left(x^v, \tau^v, u^v\right) \leq \operatorname*{Inf}_{y_i}\left(f(\bar{x}) + \sum_{i=1}^{n} g_i(y_i)\right) + \varepsilon \tag{7.15}$$

Then the proposed method should converge in finite steps.

7.4 Typical Problems

7.4.1 Multi-energy Management for Cruise Ships

This section uses the cruise ship in Fig. 7.3 as the test case to show the effects of energy management. For a more economic and environmental operation of the cruise ship, the shipboard energy management system will optimally dispatch the outputs of the DG, CCHP, PTC, and HES to fulfill the propulsion, onboard electric, and thermal loads. However, in practice, those control variables are not on the same time-scale. During the navigation, the ship will constantly cruise and the speed cannot be regulated rapidly [25], and the onboard facilities for tourists also should keep working till night. This makes the propulsion and electric loads should be fulfilled in a long-term horizon (every hour in this work). Besides, the thermal load should be satisfied in a short-term horizon (20 min) to meet the real-time constraints of indoor temperature and hot water supply. To coordinately satisfy the above load demands in two time-scales, in this work we propose a two-stage operation framework for the cruise ship, which is shown as follow:

From the Fig. 7.6, the first stage hourly schedules the DGs, CCHP, and battery to fulfill the voyage distance constraints and hourly electric load demand. The thermal power produced by the CCHP is stored in the thermal energy storage. In the second stage, every 20 min, the PTC and thermal energy storage is dispatched to meet the thermal load demand. With the above operation framework, both the propulsion and electric loads can be met in a long-term time-scale, as well as the thermal load demand can be met in a short-term time-scale to improve the QoS.

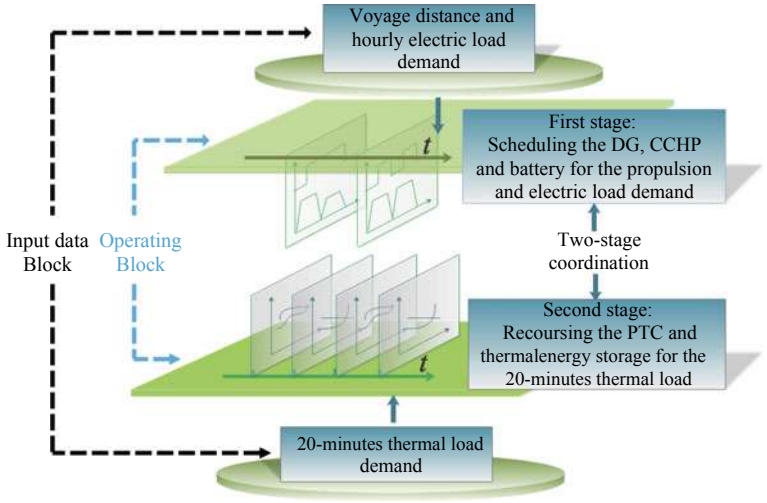

Fig. 7.6 Two-stage operation framework for the cruise ship, reprinted from [26], with permission from IEEE

To show the benefits of the proposed model, the onboard generation and battery SOC are shown in Fig. 7.7a, b, respectively. Figure 7.8 compares the results of the thermal load of the proposed two-stage method.

From Fig. 7.7a, the battery can coordinate with the speed adjustment to smooth the load profiles, which facilitates the economy of cruise ships (the DGs can better operate around their economic points). From Fig. 7.7b, the battery may have much deeper charging/discharging events without the speed adjustment. That is mainly because the cruising speed is fixed during the cruising time-intervals, and the battery should quickly respond to the load profiles for the economy of navigation.

From Fig. 7.8a, the proposed two-stage scheduling model can meet the thermal load demand in a more accurate time-scale by simply dispatching the loading factor

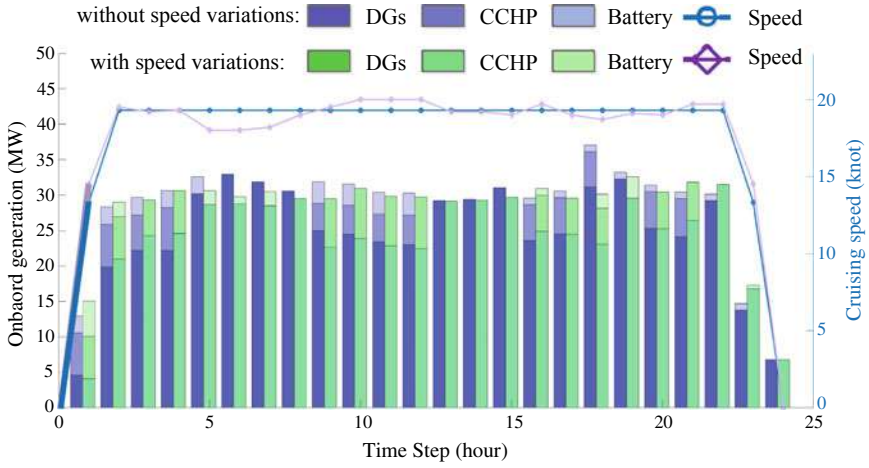

(a) Onboard generation with/without speed variations

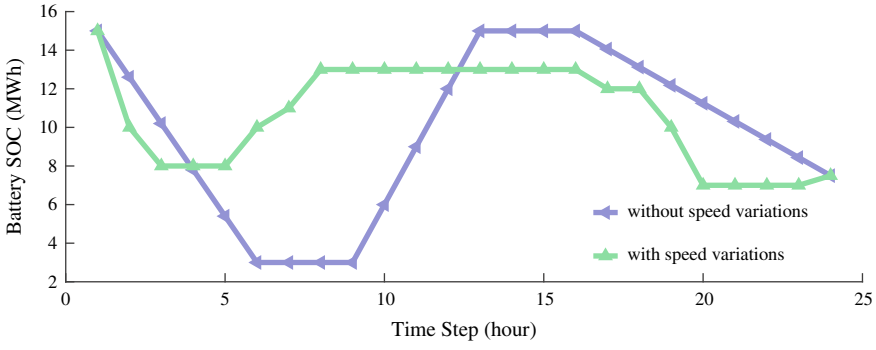

(b) Battery SOC with/without speed variations

Fig. 7.7 Onboard generation and battery SOC with/without speed variations, reprinted from [26], with permission from IEEE

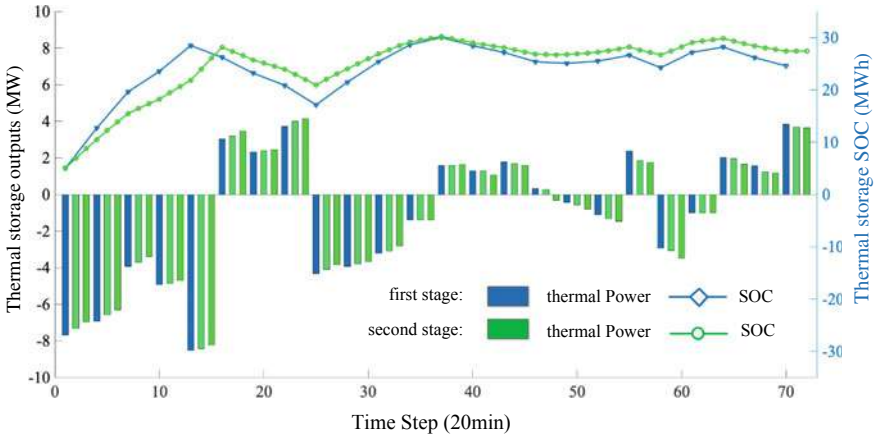

(a) thermal storage in the first/second stages

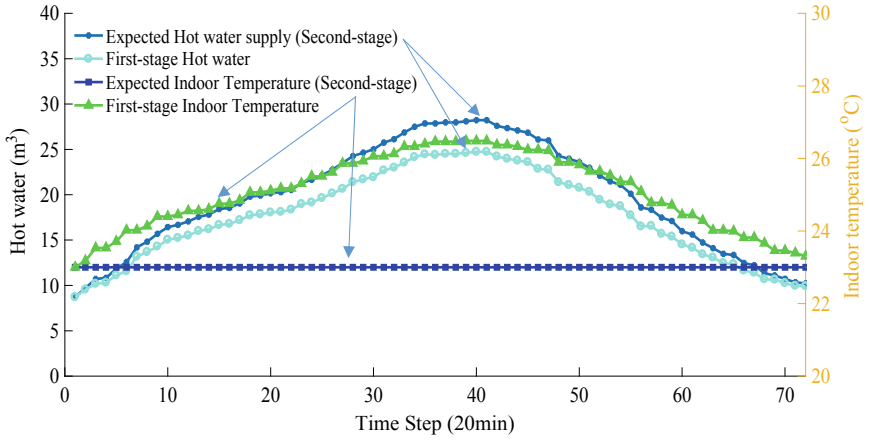

(b) indoor temperature and thermal load in the first/second stages

Fig. 7.8 Onboard thermal storage and thermal load, reprinted from [26], with permission from IEEE

of the thermal storage tank, and the outputs of PTC and CCHP. The results are shown in Fig. 7.8b. The indoor temperature can be kept as a constant meanwhile the single first stage will have a maximal 3 °C temperature variations since the accumulated effects of thermal load demand variations. Similarly, the single first stage also cannot meet the hot water supply-demand all the time, and the thermal variations will also be accumulated and make the supplies always smaller than the demands.

Current cruise ships are mainly BOS cruise ships, which means in the BOS mode, the thermal load demand is all provided by the electric-side (PTC units). In this case,

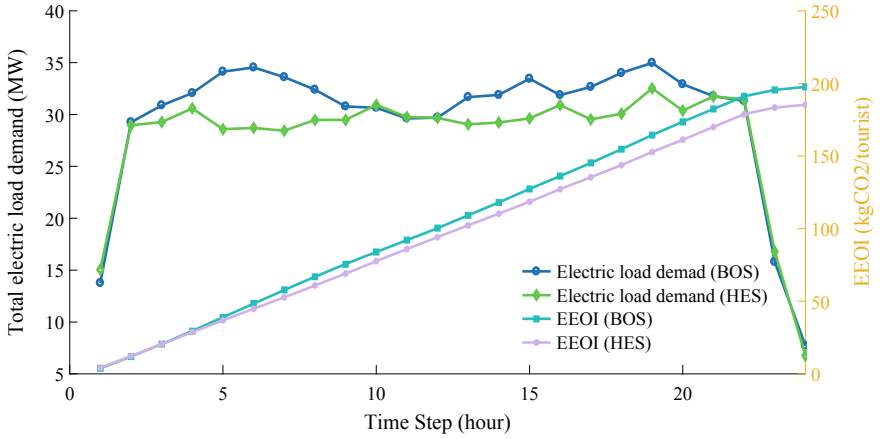

Fig. 7.9 Comparisons between BOS and HES cruise ships, reprinted from [26], with permission from IEEE

the BOS ship replaces the CCHP to conventional DG with the same capacity. The parameters are the same with DG2, 3. The total load demand and EEOI of BOS and HES ships are shown in Fig. 7.9.

From Fig. 7.9, the BOS cruise ship will have much larger load demands since the thermal load is provided by the PTC unit. Correspondingly, the EEOI of the HES integrated cruise ship is also much smaller than the BOS by 8.37%.

7.4.2 Multi-energy Management for Seaport Microgrids

(1) System description

From Fig. 7.10, there are three energy resources in this microgrid, i.e., photovoltaics(PVs), electrical substation, and gas pressure house. The PVs and substation inject electricity into the seaport microgrid via DC and AC buses, respectively. The gas pressure house injects gas into the seaport microgrid to the gas storage. Additionally, to improve the system flexibility, a battery energy storage system (ESS) and two thermal storages are incorporated. The AC/DC loads and heat/cooling power are supplied to the seaport loads, and DC power is used for charging the electric trunk. The power to gas equipment transforms the excess power to gas to fill the gas vehicles.

In this paper, the scheduling horizon is divided into equal time step Δt, denoted by set $\mathcal{T} = \{1, 2, \ldots, T\}$. The proposed operation method is formulated as a two-stage framework, where the first stage is for the day-ahead time-scale, and the second stage is for real-time scheduling, i.e., hourly. In the day-ahead operation (first stage), the hourly energy scheme is provided considering the uncertainties, and then in

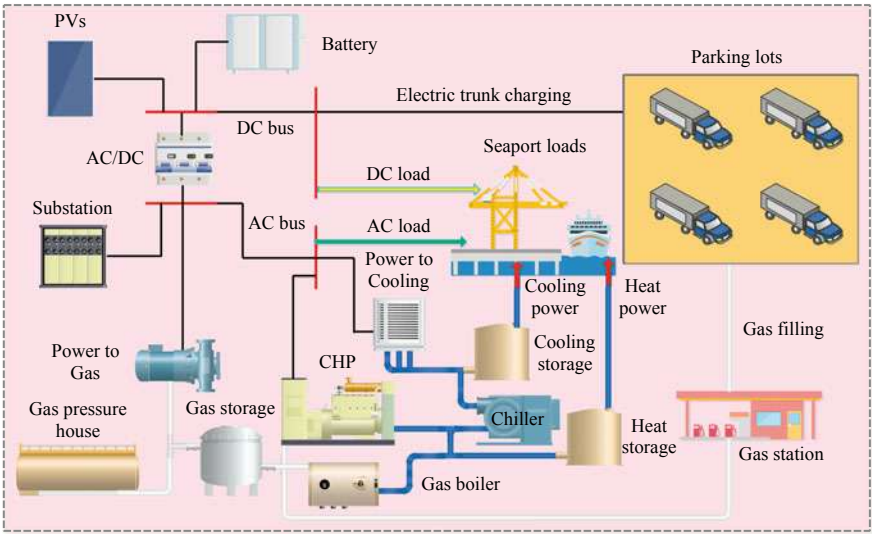

Fig. 7.10 An illustrated seaport microgrid case revised from [28]

the second stage, the seaport microgrid adjusts its scheduling plan responding to the realization of uncertainties in the hourly time-scale. The electrical load profile, heating load profile, and cooling load profile are shown in Fig. 7.11, which are all given in 1000 scenarios. Other detailed parameters can be found in [28].

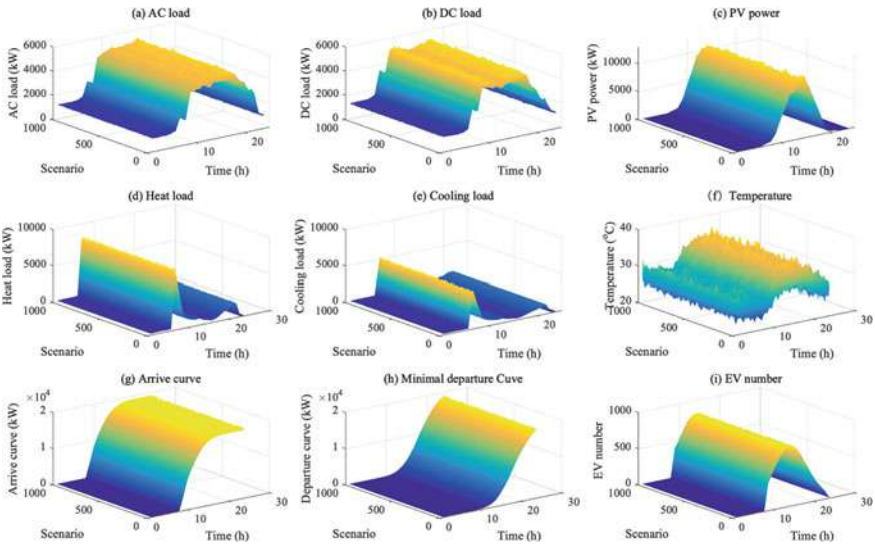

Fig. 7.11 Input parameters of the proposed method, reprinted from [28], open access

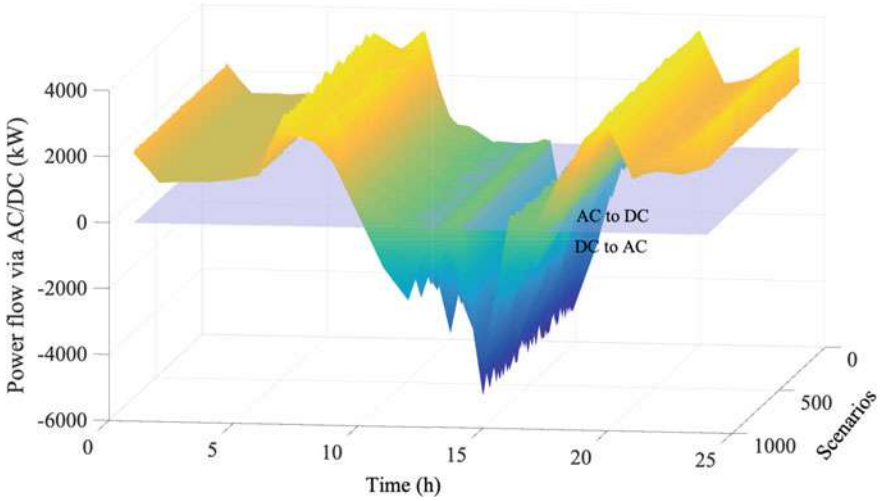

Fig. 7.12 Power flow via bi-directional AC/DC converter, reprinted from [28], open access

(2) Case study

To verify the effectiveness of the proposed method, different cases are formulated as follows.

Case 1: Two-stage optimization is considered, meanwhile the joint constraints are considered.

Case 2: Only the first-stage optimization is considered.

(2.1) Bi-directional AC/DC power flow

To show the coordination between AC and DC sides, the power flow via the bi-directional AC/DC converter is shown in Fig. 7.12. The AC to DC power is shown as the surface above the zero surface, while the DC to AC power is shown as the surface below the zero surface. Then, to show the effects of ESS, the state of charge (SOC) of battery is shown in Fig. 7.13.

From the above figure, at first, when the PV power is almost zero, i.e., $t = 0$–5 h, 20–24 h, the DC load is mainly met by AC to DC converter. When the DC load gradually increases, the AC to DC power is also increasing, and the battery discharges to further support DC load, i.e., $t = 5$, 6 h. After that, with the PV power increasing, the power demands also become larger, i.e., both DC and AC loads during $t = 10$–16 h. In those time intervals, the PV output is beyond the maximal DC load, which leads the PV power change to AC via AC/DC converter to support the AC load or charge into battery, which is shown as the surface below zero in Fig. 7.12 and the charging event in Fig. 7.13. From the above results, the integration of the AC/DC converter can bring great flexibilities to meet both DC and AC loads. The DC power for PV and AC power from UG and CHP can coordinately operate to enhance energy efficiency.

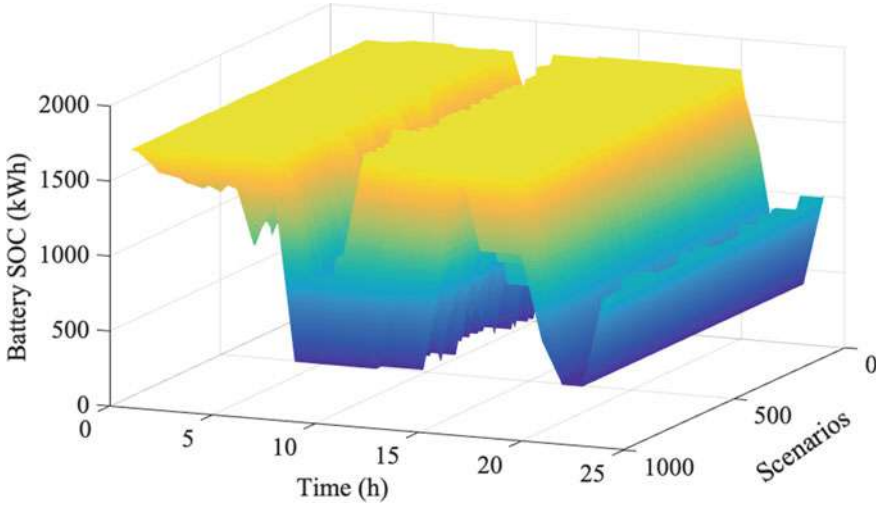

Fig. 7.13 SOC of battery, reprinted from [28], open access

(2.2) Multiple energy flows

In this seaport microgrid, various energy carriers are working coordinately to enhance operation flexibility. To show those coordinations, the power of CHP is shown in Fig. 7.14, the power of heat storage is shown in Fig. 7.15, the power of cooling storage is shown in Fig. 7.16, and the power of power-to-gas facility is shown in Fig. 7.17.

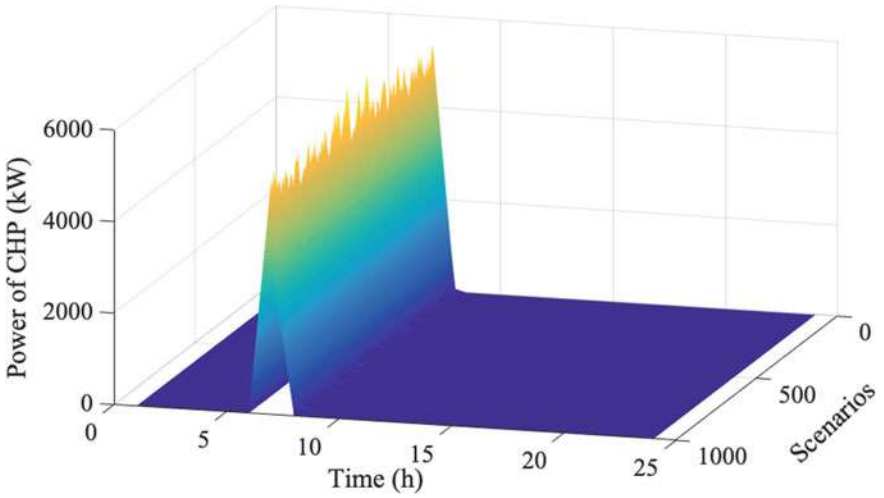

Fig. 7.14 Power of CHP, reprinted from [28], open access

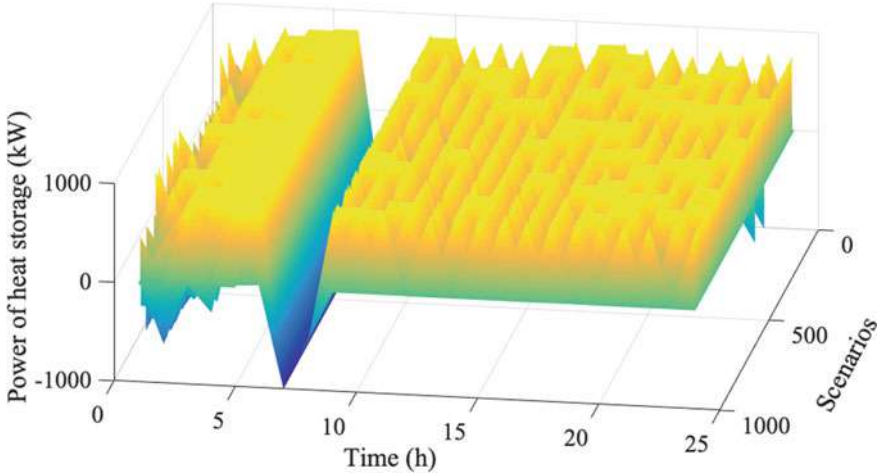

Fig. 7.15 Power of heat storage, reprinted from [28], open access

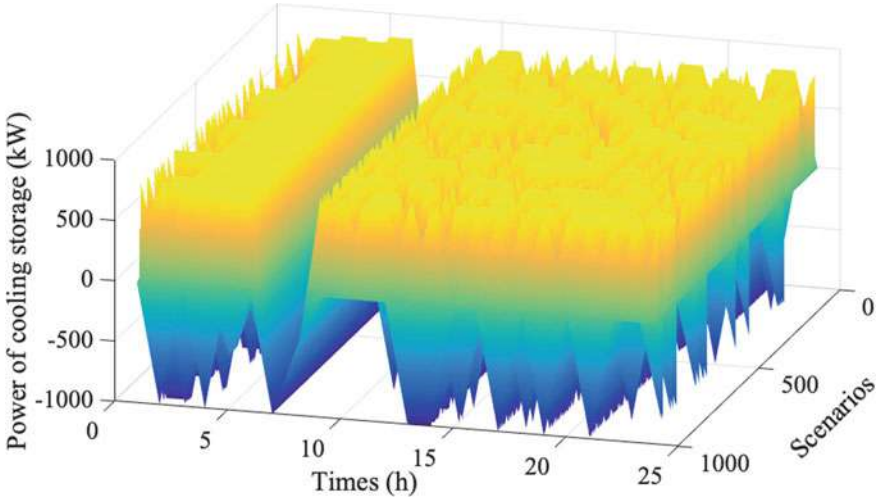

Fig. 7.16 Power of cooling storage, reprinted from [28], open access

From Fig. 7.11d and e, there are two demand impulses of both heat and cooling demands in $t = 6, 7$ h. The CHP responds to those demand impulses and consumes the gas to produce electricity and heat. The heat energy is stored and both the heat and cooling storages are discharging in this period to satisfy the demand, which is shown as the great valleys in their energy curves in Figs. 7.15 and 7.16. After that, CHP is shut-down since the total electricity demand is limited. The thermal demands are then met by the coordination of thermal storage and the gas boiler.

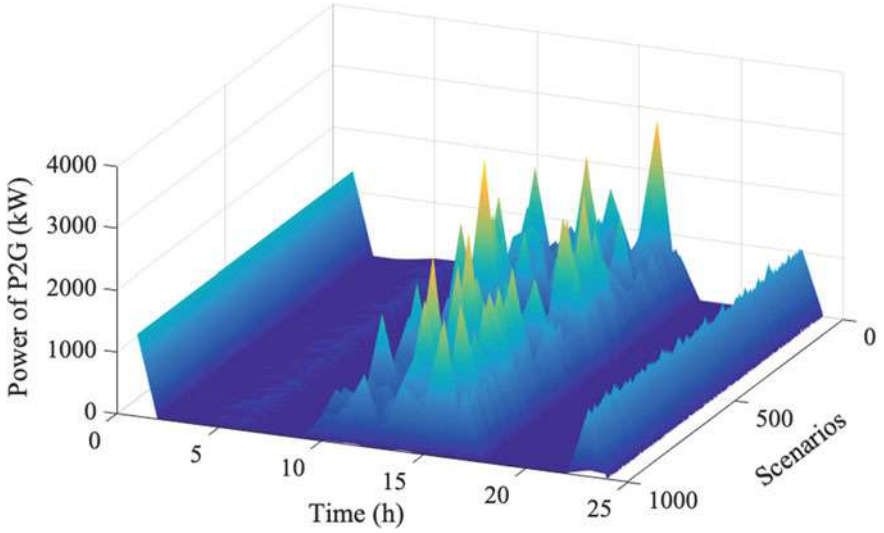

Fig. 7.17 Power of P2G equipment, reprinted from [28], open access

It should be noted that when $t = 10$–15 h, the temperature increases and requires great air-conditioning power demand. While in this time period, the PV power is also in its peak-hours. Then the PV power is converted to gas for the gas boiler to meet the air-conditioning power demand, which is shown as in Fig. 7.17.

The above results show that different energy carriers can be coordinated flexibly in a seaport microgrid. The excess electricity can be converted to gas for thermal demand. With the interactions between different energy carriers, the electric and thermal demand can both be satisfied and the flexibility can be enhanced.

(2.3) Electric and gas trucks

The energy demand of trucks is quite important in future seaport since they play a major role for cargo lifting and transporting. However, before the completed electrification of vehicles, the gas trunks and electric trunks will both exist in seaport microgrid. To satisfy their energy demands, the electric and gas sub-systems of seaport microgrid should be operated in coordination, respectively. In this case, the equivalent energy of gas trucks are shown in Fig. 7.18, and the charging power of electric trucks are shown in Fig. 7.19.

From Fig. 7.18, the energy peaks of gas vehicles are $t = 10$–15 h and 20–24 h. The first peak period corresponds to the working hours, and the second is the vehicles coming back for charging. From the results in Fig. 7.19, the charging patterns are more periodic with three peak hours, i.e., $t = 10$–15, 16–18, and 20–24 h. From the above results, both the gas and electricity demands of trunks can be satisfied.

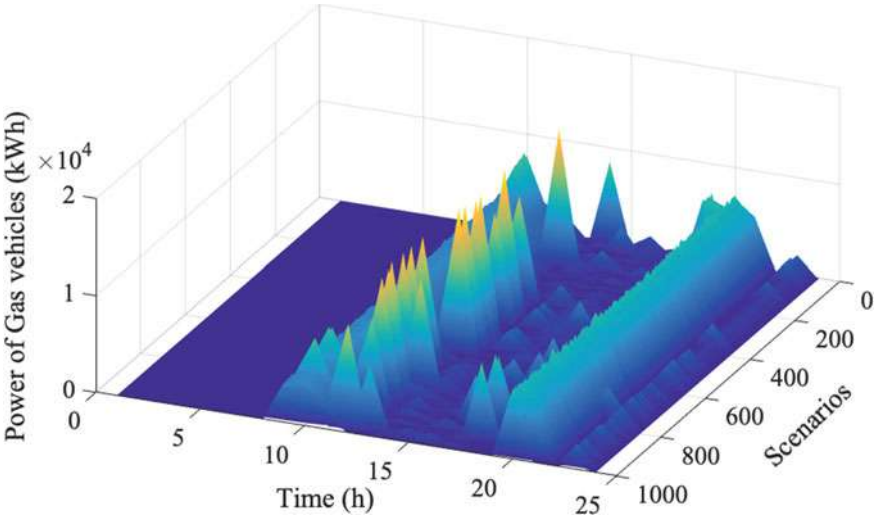

Fig. 7.18 Equivalent energy of gas vehicles, reprinted from [28], open access

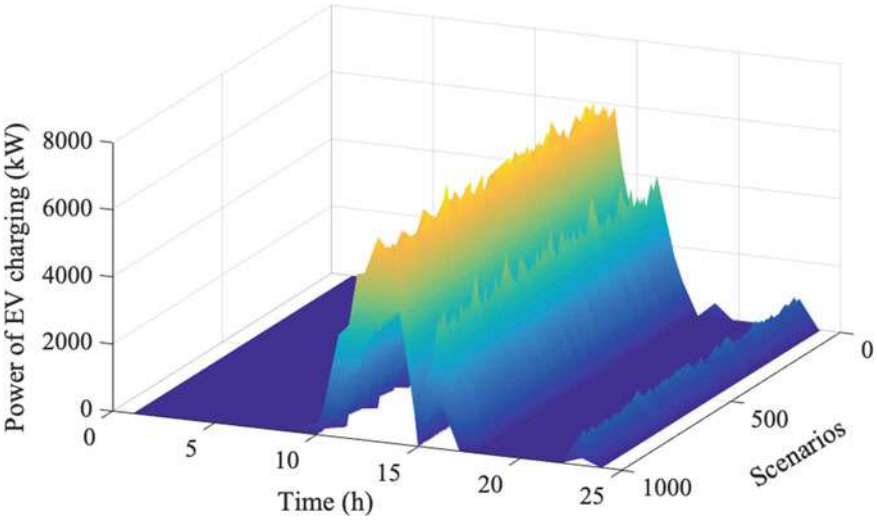

Fig. 7.19 Charging power of electric trunks, reprinted from [28], open access

References

1. Banakar, H., Luo, C., Ooi, B.T.: Impacts of wind power minute-to-minute variations on power system operation. IEEE Trans. Power Syst. **23**(1), 150–160 (2008)
2. Wang, J., Shahidehpour, M., Li, Z.: Security-constrained unit commitment with volatile wind power generation. IEEE Trans. Power Syst. **23**(3), 1319–1327 (2008)
3. Alguacil, N., Motto, A.L., Conejo, A.J.: Transmission expansion planning: A mixed-integer LP approach. IEEE Trans. Power Syst. **18**(3), 1070–1077 (2003)
4. Mancarella, P.: MES (multi-energy systems): an overview of concepts and evaluation models. Energy **65**, 1–17 (2014)
5. Gabrielli, P., Gazzani, M., Martelli, E., et al.: Optimal design of multi-energy systems with seasonal storage. Appl. Energy **219**, 408–424 (2018)
6. Clegg, S., Mancarella, P.: Integrated electrical and gas network flexibility assessment in low-carbon multi-energy systems. IEEE Transactions on Sustainable Energy **7**(2), 718–731 (2015)
7. Fabrizio, E., Corrado, V., Filippi, M.: A model to design and optimize multi-energy systems in buildings at the design concept stage. Renew. Energy **35**(3), 644–655 (2010)
8. Wen, Y., Qu, X., Li, W., et al.: Synergistic operation of electricity and natural gas networks via ADMM. IEEE Trans. Smart Grid **9**(5), 4555–4565 (2017)
9. Martinez-Mares, A., Fuerte-Esquivel, C.R.: A unified gas and power flow analysis in natural gas and electricity coupled networks. IEEE Trans. Power Syst. **27**(4), 2156–2166 (2012)
10. Qiao, Z., Guo, Q., Sun, H., et al.: An interval gas flow analysis in natural gas and electricity coupled networks considering the uncertainty of wind power. Appl. Energy **201**, 343–353 (2017)
11. Zhang, X., Shahidehpour, M., Alabdulwahab, A., et al.: Hourly electricity demand response in the stochastic day-ahead scheduling of coordinated electricity and natural gas networks. IEEE Trans. Power Syst. **31**(1), 592–601 (2015)
12. Chen, Y., Wei, W., Liu, F., et al.: A multi-lateral trading model for coupled gas-heat-power energy networks. Appl. Energy **200**, 180–191 (2017)
13. Chen, Y., Wei, W., Liu, F., et al.: Energy trading and market equilibrium in integrated heat-power distribution systems. IEEE Trans. Smart Grid **10**(4), 4080–4094 (2018)
14. Liu, X., Wu, J., Jenkins, N., et al.: Combined analysis of electricity and heat networks. Appl. Energy **162**, 1238–1250 (2016)
15. Dai, Y., Chen, L., Min, Y., et al.: Dispatch model of combined heat and power plant considering heat transfer process. IEEE Trans. Sustain. Energy **8**(3), 1225–1236 (2017)
16. Zamzam, A.S., Dall'Anese, E., Zhao, C., et al.: Optimal water–power flow-problem: Formulation and distributed optimal solution. IEEE Trans. Control Netw. Syst. **6**(1), 37–47 (2018)
17. Fooladivanda, D., Taylor, J.: Energy-optimal pump scheduling and water flow. IEEE Trans. Control Netw. Syst. **5**(3), 1016–1026 (2017)
18. Gan, L., Topcu, U., Low, S.: Optimal decentralized protocol for electric vehicle charging. IEEE Trans. Power Syst. **28**(2), 940–951 (2012)
19. Liu, Z., Wen, F., Ledwich, G.: Optimal planning of electric-vehicle charging stations in distribution systems. IEEE Trans. Power Deliv. **28**(1), 102–110 (2012)
20. Tushar, W., Saad, W., Poor, H., et al.: Economics of electric vehicle charging: A game theoretic approach. IEEE Trans. Smart Grid **3**(4), 1767–1778 (2012)
21. Liu, J., Zhang, J., Yang, Z., et al.: Materials science and materials chemistry for large scale electrochemical energy storage: from transportation to electrical grid. Adv. Func. Mater. **23**(8), 929–946 (2013)
22. Yao, S., Wang, P., Liu, X., et al.: Rolling optimization of mobile energy storage fleets for resilient service restoration. IEEE Trans. Smart Grid **11**(2), 1030–1043 (2019)
23. Rees, N.V., Compton, R.G.: Carbon-free energy: a review of ammonia-and hydrazine-based electrochemical fuel cells. Energy Environ. Sci. **4**(4), 1255–1260 (2011)
24. Li, Z., Xu, Y., Fang, S., et al.: Multiobjective coordinated energy dispatch and voyage scheduling for a multienergy ship microgrid. IEEE Trans. Ind. Appl. **56**(2), 989–999 (2019)

25. Kanellos, F.D.: Optimal power management with GHG emissions limitation in all-electric ship power systems comprising energy storage systems. IEEE Trans. Power Syst. **29**(1), 330–339 (2013)
26. Fang, S., Fang, Y., et al.: Optimal heterogeneous energy storage management for multi-energy cruise ships. IEEE Syst. J. (2020). (In press)
27. Norwegian Joy. https://www.ncl.com/in/en/cruise-ship/joy
28. Fang, S., Zhao, T., Xu, Y., et al.: Coordinated chance-constrained optimization of multi-energy microgrid system for balancing operation efficiency and quality-of-service. J. Mod. Power Syst. Clean Energy (2020). (In press)

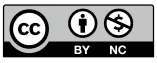

Chapter 8
Multi-source Energy Management of Maritime Grids

8.1 Multiples Sources in Maritime Grids

8.1.1 Main Grid

The main grid plays as the main power source of land-based maritime grids since the very beginning, such as the seaports and some coastal industries. This type of maritime grids usually operates in a harbor territory and can receive electricity from the harbor city. Some equipment in those maritime grids is driven by electricity and the others may be driven by fossil fuel. Table 8.1 shows the power sources of a terminal port.

From Table 8.1, electricity, diesel, petrol and natural gas are four main power sources for a terminal port, especially the electricity and diesel, serving for most of the port-side equipment. When a seaport is less-electrified, the portion from diesel is generally higher. In recent years, the extensive electrification of seaport becomes an irreversible trend, then the electricity now has become the primary power source of a seaport. Diesel now serves for some flexible operating equipment, such as trucks and other carriers. Similar phenomena also happen in other land-based maritime grids, such as coastal factories, since when fully electrified, electricity will serve as the main energy carrier and the main grid will be the main power source.

8.1.2 Main Engines

Most types of maritime grids cannot always receive power from the main grid. They mostly operate as islanded microgrids, such as island microgrids, shipboard microgrids, and various working platforms. For the island microgrids, if they cover a wide area, a small-scale or even medium-scale power plant is possible to construct,

S. Fang and H. Wang, *Optimization-Based Energy Management for Multi-energy Maritime Grids*, Springer Series on Naval Architecture, Marine Engineering, Shipbuilding and Shipping 11, https://doi.org/10.1007/978-981-33-6734-0_8

Table 8.1 Possible power sources for different equipment in a seaport (data from [1])

	Diesel	Petrol	Natural gas	Electricity
Ship-to shore cranes	•			•
Mobile cranes	•			•
Rail-mounted gantry	•			•
Rubber-tired gantry	•			•
Reach stackers	•			•
Straddle carriers	•			•
Lorries	•		•	•
Generators			•	
Building				•
Lighting				•
Reefer				•
Other vehicles	•	•	•	•

and this scenario is similar to the first case since the power plant can provide sufficient power support. For the other smaller cases, the main engines act as the main power sources instead, especially in the shipboard microgrids.

Generally, the main engines have four stages of development. The first stage is in 1900–1940, which is the initial stage of main engines. In 1910, the first diesel engine driven ship "Romagna" was launched. It uses two diesel engines manufactured by "Sulzer" company. Then in 1912, the first ocean cargo ship "Selandia" uses two DM8150x diesel engines manufactured by "B&M". In this stage, the main engines have the steamed ones and diesel ones. Then in 1940–1970, the development of main engines steps into the second stage, and this is the golden age of low-speed diesel engines. The power of a single air cylinder grows from 900–1030 kW in 1956 to 3400 kW in 1977. Then 1970–1990 is the third development stage of main engines. The theme of this stage is to reduce the fuel consumption rate. In this stage, the unit fuel consumption has reduced to 0.155–0.160 kg/(kWh), and the energy efficiency can be up to 55%. Then after 2000, the fourth stage, main engines become smarter and various advanced monitoring equipment is integrated to achieve automatic control.

Nowadays, main engines have different scales, from kilowatt to megawatt, which uses diesel, natural gas, ammonia, and so on. Some of them can use more than two types of fuels, referred to as "multi-fuel engines". Currently, main engines serve as the main power sources for many maritime grids.

8.1.3 Battery and Fuel Cell

In Chaps. 1 and 5, the energy storage technologies into maritime grids, especially the battery, are illustrated in detail. Battery stores energy in the electrochemical form

and the battery cells are connected in series or in parallel or both to make up the desired voltage and capacity. There are currently many cases of battery integrated ships. Some of them are shown in Table 8.2. Nowadays, battery mostly serves as auxiliary equipment to shave the peak load of ships and benefit the operation of shipboard microgrid. In the future, the battery integration into maritime grids will be more convenient and the large-scale integration will be reality.

Since no combustion process, fuel cell has higher power generation efficiency than the traditional internal combustion engine, which is a promising power source technology in the future. Table 8.3 shows some cases of fuel cell integrated ships.

Both of battery and fuel cell have no combustion process, and are highly efficient, which are promising for future usages.

Table 8.2 Cases of battery into ships

Name	Ship types	Battery capacity	References
Ampere	Ferry	1040 kWh	[2]
Norled	Ferry	1400 kWh	[3]
Puffer	Cargo ship	2400 kWh	[4]
Princess Benedikte	Cruise ship	2.6 MWh	[5]
Elektra	Hybrid ferry	1040 kWh	[6]
Tycho Brahe	Hybrid ferry	460 kWh	[7]
Deep ocean 01	OSV	2.8 MWh	[8]
Selbjørnsfjord	Cruise ship	585 kWh	[9]
Schleswig-Holstein	Cruise ship	1.6 MWh	[10]

Table 8.3 Projects of some selected fuel cell-based ships

Ship	Power	Fuel	References
Viking Lady	330 kW	LNG	[11]
SF-Breeze	100 kW	Hydrogen	[12]
PA-X-ELL	30 kW	Methanol	[13]
MV Undine	250 kW	Methanol	[14]
US SSFC	2.5 MW	Diesel	[15]
MC-WAP	500 kW	Diesel	[16]
MS Forester	100 kW	Diesel	[17]
212 submarine U31	330 kW	Hydrogen/Methanol	[18]
212 submarine U32	240 kW	Hydrogen/Methanol	[19]
S-80 Submarine	300 kW	Ethanol	[20]

8.1.4 Renewable Energy and Demand Response

In Chaps. 1 and 5, renewable energy integration into maritime grids has been illustrated. The following Fig. 8.1 shows renewable energy integration into a seaport. Wind power, solar energy, and the main grid supply the energy demand of seaport. The ships can charge or use cold-ironing power when berthed in a seaport, which can be also viewed as using renewable energy for propulsion.

However, renewable energy is highly fluctuating and less controllable. In conventional operation patterns, the generation-side should follow the trend of renewable energy or renewable energy has to be curtailed [21]. To mitigate this issue, the demand-side can be adjusted to follow the trend of renewable energy, then the operating burden of the generation-side can be greatly reduced and the total system benefits can be improved.

In literature, demand-side management has been used in power system operation [22, 23], unit commitment [24], and so on. In the energy market, the demand-side management sources can be aggregated as one unit and acting as a "virtual power plant". In maritime grids, demand-side management is used to adjust the propulsion system of AES [25]. Later in [26], demand-side management is used to mitigate the fluctuations of photovoltaic energy. Then [27] proposes a robust demand-side management method for a photovoltaic integrated AES.

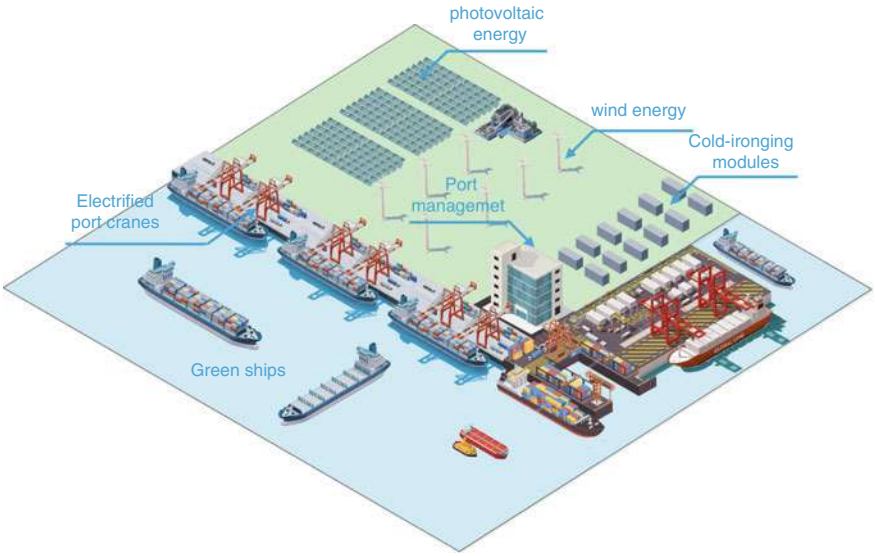

Fig. 8.1 Renewable energy integration into a seaport

8.2 Coordination Between Multiple Sources in Maritime Grids

From above, maritime grids involve multiple sources, including both generation-side and demand-side, and different sources should be coordinated to achieve better system behaviors. The coordination framework is shown as the following Fig. 8.2.

From Fig. 8.2, maritime grids consist of 4 main parts, (1) generation-side, including the main grid, main engines, fuel cell, various renewables, and so on; (2) demand-side, including the propulsion in ships, and port cranes and vehicles in a seaport, and all the load demand in different platforms; (3) Energy storage, including battery, flywheel and all the energy storage technologies can be used in maritime grids, and it should be noted that energy storage can change its roles between generation-side and demand-side, i.e., it is generation-side when discharging and it is demand-side when charging; (4) Multiple networks, including electrical, heat/cooling, water, and transportation networks, and those networks are used to deliver multiple energy flows from the generation-side to the demand-side. The energy storage and networks are the interfaces between generation-side and demand-side, thus the operating strategies of them can improve the flexibility of maritime grids.

In summary, maritime grids are a series of microgrids that have specific maritime load demand, and their operation strategies can be derived from the conventional land-based microgrids while addressing some specialties.

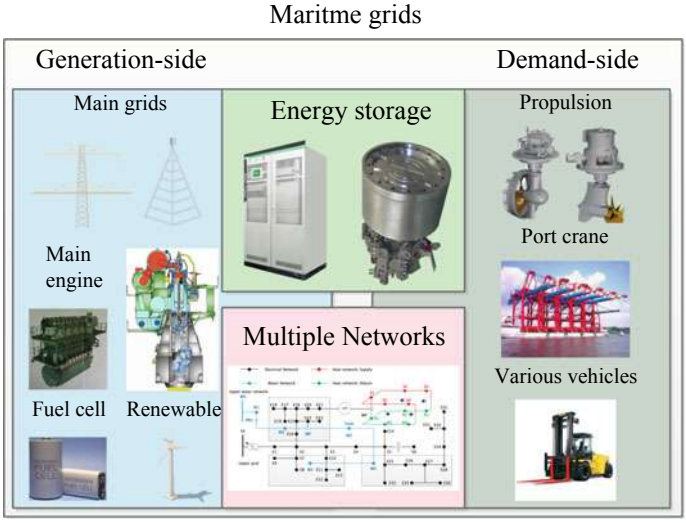

Fig. 8.2 Coordination framework of maritime grids

8.3 Some Representative Coordination Cases

8.3.1 Main Engine—Battery Coordination in AES

A single line diagram of AES is shown in Fig. 8.3 with two buses. 4 DGs are integrated into two buses. In this AES, bus A and bus B are both DC, and the DGs are all AC generators. The load demands include electric propellers and AC loads. Batteries are installed in two buses to act as auxiliary equipment.

Three sources are participating in the operation of AES, i.e., DGs, batteries, and the propulsion system of AES. The reason for the propulsion system to participate in demand response is shown as Fig. 8.4a, b.

In Fig. 8.4a, the propulsion load is cubically increasing with the cruising speed until the "wave wall". In Fig. 8.4b, the constant speed and variable speed both sail 30 nm in 6 h, but they have different load curves. In this sense, the propulsion system can adjust its load demand to coordinate with the DGs and battery to facilitate the operation of AES [25] has studied this topic and the main results are shown in Fig. 8.5a, b.

From the above Fig. 8.5a, b, the coordinated adjustment of propulsion and ESS can make the operating cost and EEOI smoother since it can mitigate the peak-valley difference of onboard power demand, which proves the effects of multi-source management on AES.

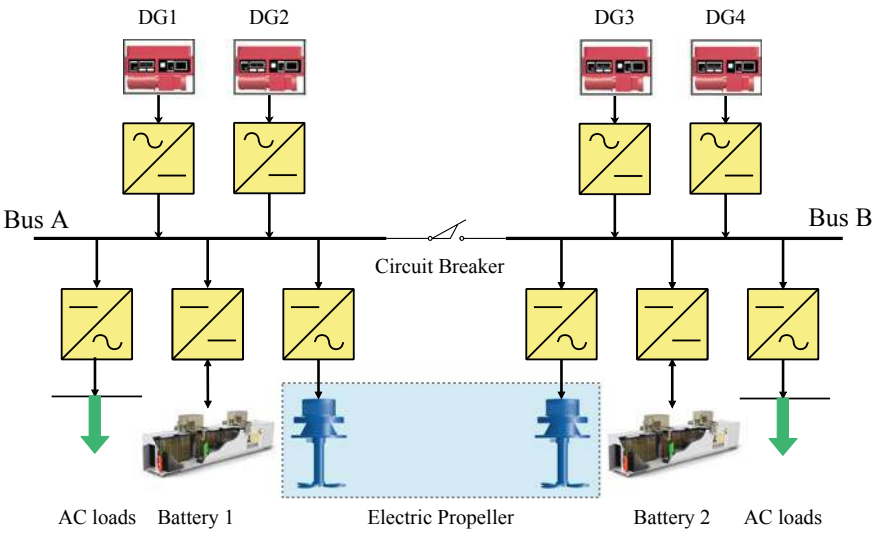

Fig. 8.3 Single-line diagram of an AES

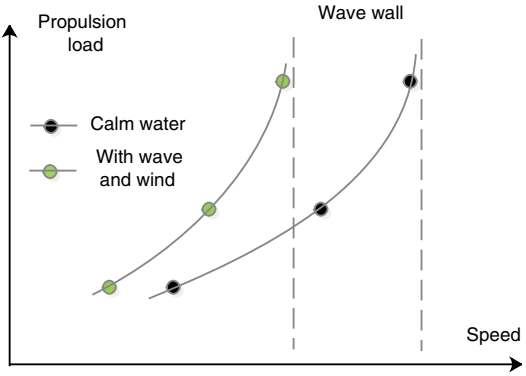

(a) Propulsion load of cruising speed

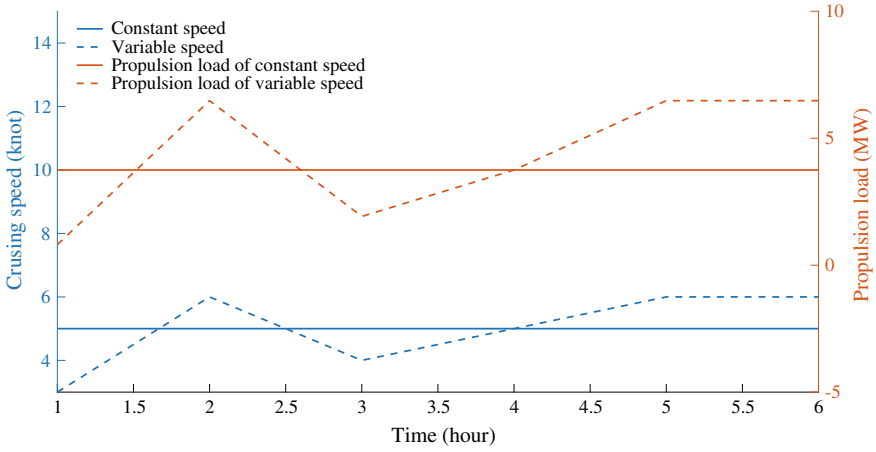

(b) Demand response of propulsion load

Fig. 8.4 Reason for propulsion system in demand response

8.3.2 Main Engine-Fuel Cell Coordination in AES

Compared with the main engines, fuel cell has smaller capacity and scale, which is suitable to undertake some small-scale load demands. Compared with the battery, fuel cell doesn't need charging, which can undertake long-term load demand [28] has studied this topic and compared two cases: (1) main engine; and (2) main engine-fuel cell. The testbed used in this study consists of a hybrid power source with the combined capacity of 180 kW (100 kW fuel cell, 30 kW battery, and 50 kW diesel generator). The results are shown in Fig. 8.6a, b. From the above curves, the integration of fuel cells can greatly reduce fuel consumption and CO_2 emission.

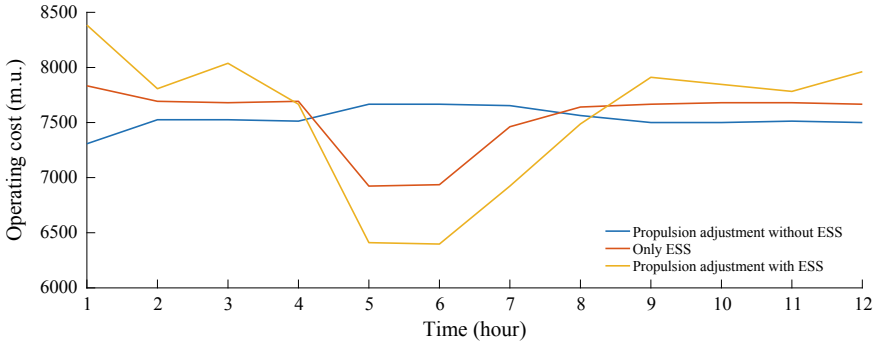

(a) Operating cost

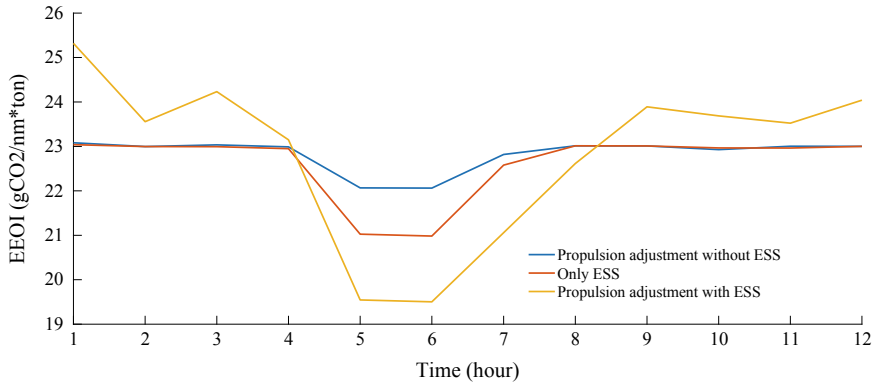

(b) EEOI

Fig. 8.5 Operating cost and EEOI with/without ESS

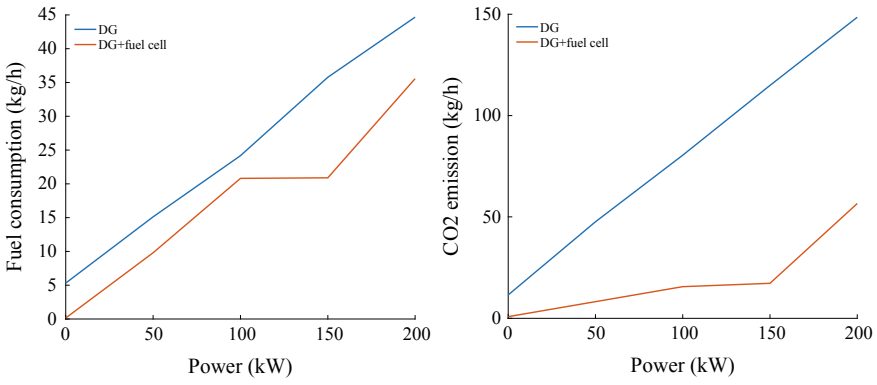

(a) Fuel consumption (b) CO2 emission

Fig. 8.6 Comparisons between DG and DG + fuel cell

8.3.3 *Demand Response Coordination Within Seaports*

Chapter 6 has illustrated the operation steps of quay crane (QC). Original Fig. 6.10 is now re-drawn as Fig. 8.7 below. A typical working process of a port crane includes (1) hoist, or beginning to lift up; (2) lifting up speedily; (3) lifting up speedily and the trolley moving forward; (4) lifting up with the full speed and the trolley moving forward; (5) lifting up with slowing speed and the trolley moving with full speed; (6) the trolley moving with slowing speed; (7) lifting down speedily and the trolley moving with slowing speed; (8) settling down. Step (2) and (3) usually have the biggest power demand whereas steps (6), (7) and (8) have smaller power demands.

Chapter 6 shows the integration of ESS can recover energy when lifting down the cargo. This Chapter proposes the demand response model of port crane. The dimension of QC, cargo speed, and QC power are shown in the sub-figures in Fig. 8.8. Based on Fig. 8.8, the entire lifting cargo distance is calculated as (8.1).

$$L = h_3 + (d_1 + d_2)/2 + (h_1 + h_2)/2 \tag{8.1}$$

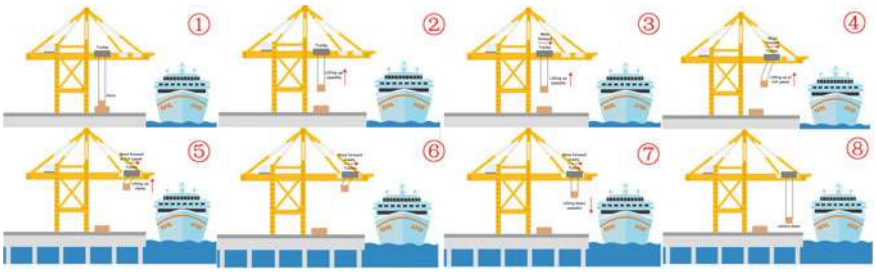

Fig. 8.7 Typical working steps for a port crane

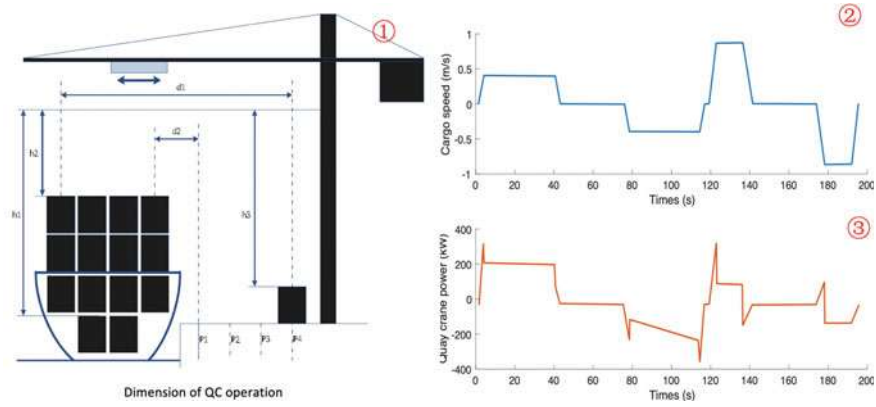

Fig. 8.8 Operation process of quay crane (QC)

From sub-figure ① and ②, the cargo speed and consumed power has a nearly linear relationship and can be shown as (8.2).

$$P = k \cdot v \tag{8.2}$$

where P is the power of QC; k is the coefficient; and v is the cargo speed. Then the average consumed power can be shown as (8.3).

$$P_{av} \cdot T_i = \int_0^{T_i} P dt = k \int_0^{T_i} v dt = k \cdot L \tag{8.3}$$

where P_{av} is the average consumed power of QC; T_i is the average handling time for one container. Then to handle n cargos, the consumed time is shown as (8.4).

$$T = n \cdot T_i = kL \sum_{i=1}^{n} (P_{av})^{-1} \tag{8.4}$$

Generally there exist an upper and a lower limit on the total handling time, i.e., $T_{min} \leq T \leq T_{max}$. Then the demand response model of QC can be obtained.

$$\frac{T_{min}}{kL} \leq \sum_{1}^{n} (P_{av})^{-1} \leq \frac{T_{max}}{kL} \tag{8.5}$$

Within the range in (8.5), the consumed power of QCs can be adjusted to facilitate the operation of seaport microgrids.

References

1. Wilmsmeier, G., Spengler, T.: Energy consumption and container terminal efficiency. Natural Resources and Infrastructure Division, UNECLAC, 2016. https://repositorio.cepal.org/handle/11362/40928?show=full
2. MV Ampere. https://en.wikipedia.org/wiki/MV_Ampere
3. Norled. https://en.wikipedia.org/wiki/Norled
4. Clyde puffer. https://en.wikipedia.org/wiki/Clyde_puffer
5. Princess Benedikte. https://www.cruisetimetables.com/cruises-from-copenhagen-denmark.html
6. The Elektra: Finland's first hybrid-electric ferry. https://ship.nridigital.com/ship_apr18/the_elektra_finland_s_first_hybrid-electric_ferry
7. MF Tycho Brahe. https://en.wikipedia.org/wiki/MF_Tycho_Brahe
8. Deep Ocean 01. http://www.sz.gov.cn/cn/xxgk/zfxxgj/tpxw/content/post_8012934.html
9. Selbjørnsfjord—Uavpic. https://uavpic.com/selbjornsfjord/
10. SMS Schleswig-Holstein. https://en.wikipedia.org/wiki/SMS_Schleswig-Holstein
11. Viking Lady. Available online: http://maritimeinteriorpoland.com/references/viking-lady/. Accessed 27 August 2018

12. SF-BREEZE. Available online: https://energy.sandia.gov/transportation-energy/hydrogen/marketransformation/maritime-fuel-cells/sf-breeze/. Accessed 27 August 2018
13. Pa-x-ell. Available online: http://www.e4ships.de/aims-35.html. Accessed 27 August 2018
14. METHAPU Prototypes Methanol SOFC for Ships. Fuel Cells Bull. 2008, 5, 4–5. 2859(08)70190-1
15. SFC Fuel Cells for US Army, Major Order from German Military. Fuel Cells Bull. 2012, 6, 4
16. Jafarzadeh, S., Schjølberg, I.: Emission reduction in shipping using hydrogen and fuel cells [C]// in Proceedings of the ASME International Conference on Ocean, Offshore and Arctic Engineering, Trondheim, Norway, 25–30 June 2017; p. V010T09A011
17. MS Forester. Available online: https://shipandbunker.com/news/emea/914341-fuel-cell-technologysuccessfully-tested-on-two-vessels. Accessed 27 August 2018
18. A Class Submarine. Available online: http://www.seaforces.org/marint/German-Navy/Submarine/Type-212A-class.htm. Accessed 27 August 2018
19. SSK S-80 Class Submarine. Available online: https://www.naval-technology.com/projects/ssk-s-80-classsubmarine/. Accessed 27 August 2018
20. Kumm, W.H., Lisie, H.L.: Feasibility study of repowering the USCGC VINDICATOR (WMEC-3) with modular diesel fueled direct fuel cells. Arctic Energies Ltd Severna Park MD: Groton, MA, USA (1997)
21. Fan, X., Wang, W., Shi, R., et al.: Analysis and countermeasures of wind power curtailment in China. Renew. Sustain. Energy Rev. **52**, 1429–1436 (2015)
22. Medina, J., Muller, N., Roytelman, I.: Demand response and distribution grid operations: opportunities and challenges. IEEE Transactions on Smart Grid **1**(2), 193–198 (2010)
23. Wang, Y., Pordanjani, I.R., Xu, W.: An event-driven demand response scheme for power system security enhancement. IEEE Trans. Smart Grid **2**(1), 23–29 (2011)
24. Zhao, C., Wang, J., Watson, J.P., et al.: Multi-stage robust unit commitment considering wind and demand response uncertainties. IEEE Trans. Power Syst. **28**(3), 2708–2717 (2013)
25. Kanellos, F.D., Tsekouras, G.J., Hatziargyriou, N.D.: Optimal demand-side management and power generation scheduling in an all-electric ship. IEEE Trans. Sustain. Energy **5**(4), 1166–1175 (2014)
26. Lan, H., Wen, S., Hong, Y.Y., et al.: Optimal sizing of hybrid PV/diesel/battery in ship power system. Appl. Energy **158**, 26–34 (2015)
27. Fang, S., Xu, Y., Wen, S., et al.: Data-driven robust coordination of generation and demand-side in photovoltaic integrated all-electric ship microgrids. IEEE Trans. Power Syst. **35**(3), 1783–1795 (2019)
28. Roh, G., Kim, H., Jeon, H., et al.: Fuel consumption and CO_2 emission reductions of ships powered by a fuel-cell-based hybrid power source. J. Marine Sci. Eng. **7**(7), 230 (2019)

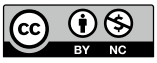

Chapter 9
The Ways Ahead

9.1 Future Maritime Grids

To illustrate the future maritime grids, we re-draw Fig. 4.1 here and give a more detailed illustration for future maritime grids. The following Fig. 9.1 is renamed as "future maritime grids".

In Fig. 9.1, the main types of maritime grids including harbor city grid (2), seaport microgrids (4), offshore platforms (10), shipboard microgrids (12), offshore wind farms (14), island microgrid (15).

In the first place, harbor city grid (2) is the core and acts as the main grid for the rest of maritime grids. The main functions include receiving the land-based renewable generation (1), supplying the industrial facilities (9), providing power to seaport microgrids (4), and operating two-way ferries (12) to island microgrid (15). The former four are energy connections and the fifth is a transportation connection.

Then seaport microgrid (4) is the network within a seaport, and this microgrid receives electricity from the harbor city grid (2) and providing raw materials to the industrial facilities (9). The seaport microgrid also receives energy from the seaport renewable (6). Seaport provides berth positions to the cargo ships (16), and handling the cargos by the port cranes (13). The cargos are then lifting by the transferring vehicles (5) to the stackyard (8), and the cold-chain containers are stored in the reefer area (7). Besides, seaport microgrid provides cold-ironing power to the shipboard microgrid (12).

The offshore platforms (10) include oil drilling platforms or other construction ships. They produce raw materials and transmit them to the industrial facilities (9) or island (15) by the oil pipes or other networks. The raw materials can be also transported by cargo ships (16).

The shipboard microgrid (12) is the network installed in cargo ships (16), offshore support vessels (3), and other ships. It receives the cold-ironing power from the seaport microgrid (4), and it periodically sails between seaport and islands (15) or other places to transfer cargos.

S. Fang and H. Wang, *Optimization-Based Energy Management for Multi-energy Maritime Grids*, Springer Series on Naval Architecture, Marine Engineering, Shipbuilding and Shipping 11, https://doi.org/10.1007/978-981-33-6734-0_9

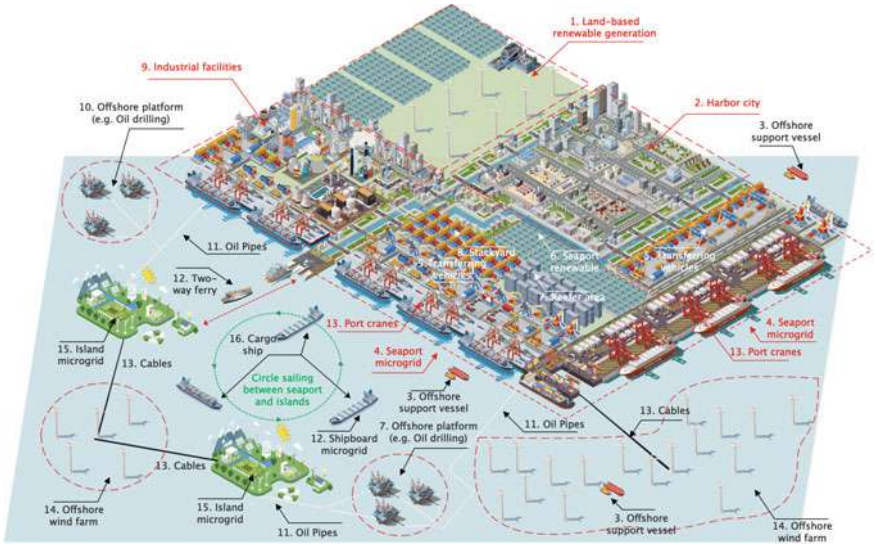

Fig. 9.1 Future maritime grids

Offshore wind farm (14) is to harvest wind energy on the sea. It has underground cables (13) to connect with the seaport (4) and then with the harbor city (2). It can also support the energy for the island microgrid (15). The offshore support vessels (3) are used to construct and repair offshore wind farms.

Island microgrid (15) is the microgrid within an island, which involves various renewable energy and other distributed generations. The scale of island microgrid depends on the area of island, and large island microgrid may have environmental agriculture facilities [1]. Island microgrid can receive the raw materials from the offshore platforms, and exchange materials with the seaport (4) by cargo ships (16). The tourists can have two-way traveling between islands and harbor city by two-way ferries (12).

From above, maritime grids undertake different maritime tasks and they are tightly coupled and they should be studied as one unit. Some typical operating scenarios are important and shown below.

(1) The coordination between the seaport microgrid and the harbor city grid. In this scenario, the harbor city grid is the main grid, and the seaport microgrid purchases electricity from the main grid to support the within equipment, i.e., port cranes, transferring vehicles, reefer area, and so on [2–4] have studied this scenario.

(2) The coordination between the seaport microgrid and the shipboard microgrids. In this scenario, the seaport allocates berth positions to the berthed-in ships and providing cold-ironing power and logistic services [5, 6] have studied this scenario.

(3) The coordination between the shipboard microgrids and the island microgrids. This scenario is similar to the case between seaport and ships when an island has a very strong power network. When the power grid of the island is weak, the ships may in reverse support the islands, which is referred to as "mobile power plant" [7].
(4) The coordination between the offshore platforms. There are generally many offshore platforms in an ocean area, and they should coordinate with each other to complete the same task, i.e., oil drilling, construction, and so on.

9.2 Data-Driven Technologies

9.2.1 Navigation Uncertainty Forecasting

Navigation uncertainty generally comes from uncertain weather, and Chap. 4 has emphasized the influences of navigation uncertainty on the operation of maritime grids. Until now, there are many data-driven maritime weather forecasting methods for ships and seaport [8–10], in different timescales, or by different algorithms, using different attributes, and also have different advantages and disadvantages. Our focus is on how to use those forecasting datasets to generate the distributions and uncertainty sets of energy management models. With the obtained distributions or uncertainty sets, stochastic and robust programming models can be formulated for different operating scenarios.

In recent research [11], a novel data-driven heuristic framework for vessel weather routing is formulated as Fig. 9.2. Based on the weather forecasting results, the ship chooses a better sailing route to save fuel consumption. The main key performance indicators (KPIs) of ships can also be predicted.

Fang et al. [12] also studies the robust energy management of all-electric ships when considering navigation uncertainties, but the weather conditions are simply classified as four sub-scenarios and only the worst case is considered. In the future, more accurate uncertainty sets should be forecasted to facilitate the operation of maritime grids.

9.2.2 States of Battery Energy Storage

Chapters 5–8 have emphasized the critical roles of battery energy storage in the maritime grids for load leveling and power quality issues. Generally, there are six states for battery energy storage, i.e., state of charge (SOC), state of power (SOP), state of energy (SOE), state of safety (SOS), State of temperature (SOT), and state of health (SOH). The above states are all essential indicators for the battery management system and many methods have been proposed to estimate them, and various data-driven techniques have been utilized.

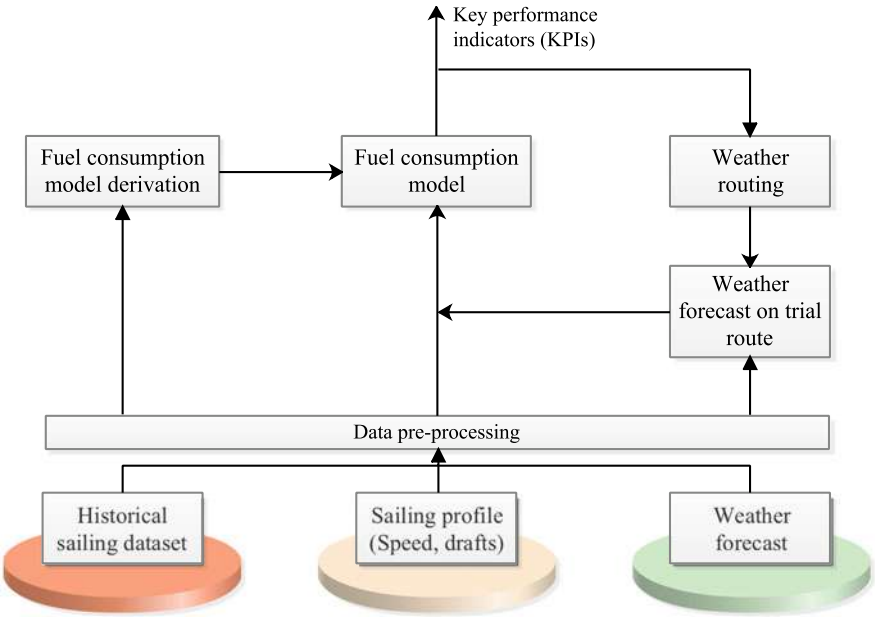

Fig. 9.2 Flowchart of the data-driven weather routing method

Generally, SOC is defined as the ratio of available capacity to the nominal capacity. Here the nominal capacity stands for the maximum amount of charge. Using the tank of a fuel vehicle as an analogy, SOC is similar to the fuel gauge. The definition of SOC is shown in (9.1) [13].

$$SOC(t) = SOC(t_0) + \int_{t_0}^{t} I(t) \cdot \eta \Big/ Q_n dt \tag{9.1}$$

where $I(t)$ is the current of battery energy storage; Q_n is the nominal capacity; η is the coulombic efficiency.

Another indicator, SOP is generally defined as the available power that a battery can supply to or absorb over a time horizon [14]. The definition of SOP is shown as (9.2).

$$\begin{cases} SOP^{charge}(t) = max\left(P_{min}, V(t+\Delta t) \cdot I_{min}^{charge}\right) \\ SOP^{discharge}(t) = min\left(P_{max}, V(t+\Delta t) \cdot I_{max}^{discharge}\right) \end{cases} \tag{9.2}$$

where P_{min} and P_{max} are the lower and upper limits of power; I_{min}^{charge} and $I_{max}^{discharge}$ are the lower and upper limits of current.

Another indicator, SOE is defined as the supplying/absorbing discrepant energy amounts in different voltage levels, which is given as (9.3).

$$SOE(t) = SOE(t_0) + \int_{t_0}^{t} P(t) \Big/ E_N dt \tag{9.3}$$

where $P(t)$ is the power; E_N is the nominal energy capacity.

Another indicator, SOS represents the hazard level when battery operating, and the definition is given as (9.4).

$$H_r = H_s \cdot H_l \tag{9.4}$$

where H_r, H_s, H_l represent the hazard risk, hazard severity, and hazard likelihood, respectively. In [15], H_s can vary from 0 to 7 as an integer to represent the hazard level; H_l can take values from 1 to 10 to represent the occurrence percentage of failures; H_r utilizes two states (i.e., H_s and H_l) to find a safe operating region.

The temperature has been recognized as one main factor for battery degradation, and the SOT indicates the operating temperature of battery, including the estimations of external, internal, and temperature distribution. In general, the external temperature is easy to control, and the internal temperature and temperature distribution are much more important to represent the state of battery. The estimation of SOT is based on the thermal dynamic model as (9.5) [16].

$$\begin{cases} C_C \cdot \dot{T}_c = \dot{Q} + (T_s - T_c) \Big/ R_x \\ C_S \cdot \dot{T}_S = (T_\infty - T_s) \Big/ R_u + (T_S - T_c) \Big/ R_c \end{cases} \tag{9.5}$$

where T_s and T_c are the surface and core temperature, respectively; R_u and R_c are the conductive and convective resistances, respectively; T_∞ is the ambient temperature. The last indicator is the SOH to represent the health state of battery, which is given by the following.

$$SOH = C_a \Big/ C_r \times 100\% \tag{9.6}$$

where C_a and C_r are the actual and rated capacity, respectively.

There are many estimation methods for the above six states of battery energy storage [13–20], and these methods belong to multiple timescales, which are shown as Fig. 9.3 below.

Besides, there are different timescales for each state. For example, there are offline training and online estimation stages for SOH estimation in Fig. 9.4 [21].

In summary, current state estimation methods can be used in maritime grids when addressing the working conditions of highly humid and saline, and high-temperature. In Fig. 9.4, these characteristics should be considered in the experimental conditions and the uncertainty management of SOH estimation model. However, there is still very little literature on this topic now.

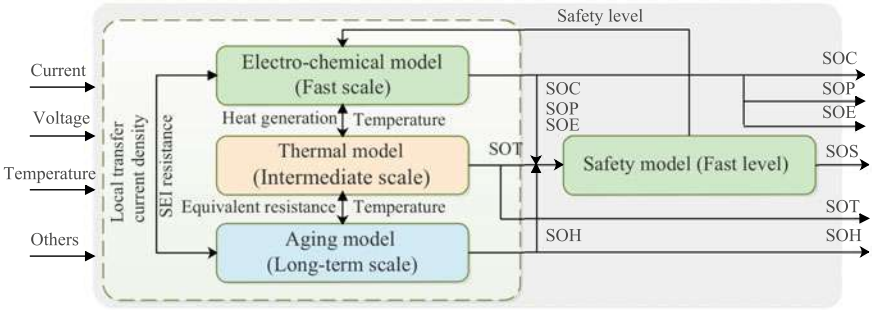

Fig. 9.3 Time-scale of state estimation of battery

Besides, the above state estimation methods are for a single battery cell. As shown in Fig. 9.5, a battery pack is comprised of many battery cells and generally different cells have different degradation speeds. This difference should be considered, named as the inconsistency of state estimation.

9.2.3 Fuel Cell Degradation

The importance of fuel cells in maritime grids has been clarified in Chap. 8, and the technological development will drive the further large-scale integration of fuel cells. Similar to battery, the degradation of fuel cells is important and certain methods should be proposed to estimate the degradation in different scenarios. Generally, the fuel cell degradation methods can be classified as (1) stack voltage degradation model; (2) Electrochemical impedance spectrometry (EIS) impedance estimation; (3) Remaining useful life (RUL) estimation. Their advantage and disadvantages are shown in Table 9.1.

The stack voltage degradation models use the output voltage V_{stack} to demonstrate the degradation phenomenon, and are usually based on two prototypes, shown in (9.7) and (9.8), respectively.

$$\begin{cases} V_{stack} = V_{rate} \cdot D_{fc} \\ D_{fc} = k_p \cdot (P_1 \cdot n_1 + P_2 \cdot n_2 + P_3 \cdot t_1 + P_4 \cdot t_2) \end{cases} \tag{9.7}$$

$$V_{stack} = V_0 - b \cdot \log(i_{fc}) - r \cdot i_{fc} + \alpha \cdot i_{fc}^{\sigma}(1 - \beta \cdot i_{fc}) \tag{9.8}$$

In (9.7), V_{stack} is the stack voltage; D_{fc} is the degradation rate; k_p is the accelerating coefficient; P_1,P_2,P_3 and P_4 are the degradation rates led by the load change, start-up/shut-down, idling, and high-power demand, respectively; and n_1, n_2, t_1, t_2 denotes the corresponding times/time-periods. In (9.8), V_0 represents the open-circuit voltage; i_{fc} is the current of fuel cell; b, r, α, and σ are parameters deduced from the experiment dataset. When the dataset changes, all the parameters should be adjusted.

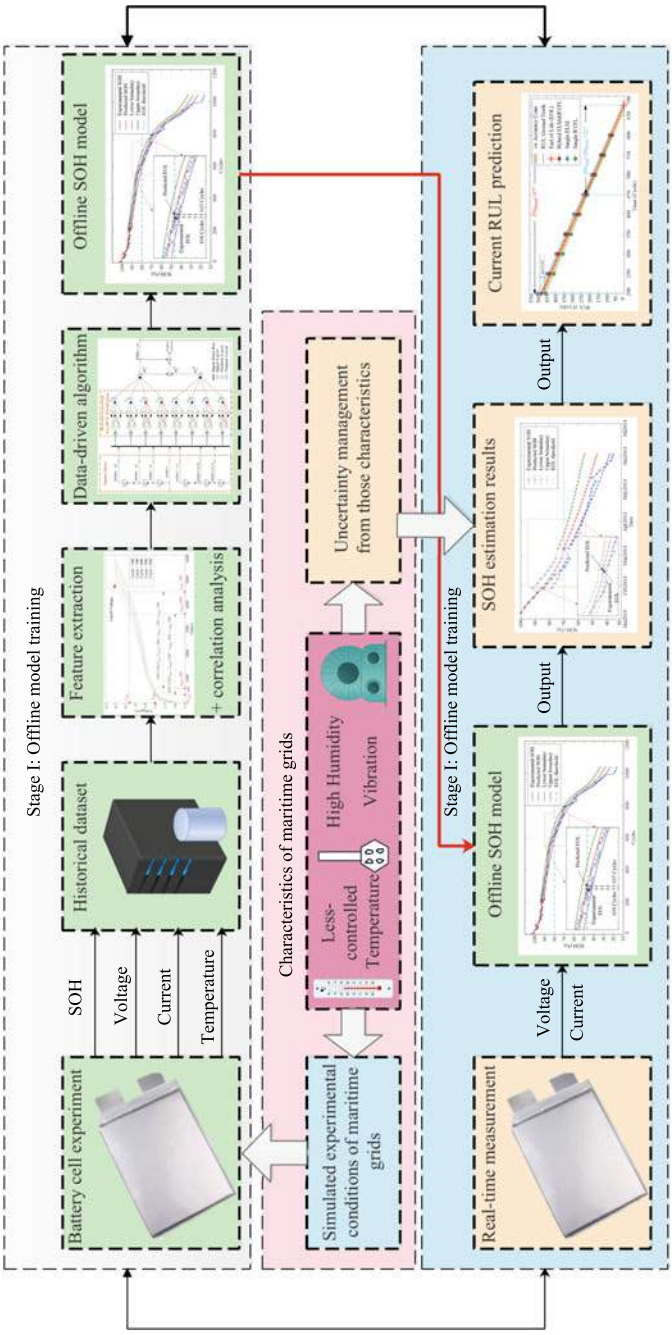

Fig. 9.4 Time-scale of state estimation of battery

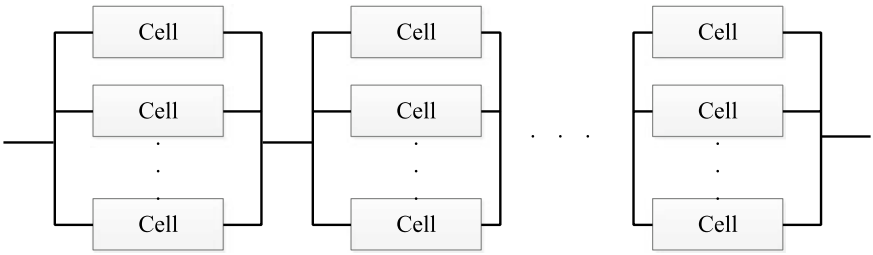

Fig. 9.5 Battery cells and Battery pack

Table 9.1 Summary of different fuel cell degradation methods

Model	References	Methods	Advantages	Disadvantages
Stack voltage degradation model	[22–24]	data-driven parameter recognization	1. Easily implement 2. Less requirement on theoretical analysis	1. Highly rely on experiment 2. Hard to adjust the parameters
EIS impedance estimation	[25, 26]	Model-based methods	1. Easily implement 2. Suitable for diagnostics field	Cannot directly forecast SOH
RUL estimation	[27–29]	Hybrid methods	Robustness to uncertainties	Computational stress

EIS is carried out by adding a small sinusoidal perturbation on the nominal current and then the EIS impedance can be calculated as the ratio between the response and the perturbation. This method can characterize the phenomenon inside the fuel cell and evaluate the fuel cell degradation [25], which are widely used in the diagnostics field, but it cannot give the information of SOH. RUL methods are a series of hybrid methods, which can be based on the semi-empirical model [28], or various machine-learning methods [30]. Since the recent development of data-mining techniques, RUL methods also have many new applications [30].

In summary, the fuel cell degradation estimation is similar to the battery and a similar estimation process can be utilized. The gaps before implementing in maritime grids are addressing the working conditions with high humidity, and high-temperature. However, there is still very little literature working on this topic.

9.2.4 Renewable Energy Forecasting

Chapter 5 has emphasized the importance of renewable energy forecasting of maritime grids. Figures 5.10 and 5.11 show that the forecasting of renewables onboard should consider more features. To recall this part, Figs. 5.10 and 5.11 are re-drawn as Fig. 9.6a, b as follows.

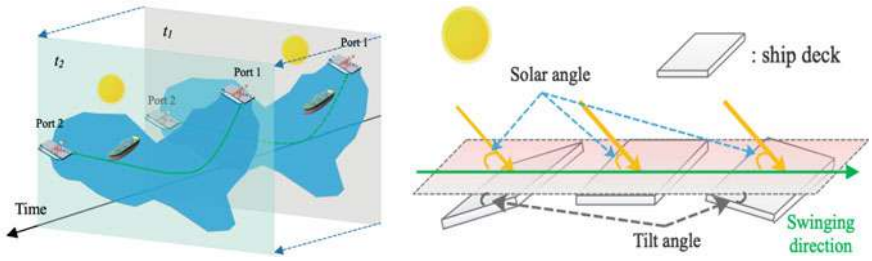

(a) Ship motion (b) Ship deck rolling

Fig. 9.6 Two extra features in onboard renewable energy forecasting [31]

An adaptive clustering method for onboard photovoltaic energy is proposed in [32]. The sketch process is shown in Fig. 9.7.

With the proposed method, the scenarios of photovoltaic energy can be adaptively obtained, and the administrator can give an optimal energy scheme for each scenario. Later in [33], the ship motion, temperature, irradiance, and temperature are all considered and a hybrid ensemble forecasting method is formulated as Fig. 9.8.

With the proposed method in Fig. 9.8, the onboard photovoltaic energy can be predicted with more accuracy. Two representatives above show the keys for the renewable energy forecasting in maritime grids: (1) properly clustering the original dataset, and the main reason is the weather conditions may change more frequent in maritime grids than other land-based applications; (2) putting more practical features into the forecasting model, such as the ship motion and rolling. With the development of renewable energy technology, the penetration of large-scale renewable energy into maritime grids will become reality, and the renewable energy forecasting in maritime grids will find a promising scenario for application.

9.3 Siting and Sizing Problems

9.3.1 Energy Storage Integration

Chapter 6 has clarified the functions of energy storage in the long-term operation of maritime grids: (1) improving economic and environmental characteristics of maritime grids [5, 12, 34]; (2) benefiting the operation of onboard equipment [31, 32, 35]; (3) improving the resilience of maritime grids [36], which are illustrated in Fig. 9.9.

In Fig. 9.9a, the main engines and energy storage are sharing the highly fluctuated power demand via maritime grids. The energy storage shares the highly fluctuated part and the main engines can work in a constant and economic working condition. In Fig. 9.9b, new equipment is integrated into the maritime grid, and the energy storage

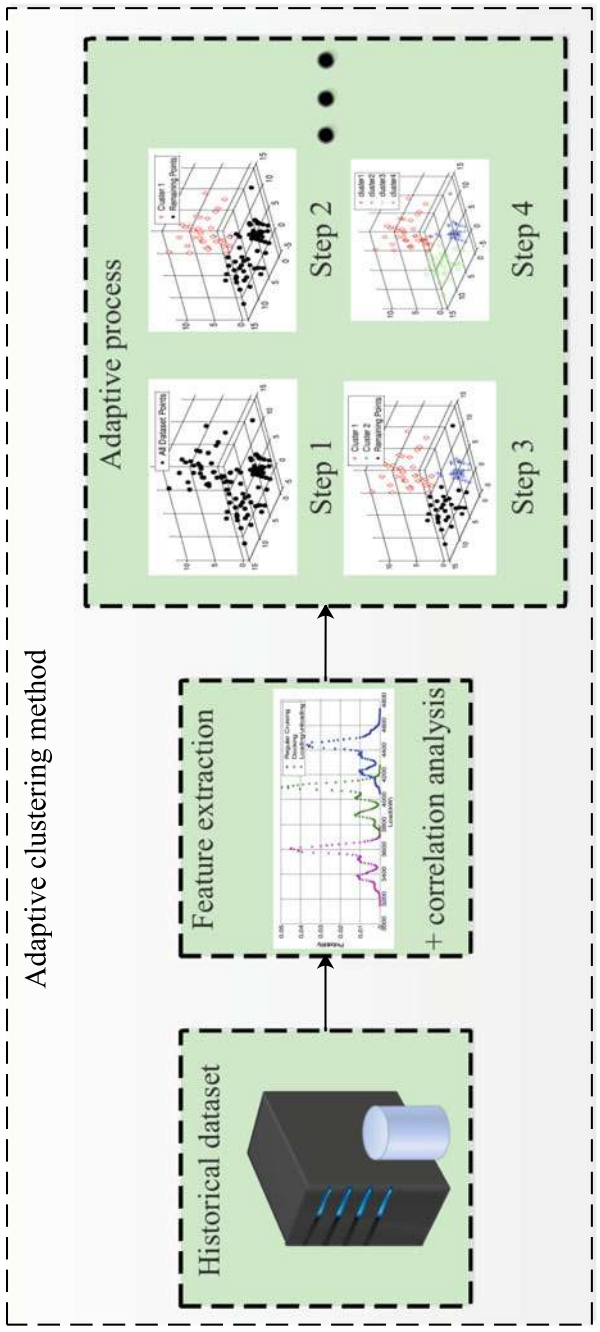

Fig. 9.7 Adaptive clustering methods for onboard photovoltaic energy

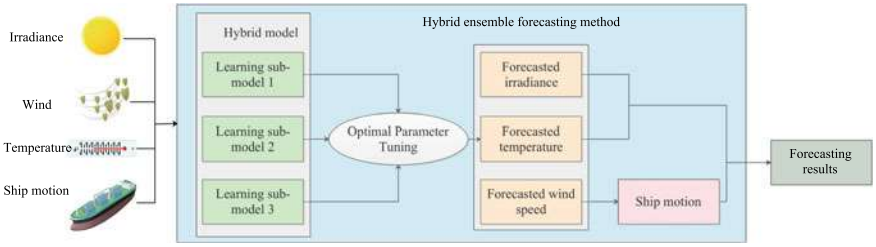

Fig. 9.8 Hybrid ensemble forecasting method

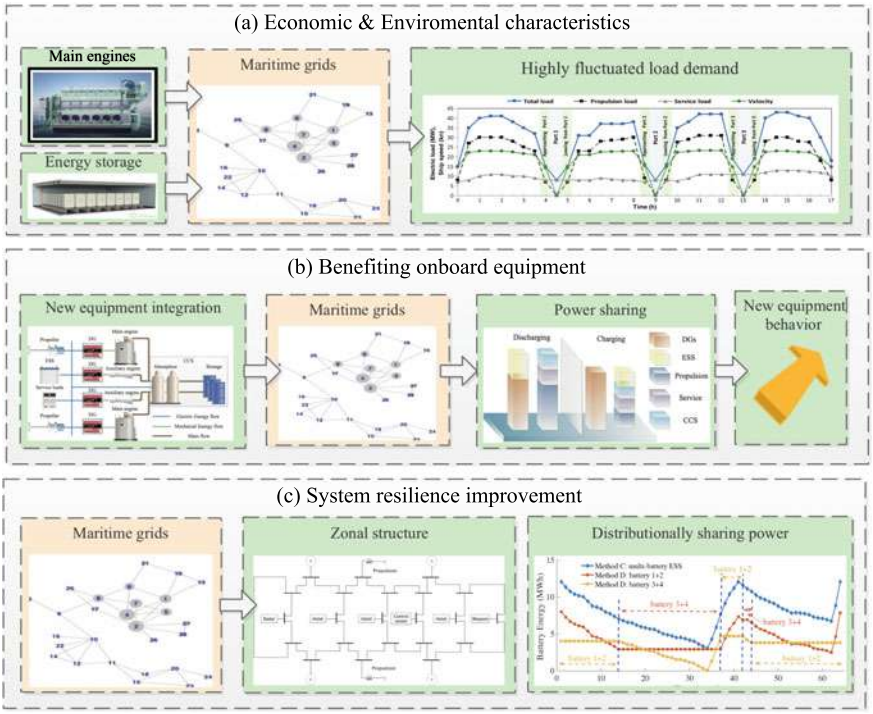

Fig. 9.9 Main functions of energy storage in maritime grids

can share the power demand of new equipment to improve its behavior. In Fig. 9.9c, energy storage is installed distributionally in different zones of maritime grid, and energy storages in different zones share the power demand, and make the system be resilient to various failures.

Since the important functions above, energy storage gradually becomes essential equipment in maritime grids to improve system characteristics. However, energy

storage, generally battery for long-term operation, is still expensive and the installment area is also another limit for energy storage. The balance between the economic benefits and the system characteristics motivates the siting and sizing problems of energy storage.

Reference [32, 37, 38] propose optimal energy storage sizing methods after comprehensively studying the influences of energy storage on the penetration of photovoltaic energy into maritime grids, which considers effects of the ship motion, deck rolling, and solar irradiation density. In seaport, [2] proposes six indexes to indicate the green operation, and a two-stage energy storage sizing problem is formulated to improve the indexes. Since the battery is limited in power density, [34, 39] propose optimal sizing methods for hybrid energy storage, i.e., high power density energy storage for the high-frequency load demand, and battery for the low-frequency load demand. For the system resilience, a distributed energy storage siting and sizing model is formulated, and the simulation results show that the distributionally installed energy storages benefit the resilience.

In summary, future research should consider more specialties of maritime grids, which are shown as follows.

(1) Special network structures. Maritime grids have a different network structure compared with conventional land-based microgrids. This feature in ships has been illustrated in Chap. 5 as Fig. 5.11. We re-draw this figure to Fig. 9.10 below, and we can find the network structure of ships is zonal and parallelly designed.
(2) The distributional installment of energy storage. Different from the land-based applications, the energy storages in maritime grids are mostly distributionally installed. For example, the energy storage system in ships is usually separated into several parts and installed in different watertight compartments for system

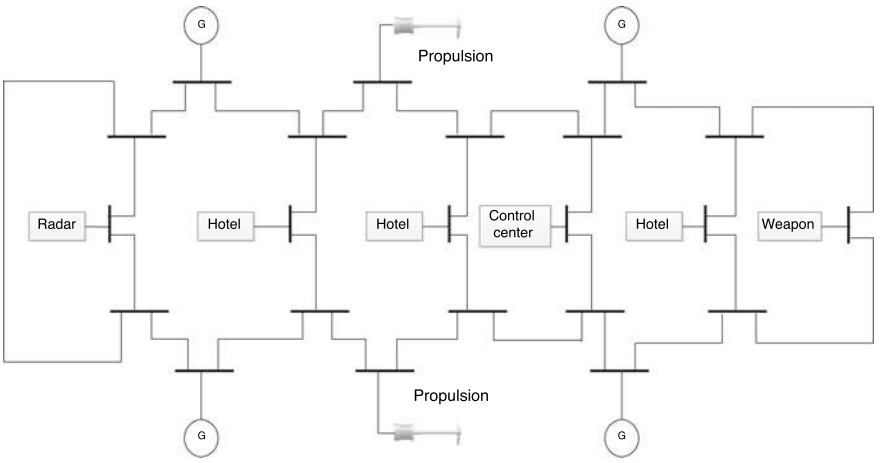

Fig. 9.10 The graph topology of an all-electric ship

resilience. In seaport, energy storages have different functions, i.e, for cold-ironing, for port cranes, for electric truck charging, and so on. So the energy storages also need to be distributionally installed.

(3) The redundant capacity of energy storage. Different from conventional land-based microgrids, maritime grids generally receive less support from the main grid. In this sense, energy storage is viewed as one of the main power sources to improve system resilience, and therefore needs to have a redundant capacity.

9.3.2 Fuel Cell Integration

Chapter 8 has revealed the fuel cell is a promising power source for the future maritime grids, and its integration is an irreversible trend. Currently, there are many practical cases and studies on the siting and sizing of fuel cells in maritime grids. With these cases, fuel cell shows similar effects as the integration of energy storage, i.e., highly flexible, energy-efficient, no combustion process, and easily maintained. The functions are also similar: (1) improving economic and environmental characteristics of maritime grids; (2) benefiting the operation of onboard equipment; (3) improving the resilience of maritime grids. Although these similarities, fuel cell is a power source and has no need to charge, and therefore the fuel cell is able to sustain the long-term power demand.

As above, future research should consider the following aspects as Fig. 9.11 before it can integrate into maritime grids.

(1) Fuel cell is a power source and has similar functions with the main engines. In this sense, the maritime grids should be expanded for its integration, i.e., structure modification.

(2) Generally, fuel cell and main engines serve different load demands, i.e., main engines for the large-scale load demand such as propulsion, and fuel cell for the small-scale but critical load demand such as control center. The division of responsibilities should be considered.

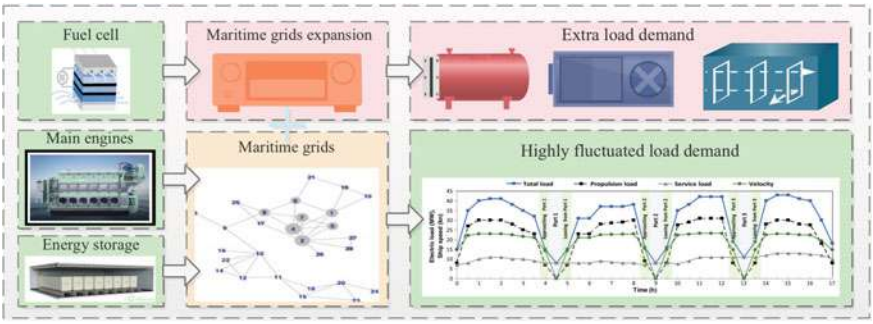

Fig. 9.11 Fuel cell integration and maritime grid expansion

9.4 Energy Management

With the above illustrations, the main target for maritime grids is to achieve the cost-efficient and green development of the maritime industry, and the energy management methods/strategies are fundamental for this target. In the future, the energy management of maritime grids should have two main abilities: (1) Ambient environment perception, i.e., the real-time perception of working conditions and the quick responding abilities for the changes of working conditions. (2) Optimal energy scheduling ability, i.e., real-time perception of system conditions and the ability for the optimal energy scheduling among different sources and equipment. These two abilities are shown in Fig. 9.12 below.

From Fig. 9.12, the first ability, ambient environment perception, relies on real-time data measurement and the corresponding data-driven techniques. This ability can provide adequate inputs to indicate the energy scheduling of maritime grids. It should be noted that the ambient environment includes the working conditions and the coordination from other maritime grids, such as the coordination between berthed-in ships and seaport.

Then the second ability, optimal energy scheduling ability, should integrate all the current management methods, i.e., the methods mentioned in Chaps. 5–8, namely, uncertainty management, energy storage management, multi-energy management, and multi-source energy management, and determines an optimal energy scheme to respond to the ambient working conditions.

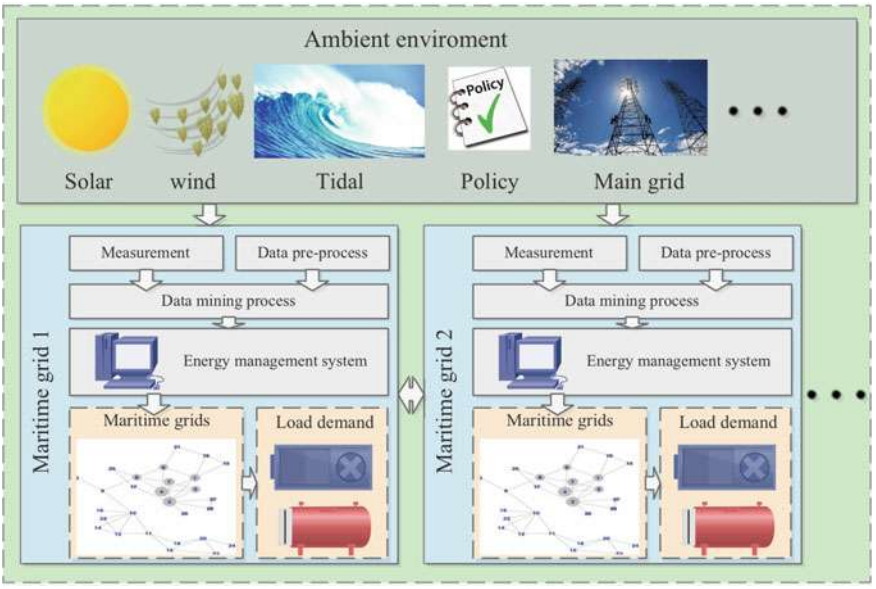

Fig. 9.12 Energy management of maritime grids

9.5 Summary

Generally, maritime grids are born under the trend of maritime transportation electrification, and this trend is irreversible in the future. From the views of electrical engineering, maritime grids are a series of microgrid-scale networks which undertake different maritime tasks. The electrical network serves as the backbone and connects with other networks with different functionalities. This characteristic determines the operation of maritime grids should have plenty of similarities with conventional microgrids, but the maritime tasks involved further make the maritime grids with many distinguishing features. In this sense, it is essential and also very necessary to study this type of special microgrids before they can be implemented in real-world.

In this book, maritime grids are defined as those networks installed in harbors, ports, ships, ferries, or vessels. A typical maritime grid consists of generation, storage, and critical loads, and can operate either in grid-connected or in islanded modes, and operate under both the constraints of the energy system and maritime transportation system, and formulates as a "maritime multi-energy system", and the energy management of this special system will shape the energy efficiency improvement of the future maritime transportation system.

In this book, optimization-based energy management methods are comprehensively reviewed and overviewed with plentiful case studies. In Chaps. 1–4, i.e., (1) the introduction for maritime grids, (2) the mathematical basics of optimization; (3) mathematical formulation of management targets and (4) formulation and solution of maritime grid optimization, give illustrative descriptions on the research focus. Then in Chaps. 5–8, four aspects, i.e., (1) energy management under uncertainties, (2) energy storage management, (3) multi-energy management, and (4) multi-source energy management, are discussed. At last, this chapter overviews the future roadmap in four parts, i.e., (1) future maritime grids, (2) data-driven technologies, (3) siting and sizing problems, and (4) energy management. With the above arrangement, the initial research framework of maritime grids has been launched and specific efforts are expected in this field for future development.

References

1. Walsh, K., O'Sullivan, D., Young, R. et al.: Medieval land use, agriculture and environmental change on Lindisfarne (Holy Island), Northumbria. Ecological relations in historical times: human impact and adaptation, pp. 101–21 (1995)
2. Molavia, A., Shib, J., et al.: Enabling smart ports through the integration of microgrids: a two-stage stochastic programming approach. Appl. Energy **258**, 114022 (2020)
3. Kanellos, F.D., Volanis, E.S., Hatziargyriou, N.D.: Power management method for large ports with multi-agent systems. IEEE Trans. Smart Grid **10**(2), 1259–1268 (2017)
4. Gennitsaris, S.G., Kanellos, F.D.: Emission-Aware and cost-effective distributed demand response system for extensively electrified large ports. IEEE Trans. Power Syst. **34**(6), 4341–4351 (2019)

5. Wen, S., Zhao, T., Tang, Y., et al.: A joint photovoltaic-dependent navigation routing and energy storage system sizing scheme for more efficient all-electric ships. IEEE Trans. Transp. Electrif. **6**(3), 1279–1289 (2020)
6. Fang, S., Wang, Y., Gou, B., et al.: Toward future green maritime transportation: an overview of seaport microgrids and all-electric ships. IEEE Trans. Veh. Technol. **69**(1), 207–219 (2019)
7. Tanaka, E.: Power generation plant ship: U.S. Patent Application 09/865,495. 2002–12-5
8. Georgiana, E.: A decision tree for weather prediction. Buletinul. LXI **1**, 77–82 (2009)
9. Sawale, G.J., Gupta, S.R.: Use of artificial neural network in data mining for weather forecasting. Int. J. Comput. Sci. Appl. **6**(2), 383–387 (2013)
10. Shanmuganathan, S., Sallis, P.: Data mining methods to generate severe wind gust models. Atmosphere **5**(1), 60–80 (2014)
11. Gkerekos, C., Lazakis, I.: A novel, data-driven heuristic framework for vessel weather routing. Ocean Eng. **197**, 106887 (2020)
12. Fang, S., Xu, Y., Wang, H. et al.: Robust operation of shipboard microgrids with multiple-battery energy storage system under navigation uncertainties. IEEE Trans. Vehic. Technol. (2020). In press
13. Hannan, M.A., Lipu, M.S., Hussain, A., et al.: A review of lithium-ion battery state of charge estimation and management system in electric vehicle applications: challenges and recommendations. Renew. Sustain. Energy Rev. **78**, 834–854 (2017)
14. Plett, G.L.: High-performance battery-pack power estimation using a dynamic cell model. IEEE Trans. Veh. Technol. **53**(5), 1586–1593 (2004)
15. Ashtiani, C.: Analysis of battery safety and hazards' risk mitigation. ECS Trans. **11**(19), 1 (2008)
16. Lin, X., Stefanopoulou, A.G., Perez, H.E. et al.: Quadruple adaptive observer of the core temperature in cylindrical Li-ion batteries and their health monitoring. In: 2012 American Control Conference (ACC), pp. 578–583. IEEE (2012)
17. Xie, J., Ma, J., Chen, J.: Available power prediction limited by multiple constraints for LiFePO4 batteries based on central difference Kalman filter. Int. J. Energy Res. **42**(15), 4730–4745 (2018)
18. Cannarella, J., Arnold, C.B.: State of health and charge measurements in lithium-ion batteries using mechanical stress. J. Power Sources **269**, 7–14 (2014)
19. Berecibar, M., Gandiaga, I., Villarreal, I., et al.: Critical review of state of health estimation methods of Li-ion batteries for real applications. Renew. Sustain. Energy Rev. **56**, 572–587 (2016)
20. Zheng, L., Zhang, L., Zhu, J., et al.: Co-estimation of state-of-charge, capacity and resistance for lithium-ion batteries based on a high-fidelity electrochemical model. Appl. Energy **180**, 424–434 (2016)
21. Gou, B., Xu, Y., Feng, X.X.: State-of-Health estimation and remaining-useful-life prediction for lithium-ion battery using a hybrid data-driven method. IEEE Trans. Vehic. Technol. (2020)
22. Pei, P., Chang, Q., Tang, T.: A quick evaluating method for automotive fuel cell lifetime. Int. J. Hydrogen Energy **33**(14), 3829–3836 (2008)
23. Chen, H., Pei, P., Song, M.: Lifetime prediction and the economic lifetime of proton exchange membrane fuel cells. Appl. Energy **142**, 154–163 (2015)
24. Xu, L., Li, J., Ouyang, M., et al.: Multi-mode control strategy for fuel cell electric vehicles regarding fuel economy and durability. Int. J. Hydrogen Energy **39**(5), 2374–2389 (2014)
25. Petrone, R., Zheng, Z., Hissel, D., et al.: A review on model-based diagnosis methodologies for PEMFCs. Int. J. Hydrogen Energy **38**(17), 7077–7091 (2013)
26. Cadet, C., Jemeï, S., Druart, F., et al.: Diagnostic tools for PEMFCs: from conception to implementation. Int. J. Hydrogen Energy **39**(20), 10613–10626 (2014)
27. Bressel, M., Hilairet, M., Hissel, D., et al.: Extended Kalman filter for prognostic of proton exchange membrane fuel cell. Appl. Energy **164**, 220–227 (2016)
28. Silva, R.E., Gouriveau, R., Jemei, S., et al.: Proton exchange membrane fuel cell degradation prediction based on adaptive neuro-fuzzy inference systems. Int. J. Hydrogen Energy **39**(21), 11128–11144 (2014)

29. Chandrasekaran, R., Bi, W., Fuller, T.F.: Robust design of battery/fuel cell hybrid systems—methodology for surrogate models of Pt stability and mitigation through system controls. J. Power Sources **182**(2), 546–557 (2008)
30. Hu, X., Feng, F., Liu, K., et al.: State estimation for advanced battery management: Key challenges and future trends. Renew. Sustain. Energy Rev. **114**, 109334 (2019)
31. Fang, S., Xu, Y., Wen, S., et al.: Data-driven robust coordination of generation and demand-Side in photovoltaic integrated all-electric ship microgrids. IEEE Trans. Power Syst. **35**(3), 1783–1795 (2019)
32. Yao, C., Chen, M., Hong, Y.Y.: Novel adaptive multi-clustering algorithm-based optimal ESS sizing in ship power system considering uncertainty. IEEE Trans. Power Syst. **33**(1), 307–316 (2017)
33. Wen, S., Zhang, C., Lan, H. et al.: A hybrid ensemble model for interval prediction of solar power output in ship onboard power systems. IEEE Trans. Sustain. Energy (2019)
34. Fang, S., Xu, Y., Li, Z., et al.: Two-step multi-objective management of hybrid energy storage system in all-electric ship microgrids. IEEE Trans. Veh. Technol. **68**(4), 3361–3373 (2019)
35. Fang, S., Xu, Y., Li, Z., et al.: Optimal sizing of shipboard carbon capture system for maritime greenhouse emission control. IEEE Trans. Ind. Appl. **55**(6), 5543–5553 (2019)
36. Lai, K., Illindala, S.: Graph theory based shipboard power system expansion strategy for enhanced resilience. IEEE Trans. Ind. Appl. **54**(6), 5691–5699 (2018)
37. Lan, H., Wen, S., Hong, Y.Y., et al.: Optimal sizing of hybrid PV/diesel/battery in ship power system. Appl. Energy **158**, 26–34 (2015)
38. Wen, S., Lan, H., Yu, D.C., et al.: Optimal sizing of hybrid energy storage sub-systems in PV/diesel ship power system using frequency analysis. Energy **140**, 198–208 (2017)
39. Hou, J., Sun, J., Hofmann, H.: Control development and performance evaluation for battery/flywheel hybrid energy storage solutions to mitigate load fluctuations in all-electric ship propulsion systems. Appl. Energy **212**, 919–930 (2018)